

NASA
Technical
Paper
3040

September 1990

AMES
IN-71

1721

967

Acoustic and Aerodynamic Study of a Pusher-Propeller Aircraft Model

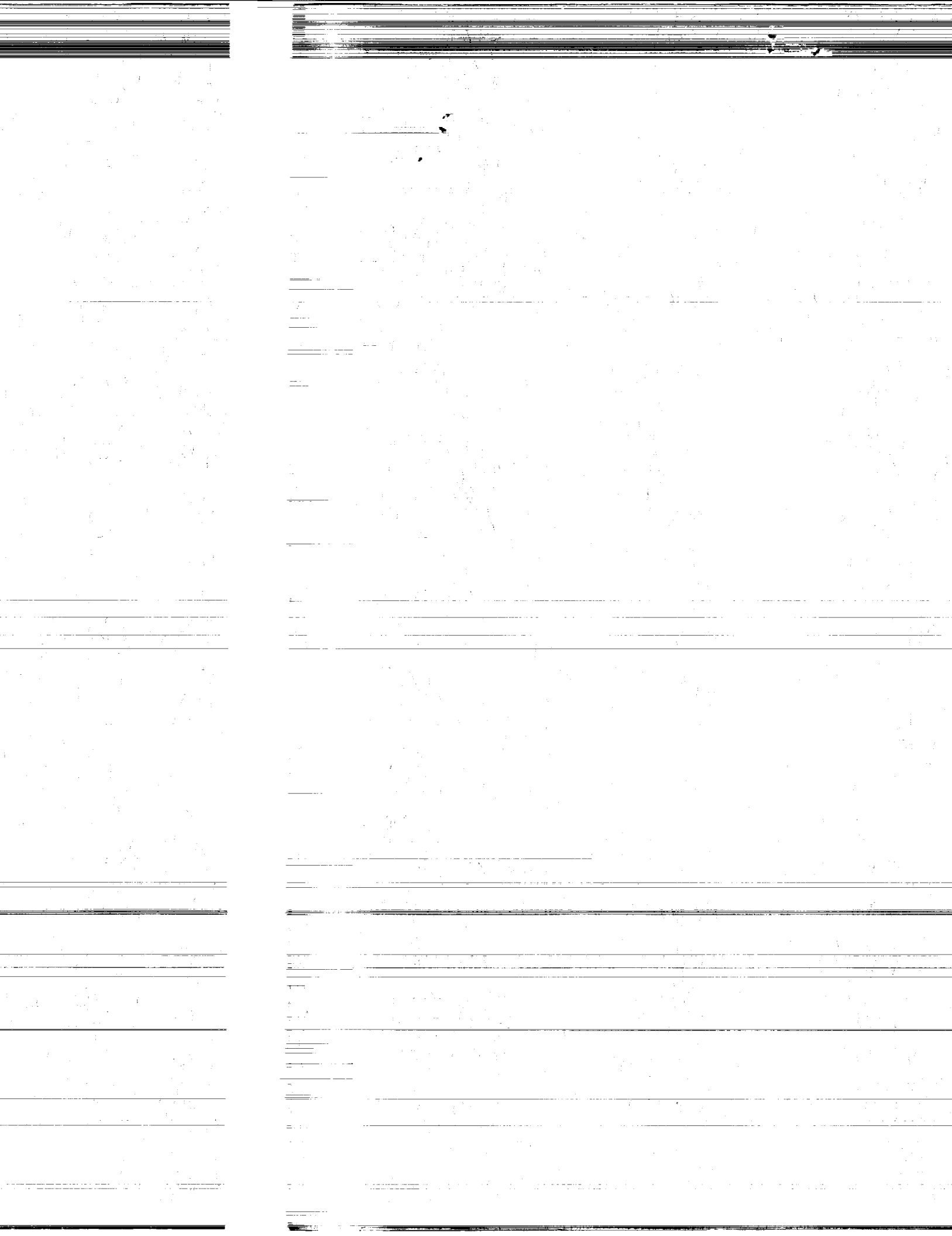
Paul T. Soderman
and W. Clifton Horne

(NASA-TP-3040) ACOUSTIC AND AERODYNAMIC
STUDY OF A PUSHER-PROPELLER AIRCRAFT MODEL
(NASA) 67 D CSCL 20A

N91-21828

H1/71 Unclas
0001721

NASA



**NASA
Technical
Paper
3040**

1990

**Acoustic and
Aerodynamic Study
of a Pusher-Propeller
Aircraft Model**

Paul T. Soderman
and W. Clifton Horne
*Ames Research Center
Moffett Field, California*

NASA

National Aeronautics and
Space Administration
Office of Management
Scientific and Technical
Information Division

CONTENTS

	<u>Page</u>
NOMENCLATURE.....	vii
SUMMARY.....	1
INTRODUCTION.....	1
MODELS AND APPARATUS	2
Empennages and Fuselage	2
Propeller and Drive Motor	2
Test Section and Acoustic Arena	2
Microphones	3
Instrumentation for Data Acquisition and Reduction	3
EXPERIMENTAL METHOD	3
Coordinate System and Empennage/Propeller Spacing	3
Wind Tunnel Operation	3
Propeller Operation	4
Acoustic Data Reduction	4
RESULTS AND DISCUSSION	4
Noise Resulting from Facility and Test Hardware	5
Fuselage and motor nacelle in test section	5
Fuselage and empennage in test section	5
Propeller alone	5
Propeller plus fuselage.....	6
Data Repeatability and Floor Reflections	6
Propeller/Empennage Interaction Noise	6
Y-tail	6
V-tail	7
I-tail	7
Time signatures	7
Comparison of acoustic spectra and directivity	8
Tail loading	9
Empennage/propeller axial separation	9
Empennage/propeller vertical separation	10
Correlation of Acoustics and Aerodynamics	10
Wake deficit	10
Turbulence	10
Implications for Propeller Noise Prediction	11
CONCLUSIONS	12
REFERENCES	13
APPENDIX	15
Analytical Prediction of Propeller Blade Loading and Noise Generation Computer Code WTPROP2	

INDEX TO FIGURES

	<u>Page</u>
Figure 1. Model propeller, empennages, and fuselage in the wind tunnel	28
Figure 2. Schematic of model in test section	30
Figure 3. Geometry of empennages.....	31
Figure 4. SR-2 propeller geometry.	32
Figure 5. Sound-absorbent panels used to prevent wall reflections.....	34
Figure 6. Microphone locations relative to the propeller.....	35
Figure 7. Acoustic data-acquisition and reduction system	36
Figure 8. Flow survey apparatus.....	37
Figure 9. Coordinate systems.....	38
Figure 10. Background noise out of flow	38
Figure 11. Background noise in the flow.....	39
Figure 12. Comparison of background noise measured in and out of flow	39
Figure 13. Influence of Y-tail on background noise (propeller not operating).....	40
Figure 14. Propeller-alone noise at one rotational speed	40
Figure 15. Propeller-alone noise at two rotational speeds	41
Figure 16. Effect of fuselage on propeller noise.....	41
Figure 17. Blade-passage harmonic noise with Y-tail as measured at 10 locations.....	41
Figure 18. Effect of Y-tail on acoustic spectrum	43
Figure 19. Effect of Y-tail on blade-passage harmonic noise	44
Figure 20. Effect of V-tail on acoustic spectra	44
Figure 21. Effect of V-tail on blade-passage harmonic noise	45
Figure 22. Effect of I-tail on acoustic spectra.....	45
Figure 23. Effect of I-tail on blade-passage harmonic noise	46
Figure 24. Acoustic pressure time traces inside and outside the shear layer	46
Figure 25. Propeller acoustic pressures without empennage installed	47

	<u>Page</u>
Figure 26. In-plane acoustic pressure with Y-tail, V-tail, and I-tail installed	47
Figure 27. Upstream acoustic pressures with Y-tail, V-tail, and I-tail installed.....	48
Figure 28. Downstream acoustic pressures with Y-tail, V-tail and I-tail installed.....	49
Figure 29. Comparison of blade-passage harmonic noise from three empennages.....	50
Figure 30. Acoustic directivity in propeller plane	52
Figure 31. Effect of empennage incidence angle on noise	53
Figure 32. Variation of noise with propeller/empennage spacing	54
Figure 33. Summary of noise decay with propeller/empennage spacing	55
Figure 34. Noise decay with propeller/empennage space–data from two studies	55
Figure 35. Effect of propeller vertical location on noise	56
Figure 36. Mean velocity deficit in I-tail wake	56
Figure 37. Peak wake deficit versus distance downstream from the empennage.....	57
Figure 38. Wake width versus distance downstream from the empennage.....	57
Figure 39. Turbulence distribution in the I-tail wake	57
Figure 40. Turbulence spectra inside and outside the I-tail wake	59
Figure 41. Predicted and measured blade-passage harmonic noise	59

NOMENCLATURE

b	propeller blade chord, mm	u'	turbulent velocity component in axial direction (rms), m/sec
b_w	wake width measured at mid height of the wake deficit, mm	v'	turbulent velocity component in vertical direction (rms), m/sec
c	empennage chord measured streamwise, mm	w'	turbulent velocity component in horizontal cross-stream direction (rms), m/sec
c'	mean of the empennage chords measured at the empennage root and propeller tip station, mm ($c' = 291$ for Y-tail, $c' = 570$ for I-tail, $c' = 261$ for dorsal fin)	x	downstream distance from aft tip of fuselage, mm
C_d	empennage drag coefficient	x'	mean distance from empennage trailing edge to propeller as measured at the empennage root and propeller tip station, mm
C_l	design lift coefficient of blade as a function of radial station	x_p	downstream distance from empennage trailing edge to wake probe as measured along streamline intersecting probe, mm
C_p	power coefficient, $power/(\rho n^3 d^5)$	y	vertical distance from center of aft tip of fuselage, mm
C_t	thrust coefficient, $thrust/(\rho n^2 d^4)$	z	horizontal distance from center of aft tip of fuselage (positive to left facing upstream), mm
d	propeller diameter, m	α	Y-tail angle of attack measured near the tip, deg
J	advance ratio, $U_\infty/(nd)$	β	propeller blade pitch angle between 3/4 radius chord line and plane of propeller as measured at the 3/4 radius station, deg
l	dimension on airfoil equal to vortex street spacing; i.e., distance between upper and lower surface regions where vortices are created, m	β_0	propeller blade twist angle relative to the 3/4 radius chord line, deg
$L_p(f)$	sound pressure level measured with an effective filter bandwidth of 42 Hz, dB	$\Delta L_{p_c}(f)$	change in blade-passage sound pressure level, dB
$L_{p_c}(f)$	sound pressure level of blade-passage harmonic corrected for broadband amplification, dB	λ	acoustic wavelength, m
n	propeller rotational speed, rev/sec	ρ	air density, kg/m^3
N	propeller rotational speed, rev/min	φ	angle in vertical plane containing propeller, deg; 0° is down, 90° is to right facing upstream
St	Strouhal number	ψ	model roll angle, deg; 90° is right wing down
t	propeller blade thickness, mm	θ	angle in horizontal plane centered on propeller, deg; 0° is upstream, 90° is to the left facing upstream
U_∞	test section airspeed measured 1.3 m upstream of the fuselage nose, m/sec		
U_{wake}	airspeed measured in the empennage wake, m/sec		
\bar{U}	normalized streamwise velocity deficit in wake, $(U_\infty - U_{wake})/U_\infty$		
\bar{U}_{max}	maximum value of \bar{U} in the wake		

SUMMARY

An aerodynamic and acoustic study was made of a pusher-propeller aircraft model in the NASA Ames Research Center 7- by 10-Foot Wind Tunnel. The test section was modified to operate as an open jet. The 591-mm diameter unswept propeller was operated alone and in the wake of three empennages—an I-tail, a Y-tail, and a V-tail. The radiated noise and detailed wake properties were measured. Results indicate that the unsteady blade loading caused by the blade interactions with the wake mean velocity distribution had a strong effect on the harmonics of blade-passage noise. In particular, the blade-passage harmonics above the first were substantially increased in all horizontal directions by the empennage/propeller interaction. Directivity in the plane of the propeller was maximum perpendicular to the blade surface. Increasing the tail loading caused the propeller harmonics to increase 3-5 dB for an empennage/propeller spacing of 0.38 mean empennage chords. The interaction noise became weak as empennage/propeller spacing was increased beyond 1.0 mean empennage chord lengths. Unlike the mean wake deficit, the wake turbulence had only a small effect on the propeller noise, that effect being a small increase in the broadband noise. A propeller noise theory, which incorporated an unsteady blade-loading model, indicates that the interaction noise trends can be predicted if the unsteady blade-loading aerodynamic and acoustics are modeled properly.

INTRODUCTION

The pusher propeller has become a viable option for the aircraft designer in recent years. A variety of designs have been proposed and built which have propellers mounted behind wings, on aft fuselages, and on empennages. In some cases, the pusher propeller is more efficient aerodynamically than a tractor propeller because of the lower velocity inflow from the upstream body. Furthermore, locating the propeller on the aft portions of the aircraft allows flexibility in the location of the power plant. Acoustically, pusher propellers can produce more cabin noise than tractor designs, although cockpit noise should be lower with a pusher. Flyover and cabin noise can be a problem because of the flow disturbances ingested by the propeller from wakes and engine exhausts, which translate into radiated noise.

Several studies have been made of the acoustic characteristics of pusher propellers in recent years, notably by P. Block (1984, 1985, 1986) and others at NASA Langley

Research Center. Those studies dealt with a single pylon or a single airfoil mounted upstream of a propeller. Wake measurements were limited. The study described here involved single and multiple airfoil wakes interacting with a pusher propeller, and wake properties were measured in detail.

The present study was an attempt to improve the basic understanding of propeller-wake interactions and the radiated noise from a pusher propeller operating behind an aircraft empennage. An experiment was conducted in the Ames Research Center 7- by 10-Foot Wind Tunnel #1, which was modified into an open-jet configuration (floor remaining) to minimize acoustic reflections. The model included a fuselage capable of accepting three empennage configurations, and a detached propeller mounted to an electric motor downstream of the empennage. The fuselage was provided by the Lear Fan Corp. in Reno, Nevada. It was recognized that the location of the propeller relative to the upstream aerodynamic surfaces is a critical factor in the strength of the aerodynamic interaction, just as it is in the case of rotor-stator interactions in ducts (Kramer et al., 1972). In the latter case, it was demonstrated that stator noise caused by interactions with the wakes of upstream rotors can be quite strong if the rotor-stator spacing is less than one rotor chord. As that spacing is increased, the interaction and induced noise decay rapidly. Therefore, this experiment was designed to allow flexibility in the location of the propeller relative to the empennage. Furthermore, significant effort was put into measurements of the flow field entering the propeller and the effect of the propeller on the development of that flow field. That aerodynamic phase of the study was sufficiently extensive to be published as a separate report (Horne and Soderman, 1988).

In order to make it available as soon as possible, the acoustic data acquired in this study was published as a NASA Contractor Report by Wilby and Wilby (1985). That report is extensive and laid the basic framework for this publication. Some of the results of Wilby and Wilby (1985) were clouded by data scatter. Since then, careful examination of the data has traced the problem to floor reflections at specific microphones. We believe the problem data have been eliminated to allow a clearer interpretation of the empennage/propeller interaction. This report summarizes and correlates the acoustic and aerodynamic work reported in the above two references. Finally, the experimental results acquired here are compared with an analytical method for predicting propeller noise.

MODELS AND APPARATUS

Empennages and Fuselage

Figures 1 and 2 show the Ames 7- by 10-Foot Wind Tunnel #1 open-jet test section, acoustic measurement arena, and the three empennage configurations studied—the Y-tail, V-tail, and I-tail mounted on a model fuselage without a wing. The Y-tail is shown in figures 1(a)-(c). (An index of figures follows the Contents.) Note that the empennage is oversized for the fuselage. That is because the fuselage was available as an empennage support structure, but was not essential to the simulation. Instead, the empennage was sized to span the propeller disc so that tip vortices would not intersect the propeller. It was decided that because tip vortices are strong sources of flow disturbance, tip-vortex ingestion by the propeller would be avoided. Tip-vortex ingestion can dominate propeller or rotor noise generation (Schlinker and Amiet, 1983), depending on various parameters such as vortex strength and angle of incidence relative to blade normal. It is assumed that aircraft designers would avoid tip-vortex ingestion also, if at all possible. Figure 1(b) shows the fuselage and Y-tail rolled 90° ($\psi = 90^\circ$) so that the sideline microphones would be in a flyover position. When the model was rolled 90° , the fuselage remained aligned with the propeller shaft as it was with the model upright.

The I-tail, a simple vertical fin, is illustrated in figure 1(d). Figures 2(a) and (b) show the model with the I-tail positioned relative to the test section inlet and collector. The third empennage configuration, not shown in the photographs explicitly, was the V-tail, which was created by removing the lower dorsal fin from the Y-tail. Figures 3(a) and (b) show a schematic of the empennages with the appropriate dimensions and sweep angles noted. The empennages had no elevators or tabs. The Y-tail upper surfaces were operated at 1° and, where noted, 6° angle of attack (α) relative to the free stream as measured in a plane perpendicular to the empennage surface. All empennage surfaces had streamwise contours shaped as NACA 0012 airfoils. Thus, at each spanwise station, the maximum thickness was 12% of the chord.

Propeller and Drive Motor

The propeller was a four-bladed, SR-2 composite propeller with a 591-mm diameter. The SR-2 blades have been used in several wind tunnel acoustic studies of eight-bladed propellers at cruise speeds (Block, 1985, 1986; Block and Gentry, 1986; Dittmar, Blaha, and Jerack, 1978; Dittmar, Jerack; and Blaha, 1979; Dittmar, 1980). The

blades had zero sweep and a relatively low thickness-to-chord ratio, tapering to 2% at the tip. The propeller shape and dimensions are given in figures 4(a)-(c). The hub was 98 mm in diameter. Blade pitch angles were adjusted manually using a propeller protractor and were chosen for each airspeed and rotational speed to provide appropriate blade loading. The pitch angles, defined as the angle between the $3/4$ -radius chord line and propeller disc plane, were measured at the $3/4$ -radius station. The blades were twisted relative to the $3/4$ -radius chord line as shown in figure 4(a). Table 1 lists the blade angles used during the study. This size propeller and empennage would be approximately $1/3$ to $1/5$ scale of typical full-scale aircraft components.

The propeller was mounted on a 711-mm-long shaft and driven by an electric motor in a nacelle as shown in figures 1 and 2. Attempts to monitor propeller thrust with a simple thrust cell on the motor-sliding carriage failed. Therefore, all performance estimates were made analytically using the method of Larrabee and French (1983) described in the Appendix. The propeller/motor strut was adjustable in the vertical direction for a range of 178 mm. The fuselage support struts were mounted to a track system that allowed the fuselage to be moved in the streamwise direction. This allowed the propeller noise sources to be fixed in space during the variation of empennage/propeller spacing, except for the small vertical motion allowed in the motor support strut during one phase of the study.

Test Section and Acoustic Arena

The 7- by 10-Foot Wind Tunnel test section had the two side walls and the ceiling removed for a streamwise distance of 4.17 m. A bell-mouth collector, covered by 76-mm polyurethane foam to minimize acoustic reflections, was installed at the inlet to the diffuser. This geometry allows stable flow conditions up to a test-section speed of approximately 68 m/sec. Above that speed, flow oscillations develop, resulting from the well-known open-jet collector/nozzle feedback resonance (Martin, Brooks and Hoad, 1985).

The acoustic test hall surrounding the test section was approximately 14 by 17 by 9 m high. The steel walls of the room had been covered with acoustical tile, but this was inadequate to prevent reflections from the walls. Therefore, 1.2- by 2.4-m plywood panels, covered with 101- to 152-mm-thick polyurethane foam in alternating blocks, as shown in figure 5(a), were placed around the test arena (fig. 5(b)). The panels were tipped back so any reflections tended to reflect upward and away from the microphones. Polyurethane foam, 76 mm thick, was placed on the wooden floor in the test section and in the

test arena to prevent floor reflections. This method was only partially successful, as will be explained. Optimum positioning of the sound-absorbent panels was achieved by reviewing pulse reflections from a starter pistol fired near the propeller. No deleterious reflections were found with the impulsive source, although floor reflections of propeller tones were later found to be a problem, as will be discussed.

The background noise of this wind tunnel has been attenuated by the installation of acoustic linings in the end legs of the circuit and the installation of a large acoustic splitter in the cross leg upstream of the test section (Soderman and Hoglund, 1979).

Microphones

Condenser microphones (B&K 4133), 12.5 mm in diameter, were placed in positions 1-13 as shown in figures 6(a) and (b). Microphones 1-6, outside the flow on the left side of the model, were on a 4.27-m arc centered on the propeller hub at horizontal angles 60 to 120° (0° corresponds to the upstream direction). The microphones were at the propeller hub height. Two microphones, numbers 10 and 13, were in the same horizontal plane, but on the other side of the test section at angles of 270 and 290°. These microphones experienced some flow buffet from the shear layer. Microphones 11 and 12 were on a 4.27-m arc in the vertical plane containing the propeller disk (fig. 6(b)). Finally, microphones 7, 8, and 9 were in the flow closer to the model, as shown in figure 6(a). The inflow microphones had bullet-shaped nose cones pointed upstream to minimize flow noise and were essentially omnidirectional. The microphones remained fixed during the test program. All microphones, except 11 and 12, recorded sideline noise with the aircraft model upright ($\psi = 0^\circ$). With the model rolled on its side ($\psi = 90^\circ$), microphones 1-9 were under the model and microphones 10 and 13 were above the model. All microphones, except 7 and 8, were several propeller diameters and acoustic wavelengths from the propeller therefore and were, in the acoustic far field ($\lambda = 0.6$ m at the blade passage fundamental frequency at 8200 rpm). Microphones 7 and 8 were about 2.3 propeller diameters and/or blade-passage fundamental wavelengths from the hub, which is the beginning of the far-field region.

Instrumentation for Data Acquisition and Reduction

The microphone signals were monitored, recorded, and processed as shown in figure 7. The computer controller was used to coordinate the data acquisition, store

the digitized data generated by the narrow-band spectrum analyzer, and correct the results. Software used to acquire and process the data is listed in the report of Wilby and Wilby (1985).

A floor-mounted, three-axis traversing mechanism shown in figure 8(a) (prior to removal of the test section walls) was used to survey the empennage wake. The mechanism was located in the left side of the test section between the shear layer and the model to minimize interference effects. The computer-controlled apparatus is described by Horne and Soderman (1988). The flow survey probes used to acquire the pressure and hot-wire data are illustrated in figure 8(b). The pitot-static pressure probe was used to determine the velocity distribution in the wake. The five-hole, directional pressure probe measured flow direction. The two X-wire probes were used to measure the three components of turbulence. Details of the survey instrumentation and hot-wire data-reduction algorithms are given in the above report.

EXPERIMENTAL METHOD

Coordinate System and Empennage/Propeller Spacing

The distance between the model fuselage and propeller was varied in both longitudinal (x -coordinate) and vertical (y -coordinate) directions (z is the horizontal cross-stream coordinate). The origin for the x,y,z coordinates was the aft tip of the tail cone on the fuselage centerline, as shown in figure 9. A more relevant coordinate is the distance from the empennage trailing edge to the propeller, x_p . A similar distance is x' —the mean of the separation distance measured at the empennage root and empennage station opposite the propeller tip. A normalized distance, x'/c' , is also used, where c' is the mean of the empennage chords measured at the same two stations. Since the empennages were swept aft, in the case of the I-tail and dorsal fin, and swept forward, in the case of the Y-tail, x' is a variable which depends on the empennage geometry. The normalized separation distance noted for the Y-tail on the figures refers to the distance from the propeller to the upper two surfaces, not the distance to the dorsal fin.

Wind Tunnel Operation

The wind tunnel was operated at test-section airspeeds of 46 and 62 m/sec (Mach numbers of 0.13 and 0.18). These low speeds correspond to aircraft approach and takeoff speeds. During the flow survey

measurements, the flow speed was fixed at 46 m/sec. Temperature, barometric pressure, and humidity were measured periodically during the test sequence.

Propeller Operation

The acoustic measurements were made with propeller rotational speeds of 6000 and 8200 rpm. Propeller rotation was counter clockwise facing upstream. The propeller tip rotational Mach number ranged from 0.54 to 0.74, and the helical Mach number ranged from 0.56 to 0.77. On a typical general aviation aircraft, both Mach numbers lie in the range 0.65 to 0.90. Thus, the 8200-rpm data are most representative of current aircraft. The propeller blade-passage frequencies associated with 6000 and 8200 rpm were 400 and 547 Hz, respectively. The propeller advance ratio ranged from 0 to 1.06, which is close to typical values of general aviation aircraft. Table 1 lists the advance ratios, thrust coefficients, and power coefficient for each test condition. Those parameters were computed using the propeller aerodynamic theory of Larrabee and French (1983), which was incorporated into a computer code listed in the Appendix. The method does not allow prediction of propeller performance at zero advance ratio.

Acoustic Data Reduction

Narrow-band acoustic spectra were generated with the fast Fourier transform (FFT) analyzer from sound recordings approximately 30 sec long. Some spectra were acquired on line. The FFT analysis mode was chosen for sinusoidal signals, which gives the correct spectrum level for narrow-band peaks. However, this mode results in relatively wide filter bandwidths of 42 Hz (12.5×3.4). Since the output is "power in the band," the broadband levels should be reduced by $10 \log 42 = 16$ dB to give the power spectral density. (The data are presented without this adjustment.) Tone levels, of course, are unaffected by filter width and should not be reduced to give power spectral density. The data were corrected for gain, shear-layer refraction, and distance decay by normalizing to a common distance of 4.27 m using 6 dB per double-distance extrapolation.

The shear-layer refraction correction was based on the analytical method of Amiet (1975). That refraction correction accounts for the apparent directivity shift of the sound propagating through the shear layer. Noise measured at 90° from the propeller, for example, came from an acoustic ray emitted at 96° for a windspeed of 62 m/sec. Thus, the data measured at a given microphone outside the flow will be labeled for the computed radia-

tion angle, which changes depending on windspeed. The angles for the microphone data recorded inside the flow are not affected by these computations. A discussion of the method and the computer code is given by Wilby and Wilby (1985). It was determined that spectral broadening of the blade-passage harmonics due to turbulence scattering was not important except at the highest harmonics. Therefore, no such correction was made. The spectral harmonics were corrected, however, for amplification from the adjacent broadband noise (harmonic plots only, not spectral plots). That is, the true levels of the harmonics in the 42-Hz filter bands were increased by broadband noise within 10 dB of the harmonic level. Thus, the apparent harmonic levels in the spectral plots were corrected for the computed amplification, assuming that the discrete frequency and broadband components were uncorrelated, so that the calculated amplification could be made on an energy basis. For example, if a harmonic peak occurred at 71.8 dB, and the broadband level in that band was 67.8 dB, the true harmonic level was estimated to be $10 \log (10^{7.18} - 10^{6.78}) = 69.6$ dB.

RESULTS AND DISCUSSION

The main objective of this report is to correlate the propeller noise with the key geometric and fluid-mechanic parameters affecting the noise radiation. First, however, it will be necessary to summarize acoustic characteristics of the experiment such as background noise of the facility and test hardware, and floor reflections. Then, the noise of the isolated propeller will be discussed, followed by a discussion of the acoustic effects of each empennage configuration. The important wake properties will be identified. Finally, the correlation of the acoustic and aerodynamic data will be made.

Much of the acoustic data are presented as narrow-band levels at harmonics of blade-passage frequency. That is because, as will be seen, the narrow-band sound dominated the broadband sound. Furthermore, certain harmonic levels may be more important than overall sound levels, when the data are scaled to a full-size aircraft. Overall sound levels are often used as a key acoustic parameter in the literature. But in scale-model testing, it may not be appropriate. For example, the overall noise level in this study was dominated by noise at the blade-passage frequency of 547 Hz (8200 rpm). But if the data were scaled to an aircraft five times the size of the model, that propeller blade-passage frequency would be reduced by a factor of five because the tip Mach number would be held constant for proper simulation. Thus, the peak noise would be at 109 Hz, and would be less annoying than noise at higher harmonics, which would fall in the

sensitive frequency range of human hearing. For this reason, results are presented for many harmonics of blade-passage frequency.

Noise Resulting from Facility and Test Hardware

Fuselage and motor nacelle in test section— The basic test hardware is considered to be the fuselage without empennage, and the motor/nacelle and shaft without propeller. Figures 10 and 11 show the test hardware noise out of flow (microphone 2) and in flow (microphone 7), respectively, at windspeeds of 46 and 62 m/sec. Recall that as the windspeed changes, the computed directivity angle changes because the shear-layer refraction is a function of jet speed. These data are representative of all microphones and show that the windspeed increase caused an acoustic increase of 9 to 10 dB out of flow (fig. 10) and an increase of 7 to 8 dB in flow (fig. 11). The in-flow noise increase of 7 to 8 dB corresponds to the square of acoustic pressure proportional to velocity to the fifth or sixth power, which is indicative of dipole-type sources. Wind tunnel fan noise, for example, follows that velocity law. The out-of-flow noise increase of 9 to 10 dB is more difficult to explain, but may indicate that, in addition to the above acoustic power-velocity law, additional noise sources, such as on the collector, developed at the higher flow speeds.

It was determined that one of the peaks in the background noise spectrum was caused by vortex shedding from the microphone support struts, a common phenomenon in wind tunnel testing (Soderman, 1976). The peaks were visible in the out-of-flow microphone data. At 46 m/sec the peak occurred at 1780 Hz, and at 62 m/sec the peak was at 2470 Hz, as seen in figure 10. These frequencies relate to a Strouhal number of 0.28 and a dimension, l , comparable to the distance between flow-separation points on the two sides of the strut (Soderman, 1976), a distance which, in this case, was about a third of the strut maximum thickness. The vortex shedding rate is

$$f = St U_{\infty} / l \quad (1)$$

The addition of boundary-layer flow trips to the struts eliminated the tones. The trips were formed from cloth duct tape that was rolled into long loops with the sticky side out, and stuck to the struts' leading edges. Thus, a bulky, sticky protuberance was created that covered the upper and lower surfaces back to approximately 25% chord. The resulting flow disturbance broke up the coherent vortex streets. The high noise levels at very low frequencies were caused by the wind tunnel fan, which had a

blade-passage frequency of 147 Hz for a windspeed of 62 m/sec.

When in-flow and out-of-flow microphone signals are compared at the same airspeed in figure 12(a), it is clear that the in-flow microphone noise included considerable nonpropagating pressure fluctuations. Figure 12(a) shows that even after the data are corrected to the same distance, the in-flow microphone 7 had higher background noise levels than out-of-flow microphone 5. Figure 12(b) shows the background noise for all three in-flow microphones—7, 8, and 9. Microphone 7 had high levels of low-frequency noise because it was positioned at the edge of the shear layer. The shear layer spread at approximately 8° total angle (Soderman and Olson, 1988). The large-scale turbulence and vortices in the shear layer caused the low-frequency noise at that microphone. Microphone 9 shows some strut tones that were subsequently removed by tripping the flow over the microphone stand, as discussed above. Therefore, the propeller noise data from each microphone must be compared with the background noise of that microphone.

Fuselage and empennage in test section— The effect of the empennage on the sound levels was negligible (propeller removed). This is shown in figure 13, which illustrates background noise levels at microphone 2 ($\theta = 78^\circ$) with and without the Y-tail mounted on the fuselage. Note that the strut vortex-shedding noise at 2470 Hz has been eliminated in this data set by the attachment of the flow-trip tape to the microphone struts in the test section.

Propeller alone— Figures 14(a) and (b) show propeller-alone noise at 8200 rpm and at windspeeds of 46 and 62 m/sec compared with the wind-off case (fuselage and empennage removed). It is clear that the propeller generated strong tones at harmonics of the blade-passage frequency that dominated the broadband noise, at least to the fourth or fifth harmonic for this in-flow microphone 7. Out-of-flow microphone data contain tones out to the eighth or tenth harmonic. Comparison of the propeller broadband noise with the wind tunnel background noise at the same windspeed (figs. 11 and 12) shows that the wind tunnel background noise dominated the propeller broadband noise at the in-flow microphone 7. Out of flow, the propeller broadband noise dominated the wind tunnel background noise by around 5 dB at 46 m/sec windspeed and by only 1-2 dB at 62 m/sec. Thus, the data analysis will concentrate on the harmonic levels.

It is interesting that the level of the tones generated statically agree so well with the tone levels wind on. (The wind-off and wind-on tones in fig. 14(b) would agree better if the broadband contributions to the tones were removed.) Many researchers have reported large discrepancies between static and flight noise attributed to

static ingestion of ground vortices or atmospheric turbulence that create disturbances at the propulsive device that are not present in flight. No such problem with the static data is apparent in figure 14, possibly because (1) the propeller may have induced a very low, but significant, airflow in the wind tunnel, (2) the wind tunnel air has low turbulence compared to out-of-doors, and (3) the propeller was unable to induce a ground vortex because of its low thrust. In any case, wind-on data are essential for generation of proper acoustic directivity patterns and to study the propeller/empennage interactions.

Figure 15 shows blade-passage harmonic noise levels for zero windspeed and propeller rotational speeds of 6000 and 8200 rpm (fuselage and empennage removed). The data show the rapid roll-off of blade-passage harmonics with frequency, particularly at the lower rpm. This is characteristic of propeller steady-loading noise and thickness noise.

The above results show that the spectral peaks are more important to this study than the broadband noise. Therefore, the following analyses will emphasize the blade-passage harmonic levels, corrected for broadband contribution where appropriate, as discussed in the section on data reduction.

Propeller plus fuselage— Figure 16 shows that the fuselage without empennage did not create a strong enough wake at the propeller to cause the noise to change. The aft end of the fuselage was in line with the propeller hub as shown in figures 1 and 2 and was 152 mm upstream of the propeller plane. Flow surveys of the fuselage wake (Horne and Soderman, 1988) showed that the fuselage wake was approximately 100 mm wide at a station 380 mm downstream of the fuselage tip. Thus the wake would enter the central portion of the 591-mm-diameter propeller where the blade speeds are relatively low and the noise generation is relatively weak. Most propeller noise generation occurs from the outer 1/4-radius portion of the propeller (Hersh, Soderman, and Hayden, 1974).

Data Repeatability and Floor Reflections

Examination of data measured at different dates for the same test condition indicated that there was significant scatter in the level of the harmonics of blade-passage tones at certain microphones. The broadband levels, on the other hand, were repeatable. Figures 17(a)-(f) illustrate scatter of harmonic levels from microphones 1-6 (out of flow) for repeat conditions. (All reference to angles incorporates the shear-layer refraction correction for data recorded outside the jet.) The scatter of around ± 3 dB was typical of the data from microphones 1-6 outside the test section. However, the scatter from micro-

phones 11 and 12 (figs. 17(i) and (j)) was much less. Those two microphones, in the plane of the propeller, were suspended from the ceiling in the acoustic arena surrounding the test section and were relatively far from reflecting surfaces. This suggests that floor reflections (or shear-layer distortions) were affecting the propeller tones recorded by microphones 1-6, despite the 76-mm absorbent floor lining. A calculation of floor reflections from a lining with 90% sound absorption shows that the interference with the direct periodic sound wave could lead to ± 2 dB variation in the combined sound level. The interference could vary if the phase of the signal varied with time because of source motion or propagation through the unsteady shear layer. In fact, distortion of the tonal wave form by the shear layer could be more important than the floor reflection, an effect that is minimum in the plane of the propeller. This distortion will be shown in the section on time signatures. Another ± 1 dB could be expected because of the random nature of the propeller interaction with an unsteady wake. Figures 17(g) and (h) indicate that the data scatter from microphones 8 and 9, which was unaffected by the shear layer, was smaller than that for microphones 1-6. Consequently, many of the results of this study will be based on the data from microphones 8-9 and 11-12. Those data represent noise propagated upstream and downstream of the aircraft model and to the sideline (or below, with the model rotated 90°). General trends in the data from the other microphones will be reported where appropriate. All data have been corrected to the same distance of 4.3 m from the propeller hub.

Propeller/Empennage Interaction Noise

Y-tail— The addition of the empennage to the model caused the propeller blade-passage tone and harmonics to increase across the spectrum relative to the model noise without empennage as shown in figures 18(a)-(c), which correspond to noise at directivity angles, θ , of 15, 96, and 140° . The mean empennage/propeller separation distance was 0.80 mean chords. The broadband noise was not changed by the empennage except for a slight increase above 5 kHz. Figures 19(a)-(c) show the same comparison in terms of harmonic levels only, which allows a clearer interpretation of the data. (Harmonic levels have been corrected for broadband contribution as previously discussed.) The fundamental or first harmonic at 547 Hz was little affected by the empennage/propeller interaction, but the higher harmonic levels increased 10-20 dB because of the Y-tail. This is consistent with the idea that the blade-loading variations resulting from wake interaction occur rapidly relative to a blade revolution so that in the frequency domain the higher frequencies are affected

more than the low frequencies. As for the consistency of the fundamental blade-passage noise, Trebble and Williams (1983) showed that propeller noise at the blade-passage frequency is dominated by the steady-loading rotational noise and is, therefore (we conclude), relatively unaffected by wake interactions. Note that in figure 18(a) the harmonic levels above the fourth at $\theta = 15^\circ$, empennage removed, were masked by the broadband noise and, therefore, are not shown. Nevertheless, the spectral plots show that the difference between the two curves above the fourth harmonic (fig. 19(a)) was at least as great as the difference at the fourth harmonic.

Microphone 12, at $\theta = 96^\circ$, did not record a significant increase in sound out to the fifth harmonic due to empennage/propeller interaction as shown in figures 18(b) and 19(b). This is probably because the thickness noise dominates the in-plane noise from approximately the second to fifth harmonics (Trebble and Williams, 1983). The unsteady loading noise, becomes important in the propeller plane only at the higher harmonics. Block and Gentry (1986) reported a similar effect on overall noise levels in a study of propeller interaction with a single upstream pylon. Note that the harmonic levels above the fifth harmonic were increased by the propeller/empennage interaction in all directions.

V-tail— The V-tail was created by simply removing the lower dorsal fin from the Y-tail. Figures 20(a)-(c) show the effect of the V-tail on the propeller acoustic spectra, and figures 21(a)-(c) show the same data plotted as harmonic levels only. The data are similar to the data acquired with the Y-tail, except for some small differences in the upstream direction. Thus, the dorsal fin had a weak effect on the propeller in-flow relative to the two upper surfaces. This is because the dorsal tip projected beyond the propeller radius so any tip vortex would have missed the propeller. Furthermore, the dorsal fin was at zero yaw angle so it was loaded only by propeller swirl, which would be weak that far upstream. The dorsal wake would therefore be weaker than the wake from the two upper surfaces. The two upper airfoils were relatively large and had a 2° angle of attack.

I-tail— The I-tail was a simple vertical tail fin. Figures 22(a)-(c) and figures 23(a)-(c) show the increase in spectra levels and harmonic levels caused by the I-tail. The propeller empennage spacing was closer than was used for the Y-tail measurements, but the trends are similar. The higher harmonics of blade-passage noise are increased by the tail. The greatest effect is in the downstream direction because the propeller-alone tones were weakest in that direction. The interaction noise actually radiated strongly in all directions.

Time signatures— The acoustic pressure time signatures give a different perspective on the empennage/propeller interaction noise. Figures 24(a)-(c) compare

time traces of typical sound waves acquired from many averages of the data synchronously sampled at the rate of the blade-passage frequency. The blade-passage frequency recorded at microphone 12 was converted to a series of timing pulses and was used to trigger the HP 5423 analyzer. The data have not been corrected for distance or other effects. Comparing the noise radiated to 105° toward microphone 7 (in the flow) and microphone 5 (out of flow) along virtually the same path (figs. 24(a) and (b)), we see a substantial distortion of the wave shape by the shear layer. The effect may be confused by shear-layer-induced noise on microphone 7 or by floor reflections as previously discussed. However, the data from microphones 7 (in the flow) and 12 (out of flow) are reasonably similar, which confirms the previous conclusion that the in-plane microphones out of flow (microphones 11 and 12) captured the cleanest data of all the out-of-flow microphones either because of relative distance from the floor or because of minimal shear-layer effects in the direction normal to the shear layer.

When we concentrate on data from inside the flow and from microphone 12 outside the flow, the acoustic pressures plotted in the time domain can be used to reveal the empennage/propeller interaction effects. Figure 25 shows the acoustic pressures measured by microphones 9, 12, and 8 ($\theta = 15, 96, \text{ and } 140^\circ$), while the propeller alone was operating at 8200 rpm and with 62 m/sec windspeed. Because the data were recorded at microphones not equidistant from the propeller, the time traces were normalized to equal distance and proper phase based on estimated decay rates and propagation times. The phase relationships could easily be erroneous because of the miscalculation of propagation time of sound refracted by the shear layer, so the discussion will focus on the relative amplitudes. Of the three signals, only the one recorded by microphone 12 passed through the shear layer. The in-flow microphone data (microphones 8 and 9) show random noise from turbulence superimposed on the low-frequency acoustic signal. The data clearly show the strong sound pressure to the side of the propeller, relative to the upstream and downstream radiation. This is characteristic of thickness noise, although steady-loading rotational noise could also be present at the fundamental frequency. It is clear that the upstream sound was greater than the downstream sound.

Figures 26(a)-(c) show the effect of the Y-tail, V-tail, and I-tail on the sound pressure trace to the side of the propeller ($\theta = 96^\circ$). The data show that the Y-tail and V-tail interactions were similar and had little effect on the fundamental shape of the pressure signature. This is consistent with the spectra (fig. 18(b), for example), which showed little effect of the empennages on the first several harmonics of blade-passage noise. Ahmadi (1984) came to a similar conclusion in a study of blade-vortex

interactions with a model helicopter tail rotor. The details of the pressure signatures in figures 26(a)-(c) were changed by the two empennages, however, which caused changes in the higher harmonics of the spectra. The I-tail altered the peak of the pressure time trace in a dramatic fashion, which is consistent with the spectral plots (fig. 22(b)) and the high interaction noise in the higher harmonics. The time domain data illustrate that the Y-tail and I-tail had different interaction effects. It is proposed that these differences may be explained by directivity effects dictated by the azimuthal orientation of the empennage. This will be explored in the next section.

Figures 27(a)-(c) and figures 28(a)-(c) show the effects of the three empennages on the time signatures in the upstream and downstream directions, respectively. In the upstream direction (figs. 27(a)-(c)), the Y-tail had a somewhat greater effect on the sound radiation than the V-tail did, presumably because of the weak dorsal fin wake interaction with the propeller. The magnitude of the time trace with the V-tail installed was comparable to the propeller-alone noise, although the differences in signature shape resulted in higher harmonic interaction noise (fig. 20(a)). Downstream (figs. 28(a)-(c)), the interaction noises from the three empennages were fairly similar. In general, the upstream noise was somewhat stronger than the downstream noise.

Comparison of acoustic spectra and directivity-
The acoustic directivity showed that (1) in the plane of the propeller, the interaction noise tended to radiate in the direction normal to the empennage surface, with a maximum in the direction of the advancing blade; and (2) in the horizontal plane, the interaction noise from a vertical empennage (I-tail) radiated fairly uniformly in all directions. These and related results will be explained in the following discussion.

Comparison plots of the harmonic levels for the three empennages at similar empennage/propeller spacings are shown in figures 29(a)-(f). Figures 29(a)-(c) correspond to propeller/empennage spacings of 232 to 251 mm and figures 29(d)-(f) correspond to spacings of 111 to 175 mm. Because of the larger chord, the normalized I-tail spacing, x'/c' , was smaller than that of the other empennages in these comparisons. The harmonic levels from the Y-tail and V-tail were very similar since the only difference between the two configurations was the dorsal fin, which had a relatively weak wake, as previously discussed.

When the harmonic levels of the I-tail are compared with those from the other empennages in figure 29, the data do not show a consistent difference in noise in the first five or six harmonics. In the higher harmonics, however, the propeller noise from the I-tail interactions radiating upstream and downstream were 5-15 dB lower than

from the other empennages. In the plane of the propeller ($\theta = 96^\circ$), however, the I-tail generated the most noise in the higher harmonics by around 5 dB because of the decrease in Y-tail and V-tail noise (figs. 29(c) and (f)). In other words, the I-tail-induced noise was fairly uniform in all directions, but the Y-tail and V-tail noise decreased in the plane of the propeller.

These directivity effects indicate that pusher-propeller noise varies in both the horizontal plane (θ) and the vertical plane (φ) containing the propeller. The horizontal directivity of the propeller-alone noise clearly shows the maximum noise radiation (at low frequencies) in the plane of the propeller (see fig. 18(b)). Figures 29(a)-(c) show that with the empennages in place the lower harmonic noise is still maximum in the plane of the propeller, but radiation of the harmonic levels for $n > 4$ depend on the empennage geometry. The I-tail directivity is more or less uniform whereas the Y- and V-tail directivity is stronger upstream and downstream than in the propeller plane. Examination of the experimental setup shows that the in-plane microphone 12 was 30° above the horizon looking from the propeller, whereas the upstream and downstream microphones 9 and 8 were at the same height as the propeller. If we consider the normal vector of each empennage surface, we find that microphone 12 was closer to the I-tail normal vector than either of the two upper surfaces of the Y-tail. Thus, if the propeller interaction noise tended to radiate in a direction parallel to the empennage normal vector, the Y-tail noise at microphone 12 would be lower than the I-tail noise, which is what was measured. This directivity pattern is consistent with a dipole noise source on the propeller blade, which is more or less perpendicular to the chord, and has its greatest strength when the blade passes through the empennage wake.

In other words, the noise variation in the vertical plane containing the propeller depends on the angle formed at the propeller axis between the span of an empennage section and the microphone direction. Block and Gentry (1986) showed that the noise from an upstream pylon was minimum along a line parallel to the pylon span. Figures 30(a)-(d) are acoustic directivity plots in the plane of the propeller acquired by operating the model with I-tail upright and then rolled 90° onto its side. That gave eight noise measurements on a circle using four microphones. The first four harmonics of blade-passage frequency show little variation with azimuth (fig. 30(a)). The higher harmonics in figure 30(b), however, show a directivity peak between 210 and 270° (270° is to the left facing upstream) that is consistent with the results of Block and Gentry (1986), at least on one side of the model. That is, the peak interaction noise in the vertical plane radiates perpendicular to the empennage surface. The lack of a clear peak at 90° suggests

that the noise was greater on one side of the empennage than on the other. And of the two sides, the greatest noise occurred along a surface-normal vector pointing in the direction of the advancing blade which just passed the empennage trailing edge. The Y-tail noise directivity in figure 30(d) shows maximum noise for higher harmonics occurring at $\phi = 180$ and 300° (and a minimum at 240° where microphone 12 was located), which agrees roughly with acoustic lobes to be expected from the blades passing the upper empennage surfaces.

To summarize the directivity effects, the data showed that in the vertical plane containing the propeller:

1. The maximum interaction noise in the higher harmonics tended to be normal to the empennage surface, and the minimum noise was parallel to the empennage surface. The lower harmonic directivity did not show a clear pattern.

2. Along the surface normals, the greatest higher harmonic noise occurred in the direction of the advancing blade that just passed the empennage trailing edge.

In the horizontal plane:

1. The propeller-alone noise was maximum to the side of the propeller and dominated the empennage/propeller-interaction noise in that direction. This is indicative of blade-thickness noise and steady-loading noise.

2. The higher harmonics of interaction noise ($n > 4$) radiated fairly uniformly in all directions for the I-tail, the only empennage surface that was perpendicular to the microphone array.

3. The low propeller in-plane noise from the Y- and V-tails ($n > 4$) was related to the orientation of the upper surfaces, which put the in-plane microphone in a weak radiation direction (see item (1) above).

Tail loading—Increasing the empennage angle of attack and, thereby, its loading should increase the wake properties which cause the empennage/propeller-interaction noise. This was verified by increasing the Y-tail incidence from 1 to 6° , as measured in the plane perpendicular to the surface near the tip, and then operating the propeller in the wake. Figure 31(a) shows that the harmonic levels at $\theta = 15^\circ$ increased 3-5 dB because of higher tail incidence at all but the second harmonic. The data were acquired with a small empennage/propeller spacing of 112 mm. With a 305-mm spacing, the higher tail incidence caused the noise to increase only 1-5 dB as shown in figure 31(b). These interaction effects were slightly stronger upstream and downstream of the propeller than to the side.

Empennage/propeller axial separation—An important objective of this study was to measure the propeller noise variation as the spacing between the empennage trailing edge and propeller was varied. Fig-

ure 32(a) shows that the noise at $\theta = 15^\circ$ decreased as the Y-tail/propeller spacing was varied from 135 mm to 600 mm, although the trend is confused by data scatter. Figure 32(b) shows a weaker effect of empennage spacing on the noise at microphone 12 in the propeller disk plane. Figure 32(c) gives a clearer picture at $\theta = 140^\circ$ and indicates that the noise at all harmonics decreased as spacing increased. The mean spacing varied from 0.38 to 1.99 chords. The interaction noise trends upstream ($\theta = 15^\circ$) and downstream ($\theta = 140^\circ$) were more or less similar except for the scatter in the upstream microphone data. The I-tail results were similar except that, because of the large chord of the I-tail, the empennage/propeller separation distance normalized by chord was smaller for the I-tail case. Figure 32(d) shows that the closest normalized spacing of 0.16 caused the interaction noise from the I-tail to go up several decibels compared to the larger spacings.

The separation effect is easier to see in plots of noise decay versus distance at $\theta = 140^\circ$ for blade-passage harmonics 1-4 in figure 33(a) and harmonics 5-8 in figure 33(b). The changes in noise are plotted relative to the harmonic levels recorded with the closest spacing of $x'/c' = 0.38$. In general, there was a steady decay of sound of around 3-5 dB as the spacing was increased from 0.38 to 1.0 mean chord. Beyond a spacing of 1.0 chord, the sound decay was nil except for the highest harmonic. Thus, these limited data suggest that the empennage/propeller interaction is strong for spacings less than an average empennage chord, and become rapidly weaker at greater spacings. This is similar to fan rotor/stator interaction effects reported by Kramer et al. (1972).

Block and Gentry (1986) measured the noise of an SR-2 pusher propeller interacting with an upstream pylon using gap-to-eylon chord spacings of 0.1 and 0.3, which are considerably smaller spacings than were used in the present study. They showed that increasing the normalized spacing from 0.1 to 0.3 caused the forward-radiated noise to decrease around 10 dB and the aft-radiated noise to decrease around 5 dB. We didn't see those kinds of differences, upstream and downstream. But if we use their average noise decrease of 7.5 dB, we can combine their results with ours providing we extrapolate from $x'/c' = 0.3$ to 0.38. Figures 33(a) and (b) indicate that such an extrapolation would give roughly 2.5 dB decay from $x'/c' = 0.3$ to 0.4. Thus, if the results of Block and Gentry (1986) and the present study are consistent, one could conclude that pusher-propeller noise decreases around 10 dB as the empennage-to-propeller spacing increases from 0.1 to 0.4 empennage chord, and decreases another 3-5 dB as the spacing increases to 1.0 chord. Beyond that spacing, the interaction noise is small in most cases (an exception was the eighth harmonic in figure 33(b), which may be anomalous). The I-tail data taken as close as

$x'/c' = 0.16$ are consistent with the above results. A summary plot showing that noise decay is given in figure 34.

Empennage/propeller vertical separation— The vertical location of the propeller relative to the fuselage tail cone was varied by moving the motor support strut up and down. The Y-tail was on the model. Figure 35 shows that displacements of 76 mm, up or down, affected the noise radiation, but not in a clear manner. Some harmonics went up and some went down. Examination of all the microphone data indicates that with the propeller hub 76 mm below the fuselage cone, the noise increased 1-3 dB at many harmonics. On the average, that location caused the most interaction noise.

Correlation of Acoustics and Aerodynamics

Wake deficit— The aerodynamic measurements reported by Horne and Soderman (1988) included surveys of the empennage mean-wake velocity distribution with and without the propeller operating. It was discovered that the propeller did not have a significant effect on the wake properties aside from an acceleration of the wake into the propeller. On the other hand, the acoustic results reported here show that the wake had a strong effect on the propeller noise radiation.

Figure 36 shows typical wake-normalized velocity profiles measured with a pitot/static-pressure probe at approximately the propeller tip height ($y = 305$ mm) and at empennage/probe separation distances (x_p) from 7.6 to 264 mm. The propeller was removed. The wake profile started with a strong, narrow deficit and gradually broadened and weakened as it moved downstream, as expected. Both parameters, wake deficit amplitude and wake width, could affect noise from the propeller. The magnitude of the wake deficit affects the magnitude of the unsteady propeller loading, which of course radiates as noise. And, narrow flow distortions cause rapid changes in blade loading and thereby generate propeller noise over a broader frequency range than do wide flow distortions. Other flow surveys, including more Y-tail wake measurements, are presented by Horne and Soderman (1988).

Figure 37 summarizes the decay of the maximum wake deficit, \bar{U}_{max} of the I-tail and Y-tail with stream-wise distance. \bar{U}_{max} is the maximum normalized wake deficit, \bar{U} , determined from plots such as figure 36. The wake intensity decayed rapidly out to a distance of 100 mm (or around 0.25 to 0.33 empennage chord). Beyond that distance, the decay rate with distance was much more gradual. Note that the Y-tail wake was weaker than the I-tail wake because of the smaller chord and thickness of the Y-tail. This is consistent with the

theoretical wake-deficit model of Soderman and Horne (1988), which showed that \bar{U}_{max} has the following functional relationship to empennage chord, drag coefficient, and distance downstream.

$$\bar{U}_{max} \propto \left(\frac{cC_d}{2x_p} \right)^{1/2} \quad (2)$$

Figure 38 shows the decay of wake width with distance from the two empennages, where the wake width, b_w , was measured at the mid-height of the deficits. The wake-width spread is much more linear than is the peak-velocity deficit decay. The wake width increased linearly from about 8 mm near the empennage trailing edge to about 20 mm at a distance of 450 mm downstream. When the aerodynamic wake decay data are compared with the acoustic decay data (fig. 34), it appears that the wake-deficit-magnitude decay correlates better with the acoustic variation than does the wake-width decay data. Both the wake-deficit magnitude and the propeller noise decay rapidly as the propeller is moved downstream 0.5 empennage chord from the empennage trailing edge.

Turbulence— Propeller acoustic radiation consists of harmonically related tones and broadband noise. The harmonic components can be related to propeller interactions with the steady (uniform and nonuniform) inflow-velocity field. The turbulent velocity field, which contributes to the broadband noise, also can affect the harmonic noise if the turbulent eddies have sufficient length scale and amplitude to induce nearly periodic blade loading.

Figures 39(a)-(c) show the turbulence in the x , y , and z directions measured with a hot wire during surveys through the I-tail wake. The turbulence values u' , v' , and w' are normalized by the free-stream velocity U_∞ . The surveys were made cross stream at several locations aft of the empennage in a manner similar to the wake mean-velocity surveys. The data indicate that the maximum turbulence occurred in the center of the wakes. At a distance $x_p = 44$ mm downstream of the empennage trailing edge, the maximum normalized turbulence intensity, w'/U_∞ , was 0.05, and decayed to 0.03 at $x_p = 288$ mm. Since the decay with distance was fairly gradual compared to the rapid decrease in propeller noise over that distance, it is likely that the turbulence was not a strong factor in the generation of noise harmonics 1-8.

Typical frequency spectra (10 log (rms voltage²)) from a single 45° wire are presented in figure 40. The spectra were generated with a constant-bandwidth analyzer set at a nominal 25-Hz filter width. Data below 2 Hz were filtered out. The data were acquired near the propeller tip height ($Y = 305$ mm), inside and outside the

vertical tail-fin wake at two streamwise locations. The propeller-on data were acquired 106 mm upstream of the propeller tip, and the propeller-off data were acquired 274 mm upstream of the propeller station. Those two survey stations were 277 mm and 109 mm downstream of the vertical fin, propeller on and off, respectively. The spectra outside the wake (76 mm from the center of the wake) show strong periodic disturbances from the propeller. The peaks in the spectrum occur at multiples of the blade-passage frequency, which was 550 Hz (number of blades times revolutions per second). The hot-wire spectra in the wake are much more broadband, although the propeller disturbances are visible at the first two harmonics of the propeller blade-passage interactions. The peak in the wake spectrum at 1.53 kHz corresponds to a disturbance period, T , of 6.54×10^{-4} sec/cycle ($T = 1/f$). If one assumes that that disturbance is related to a turbulent eddy traveling at a velocity equal to U_{wake} in the center of the wake (40 m/sec), then the eddy length, L , can be computed from

$$L = U_{\text{wake}} \times T = 40 \times 6.54 \times 10^{-4} \\ = 0.0261 \text{ m or } 26 \text{ mm} \quad (3)$$

It should be noted that this eddy length is roughly comparable to the measured wake width at the mid-height of the wake deficit (see fig. 38). If that eddy moves at 40 m/sec, it would pass through the blade disc before two successive blades could intersect the eddy. Thus, the tonal contribution from propeller interaction with turbulence in that part of the turbulence spectrum would be nil. Eddies at lower frequencies would have adequate length for multiple blade intersections, but the in-wake data of figure 40 (propeller off) shows a random distribution of turbulence energy; no coherent eddy scale can be clearly seen outside the broad peak at 1.53 kHz. Furthermore, the turbulence decay with distance did not match the noise source decay with empennage/propeller spacing. Hence, turbulence was not a strong factor in the periodic noise generation, although it did influence the broadband noise levels slightly as evidenced by the small increase in high-frequency broadband noise resulting from installation of the various empennages.

As expected, the turbulence intensities in the wake were much stronger than those out of the wake. The difference in turbulence level, propeller on and propeller off, was due to the unequal distance from the empennage to the hot wire.

Implications for Propeller Noise Prediction

One of the objectives of the study was to compare the experimental results with an analytical noise-prediction method to see whether the pusher-propeller case could be properly modeled. Most propeller noise-prediction methods consider the propeller to be operating in free air with no in-flow disturbances. This is the usual situation for a tractor propeller. However, methods exist for predicting the unsteady loading noise. Jonkouski, Horne, and Soderman (1983) describe a simple dipole noise model resulting from ingestion of a small gust by a propeller. Viterna (1981) describes a more general equation for unsteady loading noise of a wind turbine in a tower wake using the theory of Lawson (1970). Lawson's theory predicts radiated acoustic pressure by a Fourier transformation of the blade force variation during the blade revolution. A lift response function of Filotas (1969) (see also Blake, 1986) can be used to determine the blade response to the empennage wake intersection. Estimates of blade-passage harmonic noise levels were made using Viterna's method after replacing his simple blade-loading model for a wind turbine, which is not strictly correct for a thrusting propeller, with the lifting line theory of Larrabee and French (1983), developed for the estimation of propeller performance. Given the in-flow velocity distribution of the propeller (from Horne and Soderman, 1988), the blade loads at 20 radial stations were computed for each azimuthal position specified. The steady and unsteady load distribution was then transformed into radiated noise. A computer code was developed for the aerodynamic loading and noise prediction and is listed in the Appendix.

Figure 41(a) shows the computed and measured propeller in-plane harmonic noise levels with and without a wake interaction from the I-tail. The propeller/empennage spacing was $x' = 89$ mm. Because the analytical model did not include thickness noise, the predicted noise falls a few decibels below the measurements, but has the same roll-off with increasing harmonic number as the data. The important interaction effects are predicted. That is, the predicted first three harmonics of blade passage noise are not affected by the wake, but the higher harmonic levels increase because of wake interaction. This agrees with experimental results of this study. Figure 41(b) shows similar agreement between the theory and data for upstream noise radiation. Therefore, pusher-propeller noise predictions must include unsteady loading effects. Fortunately, this simple analysis indicates that the prediction should not be difficult if the spanwise blade loading and loading variation around the propeller disk can be estimated.

CONCLUSIONS

Measurements of pusher-propeller noise in the NASA Ames 7- by 10-Foot Wind Tunnel show that the interaction of empennage wakes with the propeller had a strong effect on the radiated noise above the first few harmonics of the blade-passage noise. It was deduced that the noise was generated by unsteady blade loads on the propeller as the propeller passed through the mean velocity deficit of the wake. The turbulence in the wake had only a minor effect on the propeller broadband noise. The first few harmonics of in-plane noise were dominated by thickness and steady-loading noise. The higher harmonics of interaction noise dominated the propeller noise in all directions evaluated. The propeller in-plane noise was maximum in a direction perpendicular to the empennage surface and minimum in a direction parallel to the span.

As the separation between empennage was increased from 0.38 to 1.0 mean empennage chord length, the noise decreased 3-5 dB. Beyond 1.0 chord, the noise decay with increased spacing was small. For empennage/propeller spacings less than 0.38 empennage chord, the results of Block and Gentry (1986) are plotted with the data from this study to show interaction effects over a large range of separation distances. The interaction noise increased when the tail loading was increased.

A simple theory for propeller noise, which incorporated an aerodynamic and acoustic unsteady loading model, gave trends consistent with the measured data. The inflow velocity distribution measured during the empennage wake surveys was critical to the proper modeling of the unsteady blade loading and radiated noise.

Ames Research Center
National Aeronautics and Space Administration
Moffett Field, California 94035-1000
March 14, 1990

REFERENCES

- Ahmadi, A. R.: An Experimental Investigation of the Chopping of Helicopter Main Rotor Tip Vortices by the Tail Rotor. NASA CR-177338, 1984.
- Amiet, R. K.: Correction of Open Jet Wind Tunnel Measurements for Shear Layer Refraction of Sound. AIAA Paper 75-532, AIAA 2nd Aeroacoustics Conf., Hampton, VA, March 1975.
- Blake, W. K.: Mechanics of Flow-Induced Sound and Vibration—Volume II, Complex Flow-Structure Interactions. Academic Press, Inc., 1986, p. 743.
- Block, P. J. W.: Analysis of Noise Measured From a Propeller in a Wake. NASA TP-2358, 1984.
- Block, P. J. W.: Noise Radiation Patterns of Counter-Rotation and Unsteadily Loaded Single-Rotation Propellers. *J. Aircraft*, vol. 22, no. 9, Sept. 1985, pp. 776-783.
- Block, P. J. W.: Pusher Propeller Noise Directivity and Trends. AIAA Paper 86-1929. AIAA 10th Aeroacoustics Conf., Seattle WA, July 1986.
- Block, P. J. W.; and Gentry, C. L., Jr.: Directivity and Trends of Noise Generated by a Propeller in a Wake. NASA TP-2609, 1986.
- Dittmar, J. H.; Blaha, B. J.; and Jeracki, R. J.: Tone Noise of Three Supersonic Helical Tip Speed Propellers in a Wind Tunnel at 0.8 Mach Number. NASA TM-79046, 1978.
- Dittmar, J. H.; Jeracki, R. J.; and Blaha, B. J.: Tone Noise of Three Supersonic Helical Tip Speed Propellers in a Wind Tunnel. NASA TM-79167, 1979.
- Dittmar, J. H.: A Comparison Between an Existing Propeller Noise Theory and Wind Tunnel Data. NASA TM-81519, 1980.
- Filotas, L. T.: Response of an Infinite Wing to an Oblique Sinusoidal Gust: A Generalization of Sears' Problem. NASA SP-207, 1969, pp. 231-246.
- Hersh, A. S.; Soderman, P. T.; and Hayden, R. E.: Investigation of Acoustic Effects of Leading-Edge Serrations on Airfoils. *J. Aircraft*, vol. 11, no. 4, April 1974, pp. 197-202.
- Horne, W. C.; and Soderman, P. T.: Flow-Field Survey of an Empennage Wake Interacting With a Pusher Propeller. NASA TM-101003, 1988.
- Jonkouski, G. C.; Horne, W. C.; and Soderman, P. T.: The Acoustic Response of a Propeller Subjected to Gusts Incident from Various Inflow Angles. AIAA Paper 83-0692, April 1983.
- Kramer, J. J.; Hartmann, M. J.; Leonard, B. R.; Klapproth, J. F.; and Sofrin, T. G.: Fan Noise and Performance. NASA SP-311, 1972, pp. 7-61.
- Larrabee, E. E.; and French, S. E.: Minimum Induced Loss Windmills and Propellers. *Wind Engineering Indust. Aerodynam.*, vol. 15, no. 1-3, Dec. 1983, pp. 317-327.
- Lowson, M. V.: Theoretical Analysis of Compressor Noise. *J. Acoust. Soc. Amer.*, vol. 47, no. 1., pt. 2, 1970, pp. 371-385.
- Martin, R. M.; Brooks, T. F.; and Hoad, D. R.: Reduction of Background Noise Induced by Wind Tunnel Jet Exit Vanes. *AIAA J.*, vol. 23, no. 10, Oct. 1985, pp. 1631-1632.
- Schlinker, R. H.; and Amiet, R. K.: Rotor-Vortex Interaction Noise. NASA CR-3744, 1983.
- Soderman, P. T.: Test-Section Noise of the Ames 7- by 10-Foot Wind Tunnel No. 1. NASA TM-X-73-134, 1976.
- Soderman, P. T.; and Høglund, L. E.: Wind-Tunnel Fan Noise Reduction Including Effects of Turning Vanes on Noise Propagation. AIAA Paper 79-0642, AIAA 5th Aeroacoustics Conf., Seattle WA, March 1979.
- Soderman, P. T.; and Olson, L. E.: Large-Scale Aeroacoustic Research—Feasibility and Conceptual Design of Test-Section Inserts for the Ames 80- by 120-Foot Wind Tunnel. NASA TP-3020, 1990.
- Trebbles, W. J. G.; and Williams, J.: Propeller Noise at Model- and Full-Scale. *J. Aircraft*, vol. 20, no. 1, Jan. 1983, pp. 34-41.

Viterna, L. A.: The NASA-LeRC Wind Turbine Sound Prediction Code. NASA TM-81737, 1981. (also DOE/ NASA/20366-1)

Wilby, J. F.; and Wilby, E. G.: Wind Tunnel Acoustic Study of a Propeller Installed Behind an Airplane Empennage: Data Report. NASA CR-177335, 1985.

APPENDIX

Analytical Prediction of Propeller Blade Loading and Noise-Generation Computer Code WTPROP2

Program WTPROP2

The data acquired in this study were compared with an analytical prediction of propeller noise. A pusher propeller interacting with steady flow field and a superimposed wake was modeled. The basic theory and computer code were developed by Viterna (1981) for the prediction of wind-turbine noise, and has been modified by Soderman and Horne. Propeller noise at harmonics of blade-passage frequency are computed from a Fourier analysis of the blade force variation using the method of Lawson (1970). However, the aerodynamic loading model of Viterna (1981) for a wind turbine, which is not strictly suitable for a thrusting propeller, was replaced by the lifting-line theory of Larrabee and French (1983). Given a velocity inflow distribution around the propeller disc (from the wake studies of Horne and Soderman, 1988), the propeller-loading variation is computed using the method of Larrabee and French (1983) coupled with a Filotas function for gust response. The theory of Larrabee and French (1983) gives the radial distribution of propeller blade loading at each azimuth location and is listed in WTPROP2 as Subroutine PROPA.¹ That subroutine, in turn, contains Subroutines CLCD and SIMPSN. The code is written in FORTRAN.

Inputs for WTPROP2 are described in the code and are input as DATA elements or as line elements in the program.

Inputs for Subroutine PROPA are read from an input file PROPA.INP as follows:

- Number of blades
- Air density
- Rotational speed (RPM)
- Propeller radius
- Forward speed
- Chord distribution at radial stations
- Pitch angle at radial stations
- A1, first angle² in linear section of blade lift curve (C_l vs α)
- A2, last angle in linear section of blade lift curve (C_l vs α)
- A3, angle at zero lift in linear section of blade lift curve (C_l vs α)
- C_l at A1
- C_l at A2
- C_d , drag coefficient at A3
- C_2 , $dC_d/d(\alpha^2)$ between A1 and A2

A sample input file is listed as PROPA.INP after the main program.

A sample output of the PROPA subroutine is listed as PROPA.OUT after the main program.

¹The subroutine was written by F. Felker of the Rotary Wing Aeromechanics Branch, NASA Ames Research Center.

² α is the blade angle of attack in this appendix.

```

C
C      WTPROP2
C
C      THIS PROGRAM CALCULATES THE SOUND LEVEL OF A PROPELLER
C      USING THE METHOD OF WTSOUND WIND TURBINE NOISE CODE
C      FROM NASA LEWIS (NASA TM-81737)
C
C      THE BLADE LOADING IS FROM LARRABEE AND FRENCH
C
C      P. SODERMAN 1/28/88
C
C      INPUT PARAMETERS
C
C      RPM          PROPELLER SPEED
C      R            PROPELLER RADIUS, FT
C      B            NUMBER OF BLADES
C      SO           DISTANCE FROM PROPELLER, FT
C      DELTA        AZIMUTH ANGLE, DEG (RELATIVE TO DOWNSTREAM DIRECTION)
C      PHI          ALTITUDE ANGLE, DEG (RELATIVE TO HORIZONTAL)
C      VHUB         FREE STREAM VELOCITY AT HUB, FT/S
C      CHORD        BLADE CHORD AT 3/4 RADIUS, FT
C      SLI          BLADE LIFT CURVE SLOPE, 1/RADIAN
C      EFFR         RADIUS AT SPANWISE STATION, FT
C
C      DIMENSION DB(30,20), PRMS(100), DBT(20), PSI(3600)
C      DIMENSION PSQ(30), DBHARM(30)
C      INTEGER IWK(7350), IER, MCOEF, NPSI
C      REAL*8 CKRS, BJ(1800), MPHFPS, CKRS2(30), BJO(30), SUMSQ
C      REAL*8 DTC(21), DPC(21), VHUB, RPM, CL(21), CD(21), ALPHA(21)
C      REAL*8 THRUST, POWER, EFFICIENCY, CT, CP, EFFR(21), RR(21)
C      REAL TA(3600), QA(3600)
C      REAL WK(7350), PSIN, FTA(3600), FTB(3600), FQA(3600), FQB(3600)
C      COMPLEX X, Y, Z, C1, C2, C3, C4, C5, C6, C7, C8, C9, C10, TPP, DPP, DPN, SUM
C      COMPLEX TERM, TERM1, TERM2, SEARS(1800)
C      COMPLEX XXT(1800), XXQ(1800)
C      CHARACTER*8 TIMEX
C      CHARACTER*9 DATEX
C
C      SOUND SPEED, AIR DENSITY
C      DATA C, RHO/1120., 0.00234/
C
C      GUST PARAMETER: 0. WAKE, 1. NO WAKE
C      DATA GUST/0./
C      DATA NHAR/30/
C      DATA PSIN/3600./
C
C      IPRT=9
C      OPEN(UNIT=9, FILE='WTPROP2.OUT', STATUS='NEW', FORM='FORMATTED')
C      REWIND 9
C      PI=3.14159
C      DEGRAD=PI/180.
C
C      THESE VARIABLES CORRESPOND TO PUSHER PROP RUN 43.1 (I-TAIL)
C      RPM=8200.
C      R=0.97
C      B=4.
C      SO=14.
C      DELTA=15.
C      PHI=0.
C      VHUB=205.
C      CHORD=0.29
C      ETA=1.0E-30
C      X=(1., 0.)
C      Y=(0., 1.)
C      RPS=RPM/60.
C      DIA=2.*R
C      DELTA=DELTA*DEGRAD
C      PHI=PHI*DEGRAD

```

```

OMEGA=RPM*PI/30.
DPSI=360./PSIN
NPSI=IFIX(PSIN)
LOOPCOUNT=1
TBSUM=0.
QBSUM=0.
CALL DATE (DATEX)
WRITE (IPRT,4) DATEX
4 FORMAT (2X,A9,/)

C
C COMPUTE AERODYNAMICS OF BASELINE FLOW FIELD (NO WAKE)
C
C
C COMPUTE LOADING AT 18 SPANWISE STATIONS
C
CALL PROPA (VHUB,RPM,DTC,DPC,CT,CP,THRUST,POWER,
*EFFICIENCY,CL,CD,ALPHA,EFFR,LOOPCOUNT,IPRT)
C
C COMPUTE THRUST AND TORQUE AT EACH STATION
C
DO 100 I=3,20
LOOPCOUNT=LOOPCOUNT+1
TB=DTC(I)*0.05*RHO*RPS**2*DIA**4/B
PB=DPC(I)*0.05*RHO*RPS**3*DIA**5
QB=PB/(2.*PI*RPS)/B
TBSUM=TBSUM+TB*B
QBSUM=QBSUM+QB*B
RE=EFFR(I)*R
DRAG=QB/RE
VROT=RE*OMEGA
VRO=SQRT(VHUB**2+VROT**2)
ADVANCE=VHUB/(RPS*DIA)

C
C FIND AZIMUTH ANGLES FOR WHICH BLADE SECTION INTERSECTS WAKE
C ZDIST IS I-TAIL WAKE WIDTH
C
ZDIST=0.0328*1.2
YDIST=SQRT(RE**2+ZDIST**2)
ANGLE=ATAN(ZDIST/YDIST)/DEGRAD
ANGLE=FLOAT(IFIX((ANGLE+0.05)*10.))/10.
ANGLE2=90.+ANGLE
ANGLE3=90.-ANGLE

C
C CALCULATE UNSTEADY THRUST AND TORQUE DURING ONE REVOLUTION
C
DO 11 N=1,NPSI
PSI(N)=(N-1)*DPSI
C IF NOT IN WAKE USE BASELINE THRUST AND TORQUE
IF (PSI(N).LT.ANGLE3.OR.GUST.EQ.1.) THEN
    TA(N)=TB
    QA(N)=QB
    GO TO 10
END IF

C
VY=VHUB
IF (PSI(N).GT.ANGLE2) GO TO 7

C
C CALCULATE EFFECT OF EMPENNAGE WAKE
C
C WIND VELOCITY IS A FUNCTION OF ROTOR POSITION PSI
C
C WAKE PROFILE FOR I-TAIL (RUN 43.1)
C
SPSI=ABS(PSI(N)-90.)*DEGRAD
ZDIST=RE*SIN(SPSI)*1000.
VY=126.2821+1.0525*ZDIST-0.0881*ZDIST**2+

```

```

*0.0071*ZDIST**3-1.083*ZDIST**4*10.**(-4)
IF (VY.GT.VHUB) VY=VHUB
VRO=SQRT(VY**2+VROT**2)
C
C   CALCULATE THRUST AND TORQUE VARIATION WITH AZIMUTH
C
C   COMPUTE AERODYNAMICS OF FLOW FIELD (WITH WAKE)
C
CALL PROPA(VY,RPM,DTC,DPC,CT,CP,THRUST,POWER,
*EFFICIENCY,CL,CD,ALPHA,EFFR,LOOPCOUNT,IPRT)
C
7 CONTINUE
TA(N)=DTC(I)*0.05*RHO*RPS**2*DIA**4/B
PC=DPC(I)*0.05*RHO*RPS**3*DIA**5
QA(N)=PC/(2.*PI*RPS)/B
C
10 EPSIL=0.02
CALL TIME(TIMEX)
IF((PSI(N).GT.(ANGLE3-EPSIL).AND.PSI(N).LT.(ANGLE3+EPSIL))
*.OR.PSI(N).EQ.90..OR.(PSI(N).GT.(ANGLE2+10.-EPSIL).AND.
*PSI(N).LT.(ANGLE2+10.+EPSIL))) THEN
WRITE(IPRT,820) TIMEX
END IF
IF(((I.EQ.3).OR.(I.EQ.11).OR.(I.EQ.20)).AND.
*{(PSI(N).GT.(ANGLE3-EPSIL).AND.PSI(N).LT.(ANGLE3+EPSIL))
*.OR.PSI(N).EQ.90..OR.(PSI(N).GT.(ANGLE2+10.-EPSIL).AND.
*PSI(N).LT.(ANGLE2+10.+EPSIL))}) THEN
WRITE(IPRT,*) I
WRITE(IPRT,930) PSI(N),VY
WRITE(IPRT,932) PSI(N),ALPHA(I),CL(I),CD(I)
WRITE(IPRT,934) PSI(N),TA(N),QA(N),TB,QB
WRITE(IPRT,936) PSI(N),POWER,TBSUM,QBSUM,EFFICIENCY,
*ADVANCE
END IF
11 CONTINUE
C
820 FORMAT(2X,A8)
930 FORMAT(1X,' PSI =',F5.1,' VY =',F6.1)
932 FORMAT(1X,' PSI =',F5.1,' ALPHA =',F5.2,' CL =',F6.3,
*' CD =',F6.3)
934 FORMAT(1X,' PSI =',F5.1,' TA =',F6.3,' QA =',F6.3
*,' TB =',F6.3,' QB =',F6.3)
936 FORMAT(1X,' PSI =',F5.1,' POWER =',F6.1,' TBSUM =',
*F7.3,' QBSUM =',F7.3,/,13X,
*' ETTA =',F5.2,' ADV RATIO =',F5.2,/)
C
C   DETERMINE FOURIER COEFFICIENTS FOR THRUST AND TORQUE
C
NF=NPSI/2
MCOEF=NF
OPEN(UNIT=7,FILE='FILE7.DAT',STATUS='NEW',FORM='FORMATTED')
REWIND 7
DO 1000 K=1,NPSI
WRITE(7,*) TA(K),QA(K)
1000 CONTINUE
CLOSE(7)
CALL FFTRC(TA,NPSI,XXT,IWK,WK)
CALL FFTRC(QA,NPSI,XXQ,IWK,WK)
C
DO 21 K=1,NF+1
XXT(K)=CONJG(XXT(K))
XXQ(K)=CONJG(XXQ(K))
IF(K.EQ.1) XXT(1)=XXT(1)/2.
IF(K.EQ.1) XXQ(1)=XXQ(1)/2.
FTA(K)=REAL(XXT(K)*2.)/NPSI
FTB(K)=AIMAG(XXT(K)*2.)/NPSI

```

```

      FQA(K)=REAL(XXQ(K)*2.)/NPSI
      FQB(K)=AIMAG(XXQ(K)*2.)/NPSI
21 CONTINUE
C
C   CALCULATE EFFECT OF UNSTEADY AERODYNAMICS
C   PILOTAS APPROXIMATION TO SEARS FUNCTION
C
      SEARS(1)=X
      DO 12 NS=2,MCOEF
      SIGMA=OMEGA*(NS-1)*CHORD/2./VRO
      CS1=(1.+2.*PI*SIGMA)
      CS2=(1.-PI**2/2./CS1)*SIGMA
      SEARS(NS)=(X*COS(CS2)-Y*SIN(CS2))/SQRT(CS1)
      IF (GUST.EQ.1.) SEARS(NS)=X
12 CONTINUE
C
C   DETERMINE RMS PRESSURE VARIATION FOR EACH HARMONIC
C   USING LOWSON'S EQUATION
C
      NPMAX=0
      SUMSQ=0.
C
      DO 30 NN=1,NHAR
      CKNB=NN*B*OMEGA/C
      C1=2.*X*CKNB*0.35355/SO/PI
      CKRS=CKNB*RE*SIN(DELTA)
      CKRS2(NN)=CKRS
C
C   CALL BESSEL FUNCTION
C
      IF (EFFR(I).GT.0.15) GO TO 40
      IF (NN.LT.NHAR+1) MCOEF=CKRS*5.
      IF (NN.LT.20) MCOEF=CKRS*6.
      IF (NN.LT.10) MCOEF=CKRS*9.
      IF (NN.LT.5) MCOEF=CKRS*12.
      IF (NN.LT.3) MCOEF=CKRS*20.
      GO TO 42
40 IF (NN.LT.NHAR+1) MCOEF=CKRS*3.
      IF (NN.LT.20) MCOEF=CKRS*4.
      IF (NN.LT.10) MCOEF=CKRS*6.
      IF (NN.LT.5) MCOEF=CKRS*8.
      IF (NN.LT.3) MCOEF=CKRS*13.
42 IF (MCOEF.GT.NF) MCOEF=NF
13 CALL MMBSJN(CKRS,MCOEF,BJ,IER)
      IF (IER.NE.0) THEN
      MCOEF=MCOEF-1
      GO TO 13
      END IF
C
      WRITE(IPRT,14) IER,NN,CKRS,MCOEF
14 FORMAT(1X,'IER = ',I4,' STEP = ',I4,' CKRS = ',
      *F7.4,' MCOEF = ',I4,/)
      BJO(NN)=BJ(1)
      NBES=NN*B
      C9=BJ(NBES+1)*X
      C10=NN*B/CKNB/RE*X
      SUM=0.
      NB=NN*B
      NPLIM=MCOEF-1
C
      DO 20 NP=1,NPLIM
      IF(NP.GT.NPMAX) NPMAX=NP
      PPHI=NP*(PHI-PI/2.)
      C2=X*COS(PPHI)-Y*SIN(PPHI)
      C6=X*COS(PPHI)+Y*SIN(PPHI)
      NBESN=NN*B-NP
      IF ((NBESN+1).GT.-1) GO TO 15

```

```

      C3=-1.**ABS(NBESN+1)*BJ(ABS(NBESN+1))*X
      GO TO 17
15  C3=BJ(NBESN+1)*X
17  CONTINUE
      NBESP=NN*B+NP
      IF(BJ(NBESP+1).LT.1.0E-35) BJ(NBESP+1)=0.
      C7=BJ(NBESP+1)*X
      IF(CABS(C3).LE.ETA.AND.CABS(C7).LE.ETA) GO TO 20
      C4=COS(DELTA)*X
      C5=NBESN/CKNB/RE*X
      C8=NBESP/CKNB/RE*X
      TPP=(FTA(NP+1)*X+FTB(NP+1)*Y)*SEARS(NP+1)
      TPN=(FTA(NP+1)*X-FTB(NP+1)*Y)*SEARS(NP+1)
      DPP=(FQA(NP+1)*X+FQB(NP+1)*Y)*SEARS(NP+1)
      DPN=(FQA(NP+1)*X-FQB(NP+1)*Y)*SEARS(NP+1)
      TERM1=C2*C3*(C4*TPP-C5*DPP)
      TERM2=C6*C7*(C4*TPN-C8*DPN)
      IF(CABS(TERM1).LE.ETA) TERM1=(0.,0.)
      IF(CABS(TERM2).LE.1.0E-15) TERM2=(0.,0.)
      TERM=TERM1+TERM2
      SUM=SUM+TERM
20  CONTINUE
C
25  Z=C1*(SUM+C9*(C4*TB-C10*DRAG))
      PRMS(NN)=CABS(Z)
      IF(PRMS(NN).LE.0.) PRMS(NN)=4.177E-07
      DB(NN,I)=20.*ALOG10(PRMS(NN)/4.177E-07)
      IF(DB(NN,I).LT.0.) DB(NN,I)=0.
      SUMSQ=SUMSQ+PRMS(NN)**2
30  CONTINUE
C
      RMST=DSQRT(SUMSQ)
      IF(RMST.NE.0.) GO TO 80
      DBT(I)=0.
      GO TO 100
80  DBT(I)=20.*ALOG10(RMST/4.177E-07)
      IF(DBT(I).LT.0.) DBT(I)=0.
100 CONTINUE
C
C   COMPUTE TOTAL SOUND FROM ALL 18 SECTIONS OF BLADE
C   ASSUME IN PHASE PRESSURE ADDITION ALONG THE SPAN
C
      DO 108 NN=1,NHAR
      SUMM=0.
      DO 105 I=3,20
      PSQ(NN)=10.**(DB(NN,I)/20.)
      SUMM=SUMM+PSQ(NN)
105  CONTINUE
      DBHARM(NN)=20.*ALOG10(SUMM)
108  CONTINUE
C
C   WRITE INPUT AND OUTPUT
C
      WRITE(6,550)
      IF(GUST.EQ.0) WRITE(IPRT,555)
      IF(GUST.EQ.1) WRITE(IPRT,557)
      WRITE(IPRT,620) RPM
      WRITE(IPRT,630) R
      WRITE(IPRT,640) B
      WRITE(IPRT,650) SO
      WRITE(IPRT,657) VHUB
      WRITE(IPRT,659) DELTA/DEGRAD
      WRITE(IPRT,660) PHI/DEGRAD
C
C   TABULATE HARMONIC LEVELS
C

```

```

WRITE(IPRT,2000)
C
DO 158 I=3,11
DO 157 NN=1,NHAR/3
WRITE(IPRT,2005) I,NN,DB(NN,I),I+9,NN,DB(NN,I+9)
157 CONTINUE
WRITE(IPRT,685) DBT(I),DBT(I+9)
158 CONTINUE
WRITE(IPRT,2006)
DO 160 NN=1,NHAR
WRITE(IPRT,2007) NN,DBHARM(NN)
160 CONTINUE
C
DO 900 I=1,NHAR
C
WRITE(IPRT,950) I,CKRS2(I),BJO(I),FTA(I),FTB(I),FQA(I),FQB(I)
WRITE(IPRT,951) REAL(SEARS(I)),AIMAG(SEARS(I))
900 CONTINUE
C
550 FORMAT(//////,' WTPROP SOUND LEVEL PROGRAM - I TAIL RUN 43.1')
555 FORMAT(/,' 120% WAKE WIDTH')
557 FORMAT(/,' NO GUST CASE *****',/)
620 FORMAT(' ROTOR SPEED, RPM ',F10.1)
630 FORMAT(' ROTOR RADIUS, FT ',F10.2)
640 FORMAT(' NUMBER OF BLADES ',F10.1)
650 FORMAT(' DISTANCE FROM ROTOR, FT',F10.1)
657 FORMAT(' WIND SPEED AT HUB, FT/S ',F10.1)
659 FORMAT(' AZIMUTH, DELTA, DEG ',F10.1)
660 FORMAT(' ALTITUDE, PHI, DEG ',F10.1)
685 FORMAT(' OASPL',F10.0,9X,' OASPL',F10.0,/)
2000 FORMAT(' HARMONIC SOUND LEVEL, dB',/)
2005 FORMAT(2X,I2,2X,I2,6X,F5.1,9X,I2,2X,I2,6X,F5.1)
2006 FORMAT(/,' TOTAL HARMONIC SOUND LEVELS, dB',/)
2007 FORMAT(2X,I2,10X,F5.1)
950 FORMAT(1X,'I = ',I2,' CKRS = ',F7.4,' BJO(I) = ',F7.4,
*' FTA(I) = ',F7.4,' FTB(I) = ',F7.4,' FQA(I) = '
*,F7.4,' FQB(I) = ',F7.4)
951 FORMAT(1X,' RE(SEARS(I)) = ',F9.7,' IM(SEARS(I)) = ',F9.7)
CLOSE(9)
STOP
END
C
C*****
SUBROUTINE PROPA(V,RPM,DTC,DPC,TC,PC,THRUST,POWER,
*ETA,CL,CD,ALPHA,RR,LOOPCOUNT,IPRT)
C
C
C PROGRAM TO ANALYZE THE PERFORMANCE OF AN ARBITRARY PROPELLER
C AT A SPECIFIED THRUST OR POWER, AND ARBITRARY OPERATING CONDITION
C
C METHODOLOGY BASED ON LARRABEE PAPERS
C PROGRAM USES 21 RADIAL STATIONS: 0, 0.05, 0.1,... ..0.95, 1.0
C INPUT IS IN FILE "PROPA.INP"
C OUTPUT IS IN FILE "PROPA.OUT"
C UNITS ARE RADIANS AND FT EXCEPT FOR SELECTED INPUT AND OUTPUT
C (FOR USER FRIENDLINESS)
IMPLICIT REAL*8 (A-H,O-Z)
REAL*8 LAMBDA,N
DIMENSION CL(21),CD(21),ALPHA(21),RR(21),X(21),F(21),BIGF(21),
&CHORD(21),PHI(21),BETA(21),DTC(21),DPC(21),A(21),AP(21),
&GAM(21),W(21),SIGMA(21)
COMMON/AIRDAT/ALPHA1,ALPHA2,ALPHA3,CL1,CL2,CD1,CD2
DATA PI/3.141592654/
OPEN(UNIT=10,FILE='PROPA.INP',STATUS='OLD')
REWIND 10
READ(10,10)
10 FORMAT(//////)

```

```

VTEMP=V
READ(10,*) NB,RHO,RPM,RADIUS,V
V=VTEMP
READ(10,20)
20  FORMAT(//////)
C
DO 30 I=1,21
READ(10,*) RR(I),CHORD(I),BETA(I)
CHORD(I)=CHORD(I)/12.
BETA(I)=PI/180.*BETA(I)
30  CONTINUE
C
READ(10,40)
40  FORMAT(//)
READ(10,*) A1,A2,A3,CL1,CL2,CD1,C2
ALPHA1=A1*PI/180.
ALPHA2=A2*PI/180.
ALPHA3=A3*PI/180.
CD2=(180./PI)**2*C2
LAMBDA=V/RPM*60./2./PI/RADIUS
ADVANCE=LAMBDA*PI
C
C  INDUCED FLOW CALCULATIONS
C
DO 100 I=2,21
X(I)=RR(I)/LAMBDA
F(I)=NB/2./LAMBDA*DSQRT(LAMBDA**2+1.)*(1.-RR(I))
100  BIGF(I)=2./PI*DACOS(DEXP(-F(I)))
C
C  FIND CORRECT PHI AND ALPHA BY ITERATING
C
DO 1000 I=2,20
ALPHAT=5.*PI/180.
200  CALL CLCD(ALPHAT,CLT,CDT)
PHIT=BETA(I)-ALPHAT
SIGMA(I)=NB*CHORD(I)/2./PI/RR(I)/RADIUS
RHS1=SIGMA(I)/BIGF(I)/4.*(CLT*DCOS(PHIT)-CDT*DSIN(PHIT))/
&DSIN(PHIT)**2
RHS2=SIGMA(I)/BIGF(I)/4.*(CLT*DSIN(PHIT)+CDT*DCOS(PHIT))/
&DSIN(PHIT)*DCOS(PHIT)
AT=RHS1/(1.-RHS1)
APT=RHS2/(1.+RHS2)
PHINEW=DATAN(LAMBDA/RR(I)*(1.+AT)/(1.-APT))
DIFF=DABS(PHINEW-PHIT)
IF(DIFF.LE.0.000017) GOTO 900
ALPHAT=ALPHAT+(PHIT-PHINEW)/2.
GOTO 200
900  PHI(I)=PHINEW
CL(I)=CLT
CD(I)=CDT
ALPHA(I)=BETA(I)-PHI(I)
A(I)=AT
AP(I)=APT
1000 CONTINUE
C
C  COMPUTE THRUST AND POWER
C
DTC(1)=0.
DPC(1)=0.
DTC(21)=0.
DPC(21)=0.
C
DO 1100 I=2,20
DTC(I)=PI**3/4.*((1-AP(I))/DCOS(PHI(I)))**2*RR(I)**3*
&SIGMA(I)*(CL(I)*DCOS(PHI(I))-CD(I)*DSIN(PHI(I)))
DPC(I)=PI**4/4.*((1-AP(I))/DCOS(PHI(I)))**2*RR(I)**4*

```

```

      &SIGMA(I) * (CL(I) * DSIN(PHI(I)) + CD(I) * DCOS(PHI(I)))
1100 CONTINUE
C
      CALL SIMPSN(DTC,TC)
      CALL SIMPSN(DPC,PC)
      N=RPM/60.
      THRUST=TC*RHO*N**2*(2.*RADIUS)**4
      POWER=PC*RHO*N**3*(2.*RADIUS)**5/550.
      ETA=THRUST*V/550./POWER
C
C COMPUTE CIRCULATION DISTRIBUTION
C
      GAM(1)=0.
      GAM(21)=0.
      DO 1200 I=2,20
      W(I)=DSQRT((RPM/60.*2.*PI*RR(I)*(1-AP(I)))**2+
&(V*(1+A(I)))**2)
1200 GAM(I)=W(I)*CL(I)*CHORD(I)/2.
C
C PRINT OUT INPUT
C
      IF (LOOPCOUNT.GT.1) GO TO 2905
      WRITE(IPRT,2000)
2000 FORMAT(2X,'PROPELLER ANALYSIS PROGRAM'/2X,'INPUT PARAMETERS'//
&2X,'BLADE',6X,'AIR',5X,'PROP',4X,'PROP',4X,'DESIGN'
&/2X,'NUMBER',3X,'DENSITY',3X,'RPM',4X,
&'RADIUS',3X,'VELOCITY',
&/10X,'SLUG/FT^3',11X,
&'FT',6X,'FT/SEC')
      WRITE(IPRT,2100)NB,RHO,RPM,RADIUS,V
2100 FORMAT(3X,I2,5X,F8.6,2X,F6.1,3X,F5.2,3X,F7.3)
      WRITE(IPRT,2200)
2200 FORMAT(/10X,'CHORD',',5X,'BLADE'/3X,'r/R',4X,'INCHES',
&5X,'ANGLE')
      DO 2250 I=1,21
      CHORD(I)=12.*CHORD(I)
      BETA(I)=BETA(I)*180./PI
2250 WRITE(IPRT,2300)RR(I),CHORD(I),BETA(I)
2300 FORMAT(2X,F5.3,3X,F6.3,5X,F5.2)
      WRITE(IPRT,2350)
2350 FORMAT(/3X,'ALPHA1  ALPHA2  ALPHA3      CL1      CL2
&      CD1      CD2')
      WRITE(IPRT,2400)A1,A2,A3,CL1,CL2,CD1,C2
2400 FORMAT(2X,F8.4,1X,F8.5,1X,F8.5,1X,F8.5,1X,F8.5,1X,F8.5,1X,F8.5,1X,F8.5)
C
C PRINT OUT RESULTS
C
      WRITE(IPRT,2500)
2500 FORMAT(/2X,'COMPUTED RESULTS'/4X,'r/R      CL      CD      ALPHA
&      PHI      GAMMA      dCT/dr      dCP/dr')
      CL(1)=0.
      CD(1)=0.
      ALPHA(1)=0.
      PHI(1)=PI/2.
      CL(21)=0.
      CD(21)=0.
      ALPHA(21)=0.
      PHI(21)=BETA(21)*PI/180.
C
      DO 2600 I=1,21
      ALPHA(I)=ALPHA(I)*180./PI
      PHI(I)=PHI(I)*180./PI
      WRITE(IPRT,2700)RR(I),CL(I),CD(I),ALPHA(I),PHI(I),GAM(I),
&DTC(I),DPC(I)
2600 CONTINUE
C

```

```

2700  FORMAT(2X,F7.4,2X,F7.4,2X,F7.4,2X,F7.4,2X,F7.4,2X,F7.4,
&2X,F7.4,2X,F7.4,2X,F7.4)
      WRITE(IPRT,2800)
2800  FORMAT(/2X,'THRUST, LB      POWER, HP      EFFICIENCY
& J      CT      CP')
      WRITE(IPRT,2900)THRUST,POWER,ETA,ADVANCE,TC,PC
2900  FORMAT(1X,F8.2,5X,F8.2,7X,F10.4,5X,F6.2,5X,F5.3,5X,
&F5.3)
2905  CLOSE (10)
      RETURN
      END

```

```

C
C*****
      SUBROUTINE CLCD(ALPHA,CL,CD)
C  FINDS CL AND CD THAT CORRESPOND TO AN INPUT ANGLE OF ATTACK
C  USING SIMPLE EQUATIONS
C  WRITTEN FOR PROGRAM PROPA
C  EQUATIONS FROM LARRABEE PAPERS
      IMPLICIT REAL*8 (A-H,O-Z)
      COMMON/AIRDAT/ALPHA1,ALPHA2,ALPHA3,CL1,CL2,CD1,CD2
      IF(ALPHA.LE.ALPHA1) GOTO 1000
      IF(ALPHA.GE.ALPHA2) GOTO 2000
      CL=CL1+((CL2-CL1)/(ALPHA2-ALPHA1))*(ALPHA-ALPHA1)
      CD=CD1+CD2*(ALPHA-ALPHA3)**2
      GOTO 3000
1000  CL=DCOS(ALPHA)*CL1/DCOS(ALPHA1)
      CD=DABS(DSIN(ALPHA))
      GOTO 3000
2000  CL=DCOS(ALPHA)*CL2/DCOS(ALPHA2)
      CD=DABS(DSIN(ALPHA))
3000  CONTINUE
      RETURN
      END

```

```

C
C*****
      SUBROUTINE SIMPSN(DATA,RESULT)
C  SIMPSON'S RULE INTEGRATION OF INPUT DATA
C  WRITTEN FOR PROGRAM PROPA
C  ONLY WORKS WITH DATA VECTOR 21 ITEMS IN LENGTH WITH AN
C  INTERVAL OF 0.05
      IMPLICIT REAL*8 (A-H,O-Z)
      DIMENSION DATA(21)
      RESULT=0.05/3.*(DATA(1)+DATA(21)+
&4.*(DATA(2)+DATA(4)+DATA(6)+DATA(8)+DATA(10)+DATA(12)+
& DATA(14)+DATA(16)+DATA(18)+DATA(20))+
&2.*(DATA(3)+DATA(5)+DATA(7)+DATA(9)+DATA(11)+DATA(13)+
& DATA(15)+DATA(17)+DATA(19)))
      RETURN
      END

```

PROPA.INP

PROPELLER ANALYSIS PROGRAM
INPUT PARAMETERS

BLADE NUMBER	AIR DENSITY SLUG/FT ³	PROP RPM	PROP RADIUS FT	AIR VELOCITY FT/SEC
4	0.002378	8200.0	0.97	205.0

INPUT BLADE GEOMETRY

r/R	CHORD, INCHES	BLADE ANGLE
0.000	0.000	83.00
0.050	1.200	78.00
0.100	3.000	69.00
0.150	3.600	61.00
0.200	3.660	53.00
0.250	3.670	46.70
0.300	3.670	41.00
0.350	3.670	37.50
0.400	3.670	33.50
0.450	3.670	31.50
0.500	3.670	29.50
0.550	3.670	27.70
0.600	3.650	25.70
0.650	3.620	24.20
0.700	3.600	22.70
0.750	3.530	21.30
0.800	3.480	19.70
0.850	3.350	18.70
0.900	3.160	18.00
0.950	2.790	17.00
1.000	0.000	16.90

INPUT BLADE AIRFOIL AERODYNAMIC CHARACTERISTICS

ALPHA1	ALPHA2	ALPHA3	CL1	CL2	CD1	CD2
-8.0	10.0	-1.5	-0.6	1.0	.005	.001175

PROPA.OUT

PROPELLER ANALYSIS PROGRAM
INPUT PARAMETERS

BLADE NUMBER	AIR DENSITY SLUG/FT ³	PROP RPM	PROP RADIUS FT	DESIGN VELOCITY FT/SEC
4	0.002378	8200.0	0.97	205.000

r/R	CHORD, INCHES	BLADE ANGLE
0.000	0.000	83.00
0.050	1.200	78.00
0.100	3.000	69.00
0.150	3.600	61.00
0.200	3.660	53.00
0.250	3.670	46.70
0.300	3.670	41.00
0.350	3.670	37.50
0.400	3.670	33.50
0.450	3.670	31.50
0.500	3.670	29.50
0.550	3.670	27.70
0.600	3.650	25.70
0.650	3.620	24.20
0.700	3.600	22.70
0.750	3.530	21.30
0.800	3.480	19.70
0.850	3.350	18.70
0.900	3.160	18.00
0.950	2.790	17.00
1.000	0.000	16.90

ALPHA1	ALPHA2	ALPHA3	CL1	CL2	CD1	CD2
-8.0000	10.00000	-1.50000	-0.60000	1.00000	0.00500	0.00117

COMPUTED RESULTS

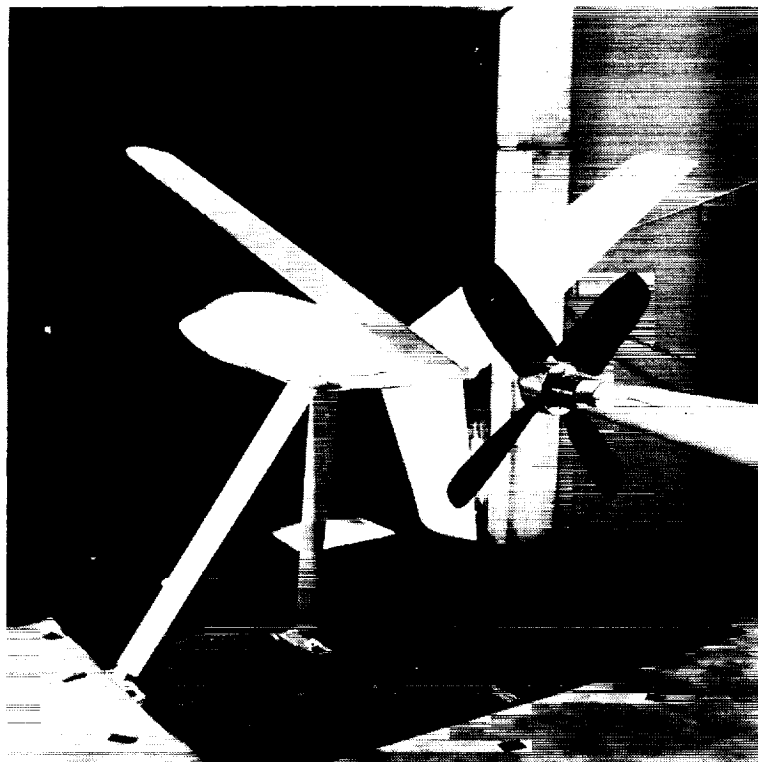
r/R	CL	CD	ALPHA	PHI	GAMMA	dCT/dr	dCP/dr
0.0000	0.0000	0.0000	0.0000	90.0000	0.0000	0.0000	0.0000
0.0500	0.0594	0.0060	-0.5825	78.5825	0.6230	0.0002	0.0003
0.1000	0.1383	0.0088	0.3056	68.6944	3.8979	0.0039	0.0038
0.1500	0.1776	0.0109	0.7473	60.2527	6.5627	0.0103	0.0099
0.2000	0.1526	0.0095	0.4670	52.5330	6.2941	0.0136	0.0127
0.2500	0.1499	0.0094	0.4357	46.2643	6.8537	0.0189	0.0176
0.3000	0.1249	0.0082	0.1548	40.8452	6.3147	0.0211	0.0196
0.3500	0.1577	0.0098	0.5234	36.9766	8.8031	0.0345	0.0324
0.4000	0.1359	0.0087	0.2786	33.2214	8.3281	0.0376	0.0354
0.4500	0.1779	0.0110	0.7516	30.7484	11.9114	0.0605	0.0583
0.5000	0.1998	0.0123	0.9981	28.5019	14.5389	0.0822	0.0808
0.5500	0.2143	0.0133	1.1606	26.5394	16.8574	0.1050	0.1051
0.6000	0.2061	0.0128	1.0690	24.6310	17.3594	0.1184	0.1195
0.6500	0.2099	0.0130	1.1108	23.0892	18.7922	0.1391	0.1425
0.7000	0.2034	0.0126	1.0390	21.6610	19.3442	0.1546	0.1600
0.7500	0.1944	0.0120	0.9373	20.3627	19.2838	0.1656	0.1728
0.8000	0.1679	0.0104	0.6382	19.0618	17.4139	0.1600	0.1674
0.8500	0.1634	0.0101	0.5878	18.1122	17.2537	0.1687	0.1789
0.9000	0.1650	0.0102	0.6058	17.3942	17.3267	0.1794	0.1941
0.9500	0.1438	0.0091	0.3671	16.6329	14.0246	0.1534	0.1689
1.0000	0.0000	0.0000	0.0000	16.9000	0.0000	0.0000	0.0000

THRUST, LB	POWER, HP	EFFICIENCY	J	CT	CP
52.0745	25.9487	0.7480	0.77	0.083	0.086

FORTRAN STOP

Table 1. Propeller operating conditions and estimated performance

Windspeed, m/sec	N, rpm	Blade angle β , deg	Advance ratio J	Thrust coeff. C_t	Power coeff. C_p
0	6000	6	0	—	—
0	8200	6	0	—	—
46	8200	16	0.57	0.05	0.04
62	6000	30	1.06	0.16	0.23
62	8200	21	0.77	0.08	0.09



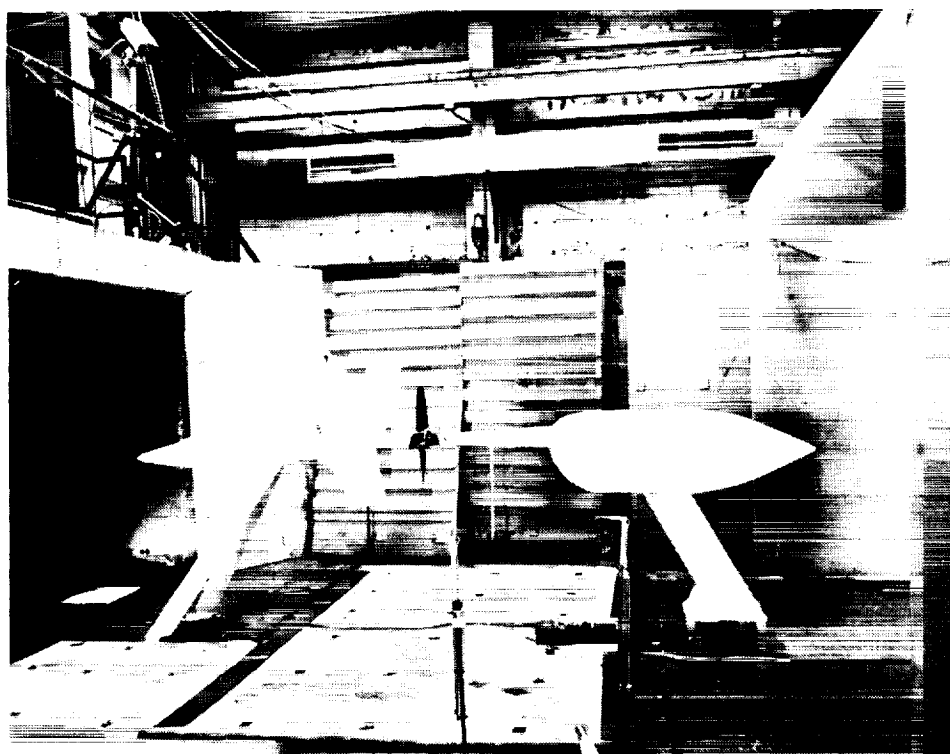
(a)



(b)

Figure 1. Model propeller, empennages, and fuselage in the Ames Research Center 7- by 10-Foot Wind Tunnel test section. (a) Y-tail, (b) Y-tail empennage seen from below.

ORIGINAL PAGE
BLACK AND WHITE PHOTOGRAPH



(c)



(d)

Figure 1. Concluded. (c) Open test section and Y-tail with sound-absorbing panels used to minimize acoustic reflections, (d) I-tail.

ORIGINAL PAGE
BLACK AND WHITE PHOTOGRAPH

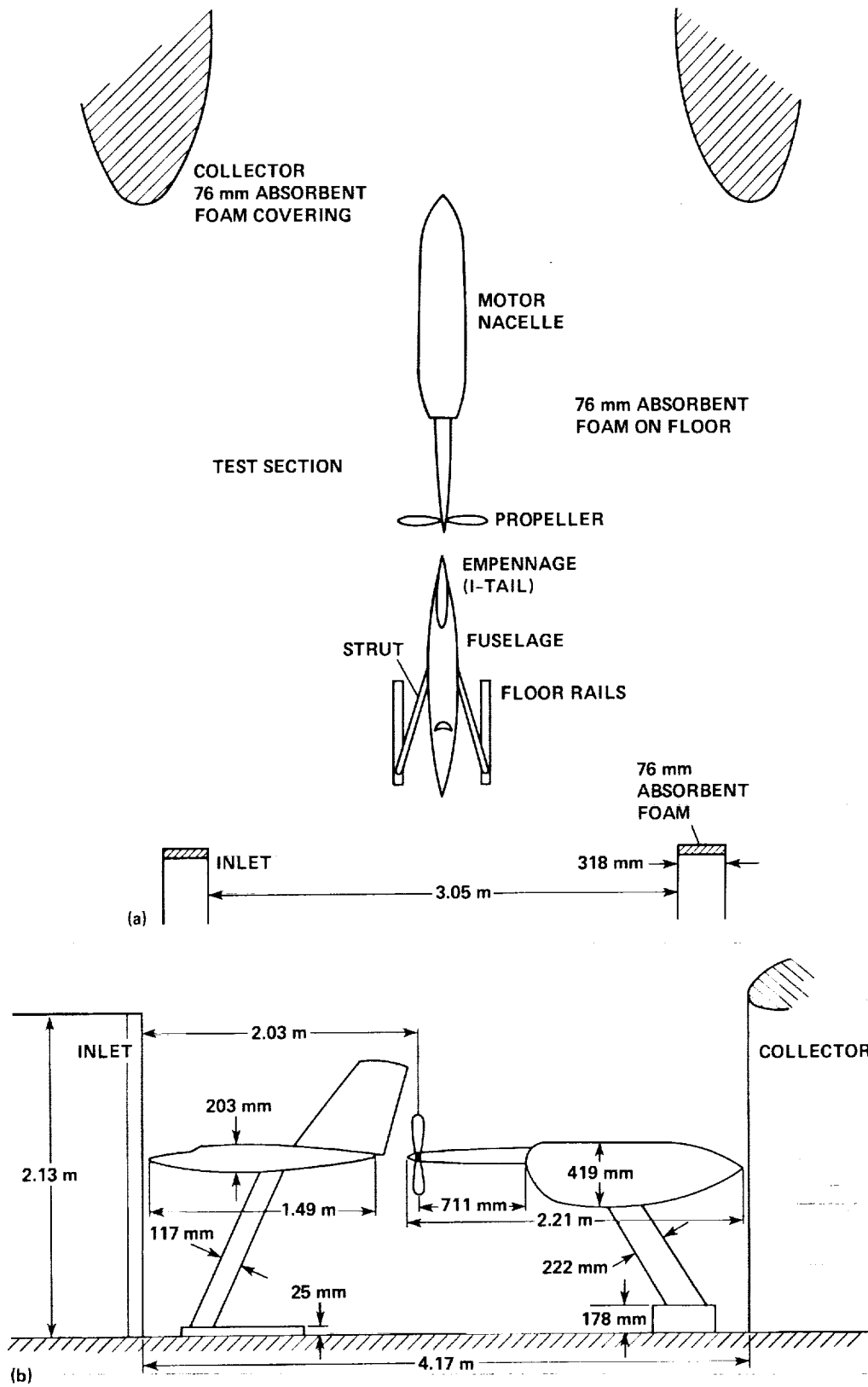


Figure 2. Schematic of model in test section relative to inlet and collector. (a) Plan view, (b) elevation view.

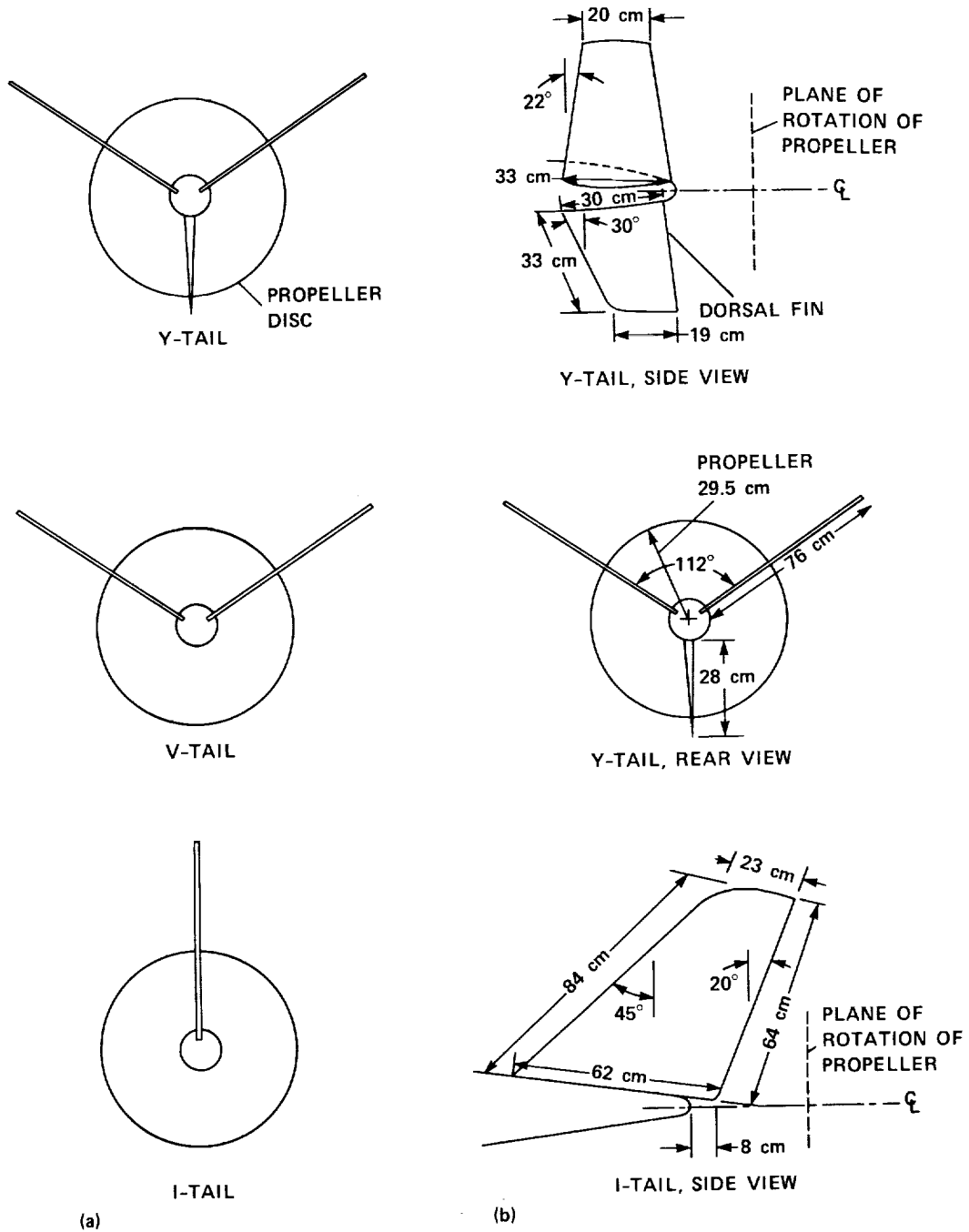


Figure 3. Geometry of empennages. (a) Looking downstream, (b) dimensions.

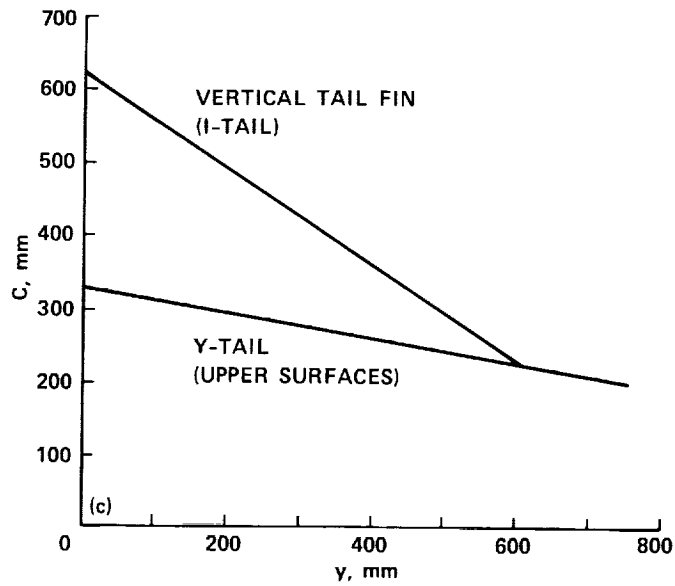


Figure 3. Concluded. (c) Chord distribution versus span station.

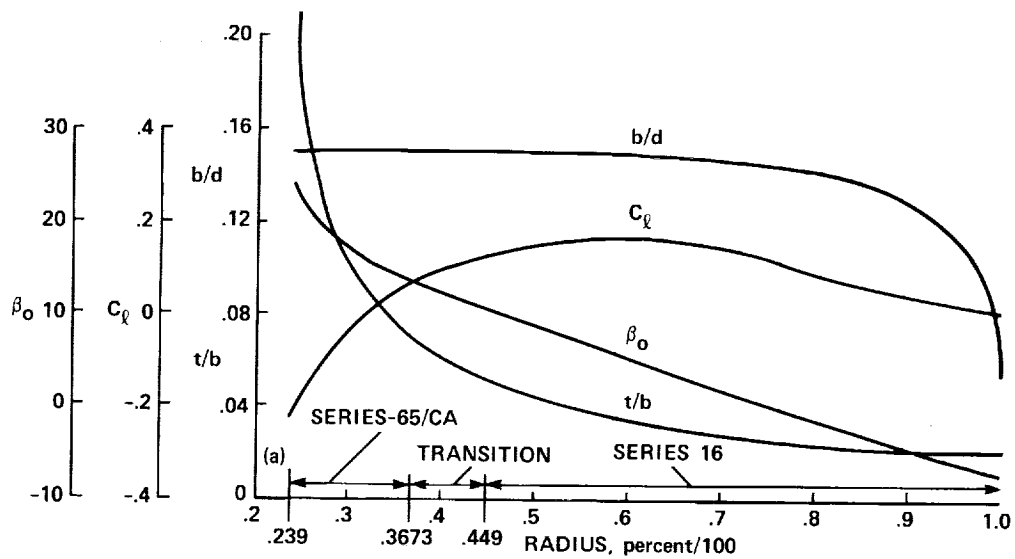
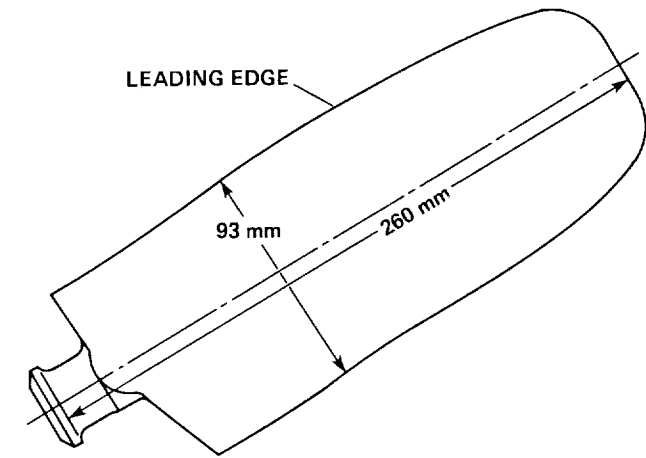
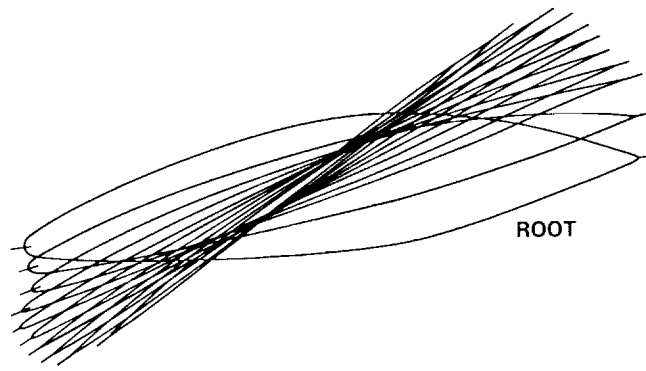


Figure 4. SR-2 propeller geometry. (a) Spanwise distribution of chord (b), twist (β_0) thickness (t), and design lift coefficient (C_l). The reference diameter (d) for this figure is 622 mm.

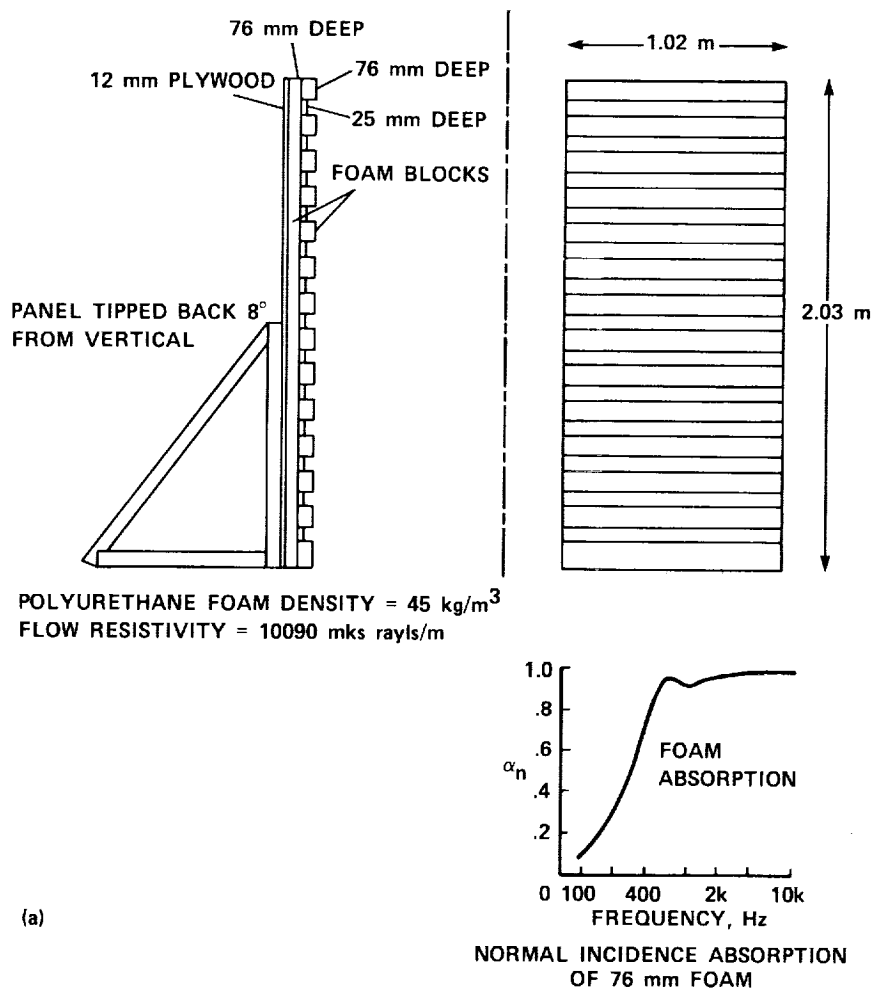


(b)

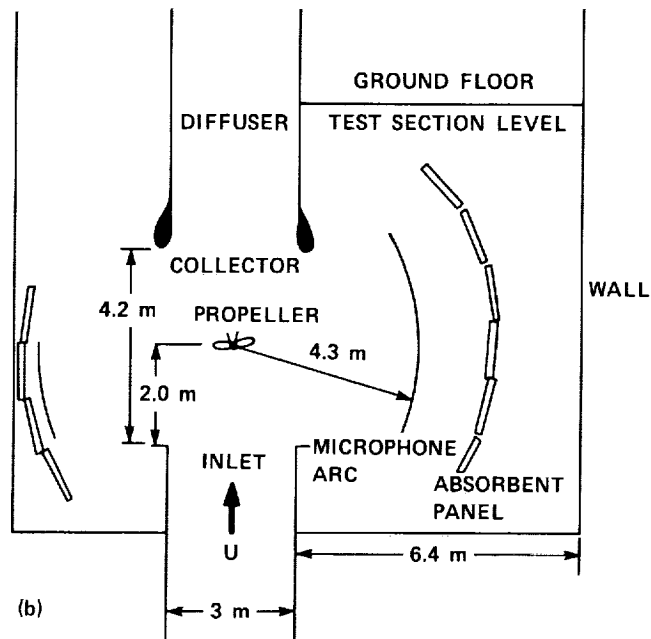


(c)

Figure 4. Concluded. (b) Blade planform, (c) blade airfoil sections at 12 radial stations from the root to tip.

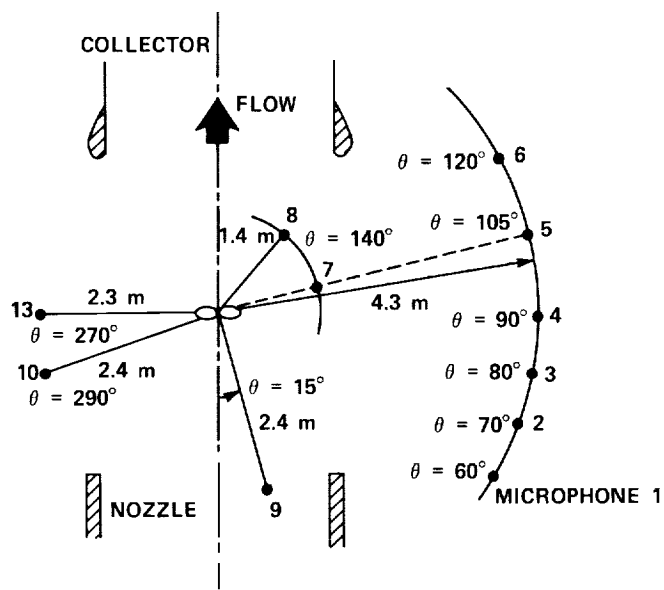


(a)

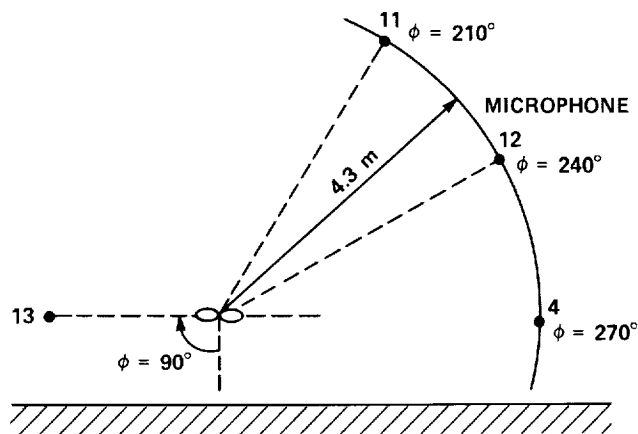


(b)

Figure 5. Sound-absorbent panels used to prevent acoustic reflections from the walls. (a) Panel geometry and lining properties, (b) general arrangement of panels.



(a)



(b)

Figure 6. Microphone locations relative to propeller hub. (a) Plan view, (b) looking downstream at plane containing propeller.

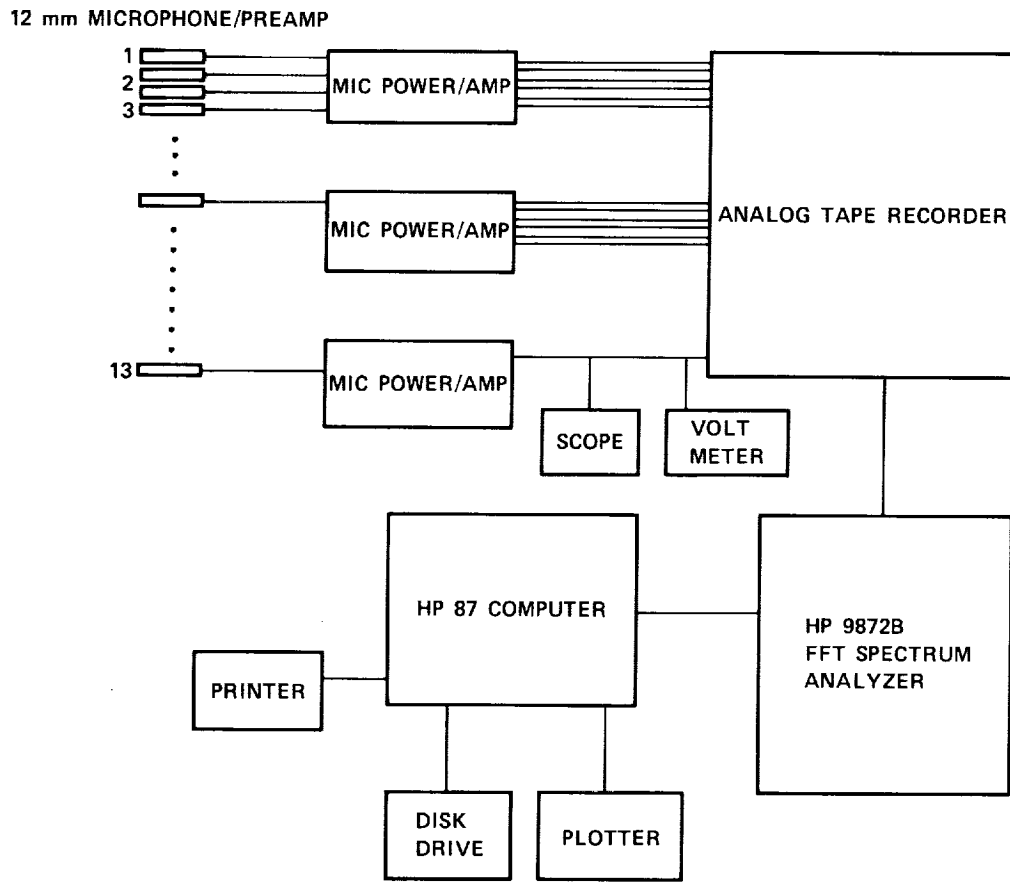
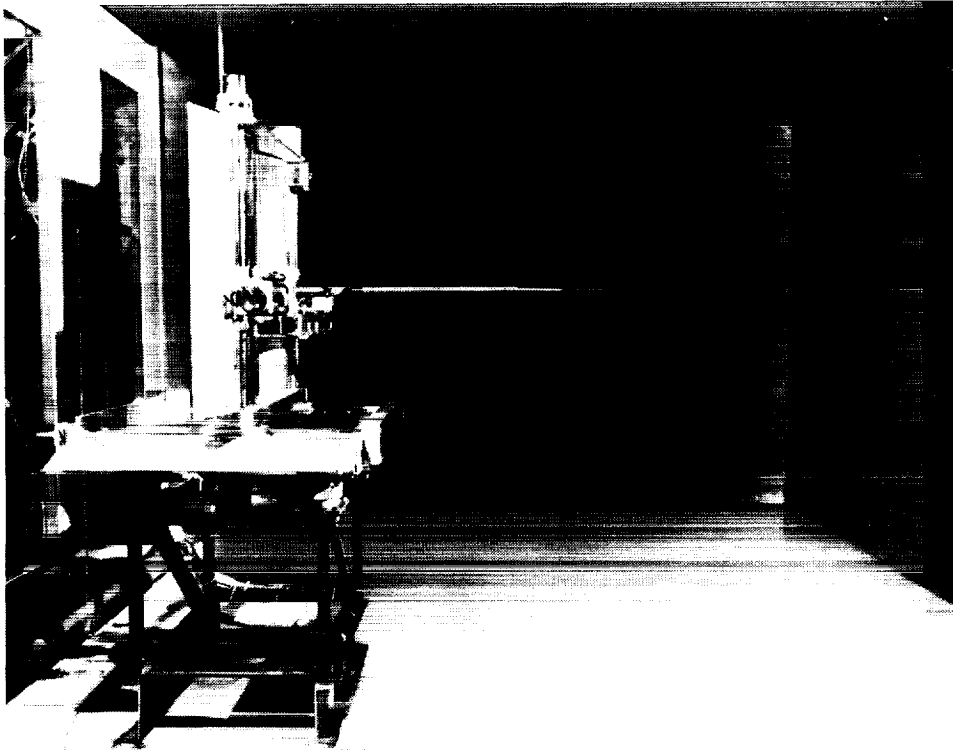


Figure 7. Acoustic data-acquisition and reduction system.



(a)

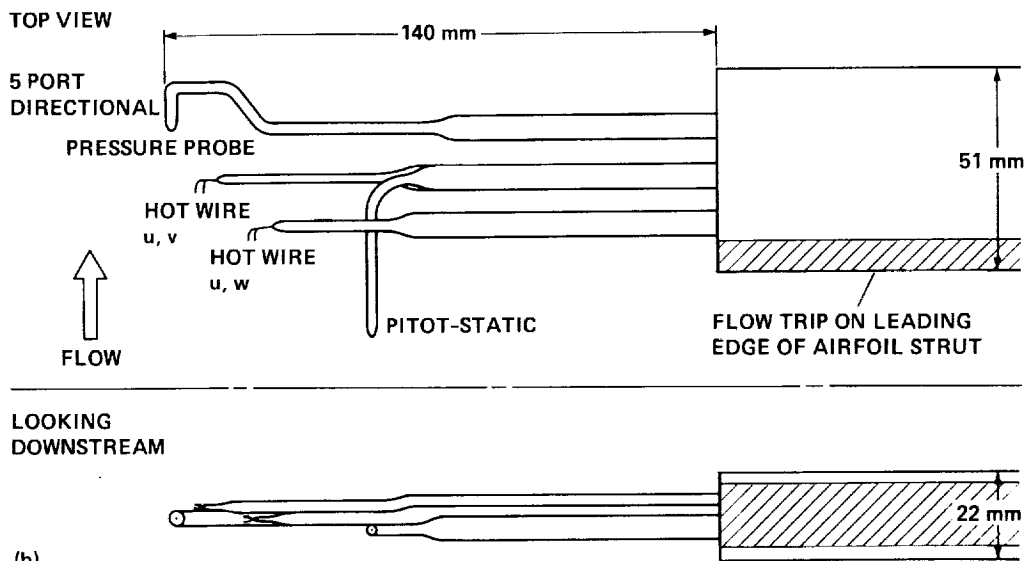


Figure 8. Flow survey apparatus. (a) Survey apparatus in test section prior to wall removal, (b) probe details.

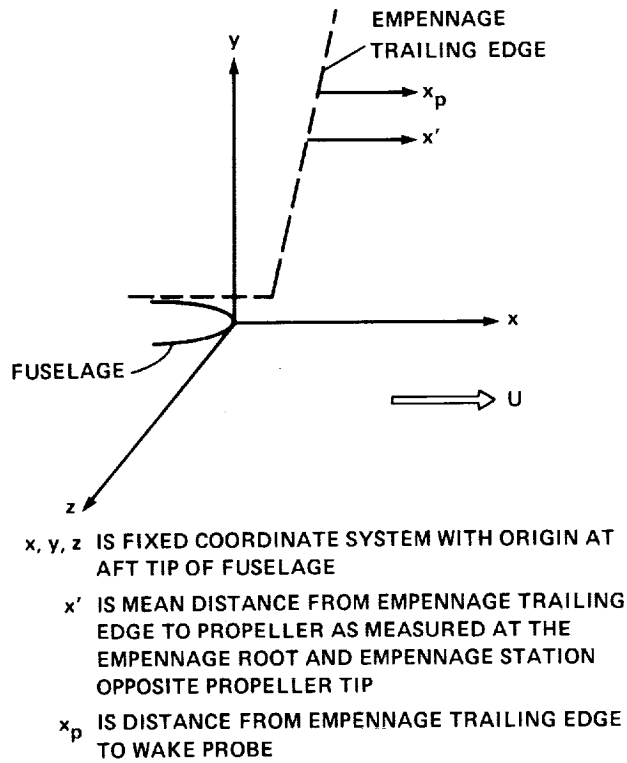


Figure 9. Coordinate systems relative to fuselage tip (x, y, z) and relative to empennage trailing edge (x', x_p).

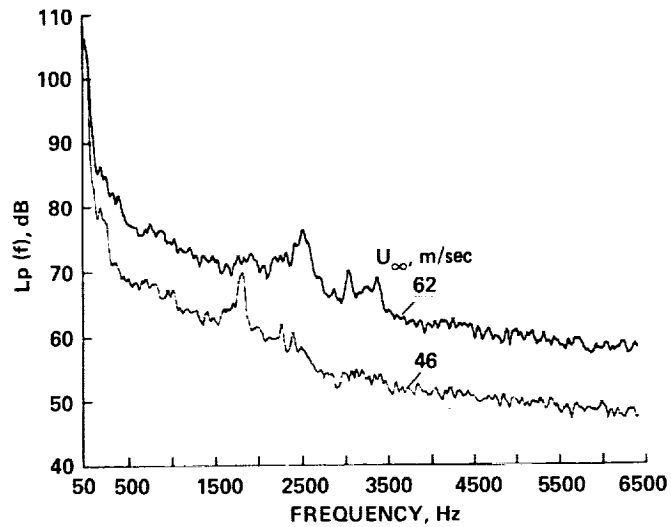


Figure 10. Background noise out of flow at two airspeeds; $\theta = 76$ and 78° (microphone 2) (propeller not operating—fuselage without empennage installed).

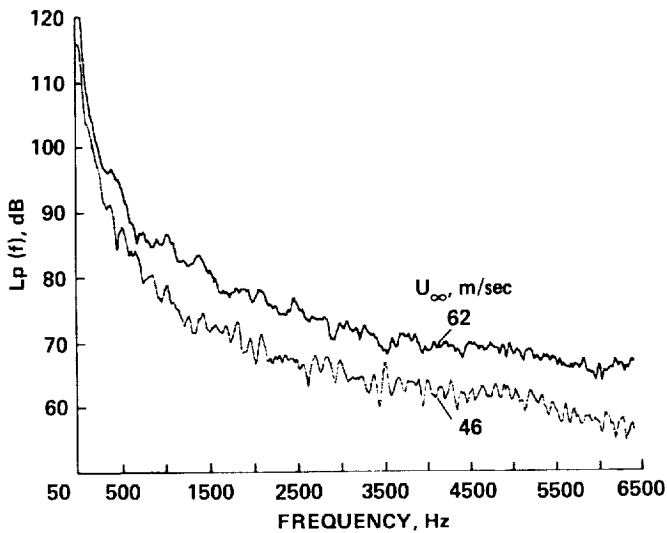


Figure 11. Background noise in flow at two airspeeds; $\theta = 105^\circ$ (microphone 7) (propeller not operating—fuselage without empennage installed). The data have been extrapolated to 4.3 m.

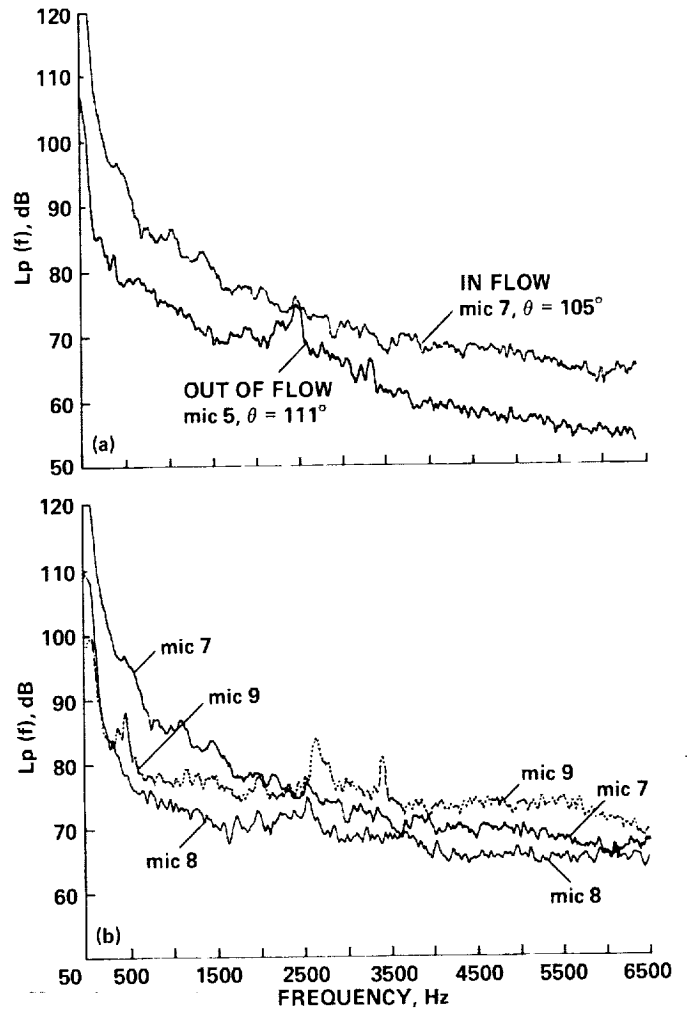


Figure 12. Comparison of background noise measured in and out of flow (propeller not operating—fuselage without empennage installed). In-flow data have been extrapolated to 4.3 m. Data out of flow measured at 4.3 m have been corrected to estimated angle induced by shear-layer diffraction. $U_\infty = 62$ m/sec. (a) $\theta = 111$ and 105° (microphones 5 and 7), (b) in flow only; $\theta = 105, 140,$ and 15° (microphones 7, 8, and 9).

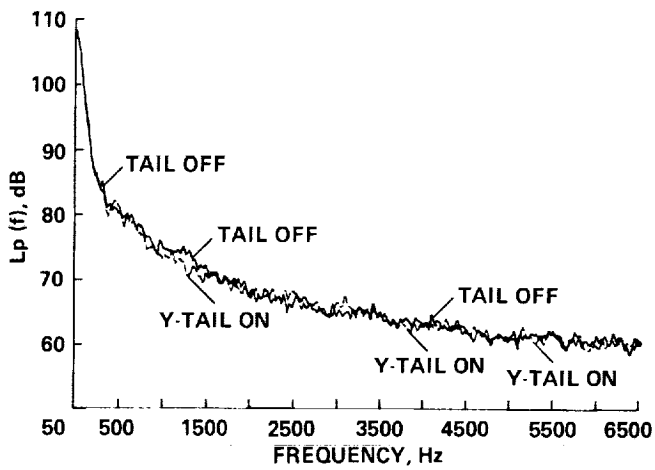


Figure 13. Influence of Y-tail on background noise; propeller not operating. $\theta = 78^\circ$ (microphone 2), $U_\infty = 62$ m/sec.

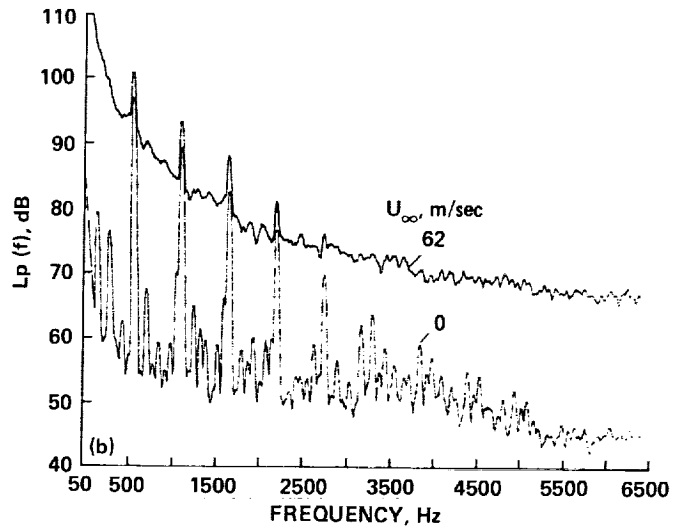
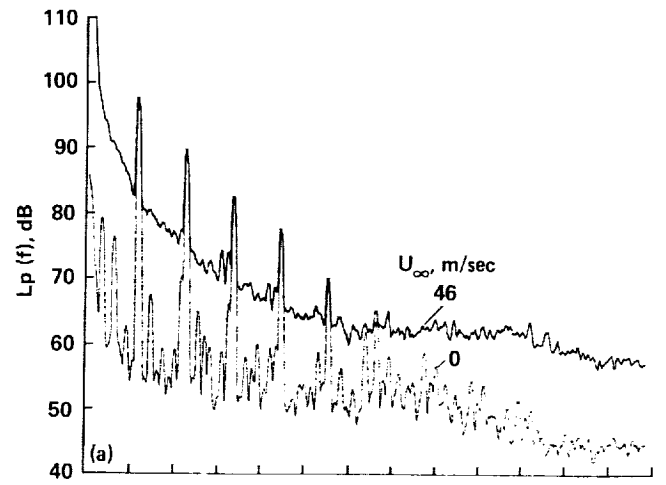


Figure 14. Propeller-alone noise with and without airflow (fuselage removed). $\theta = 105^\circ$ (microphone 7), $N = 8200$ rpm. (a) $U_\infty = 0$ and 46 m/sec, (b) $U_\infty = 62$ m/sec.

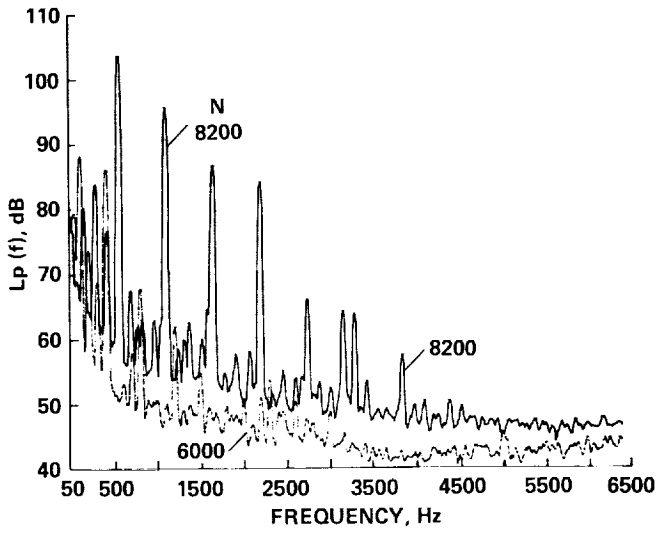


Figure 15. Propeller-alone noise spectra at two rotational speeds and zero wind speed. $\theta = 90^\circ$ (microphone 12).

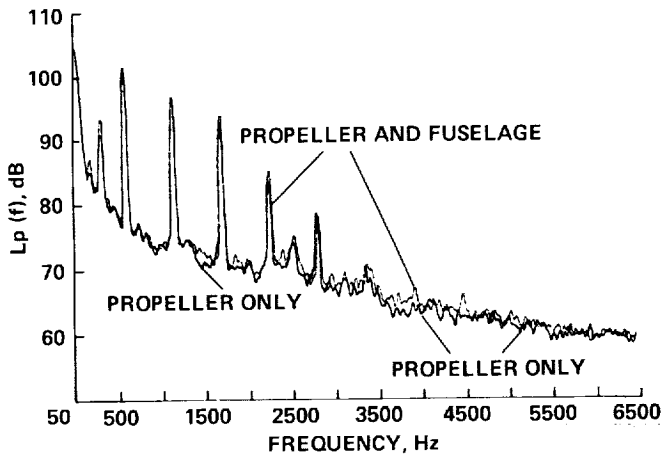


Figure 16. Effect of fuselage on propeller noise spectrum. $\theta = 96^\circ$ (microphone 12), $U_\infty = 62$ m/sec, $N = 8200$ rpm.

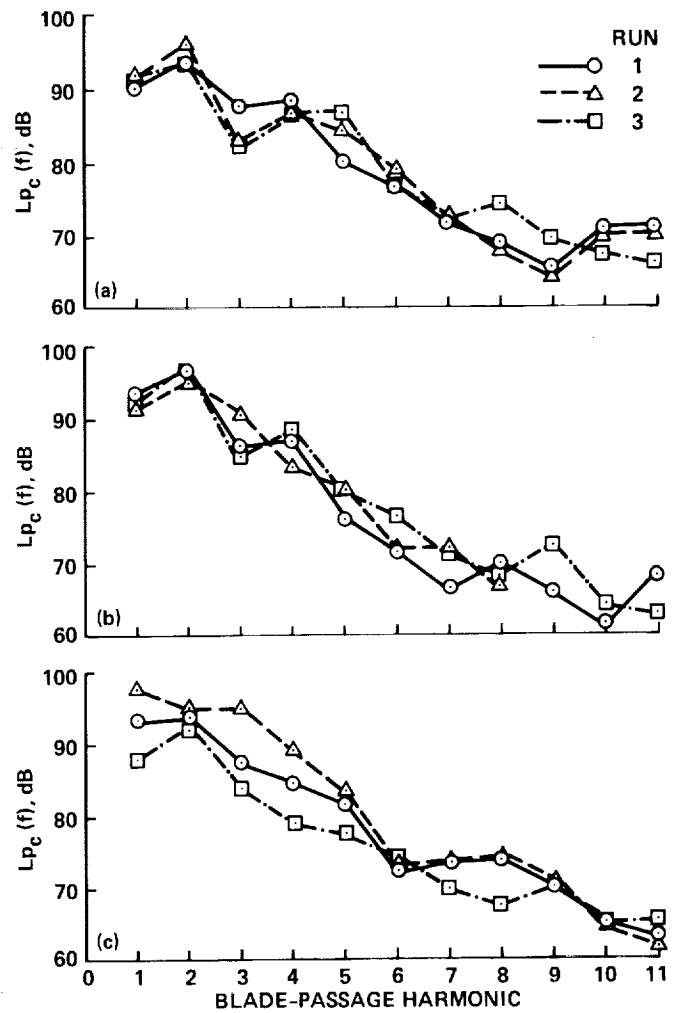


Figure 17. Comparison of blade-passage harmonic noise levels measured at 10 microphones for repeat runs (Y-tail). $U_\infty = 62$ m/sec, $N = 8200$ rpm, $x'/c' = 0.83$. (a) Microphone 1 ($\theta = 89^\circ$), (b) microphone 2 ($\theta = 78^\circ$), (c) microphone 3 ($\theta = 87^\circ$).

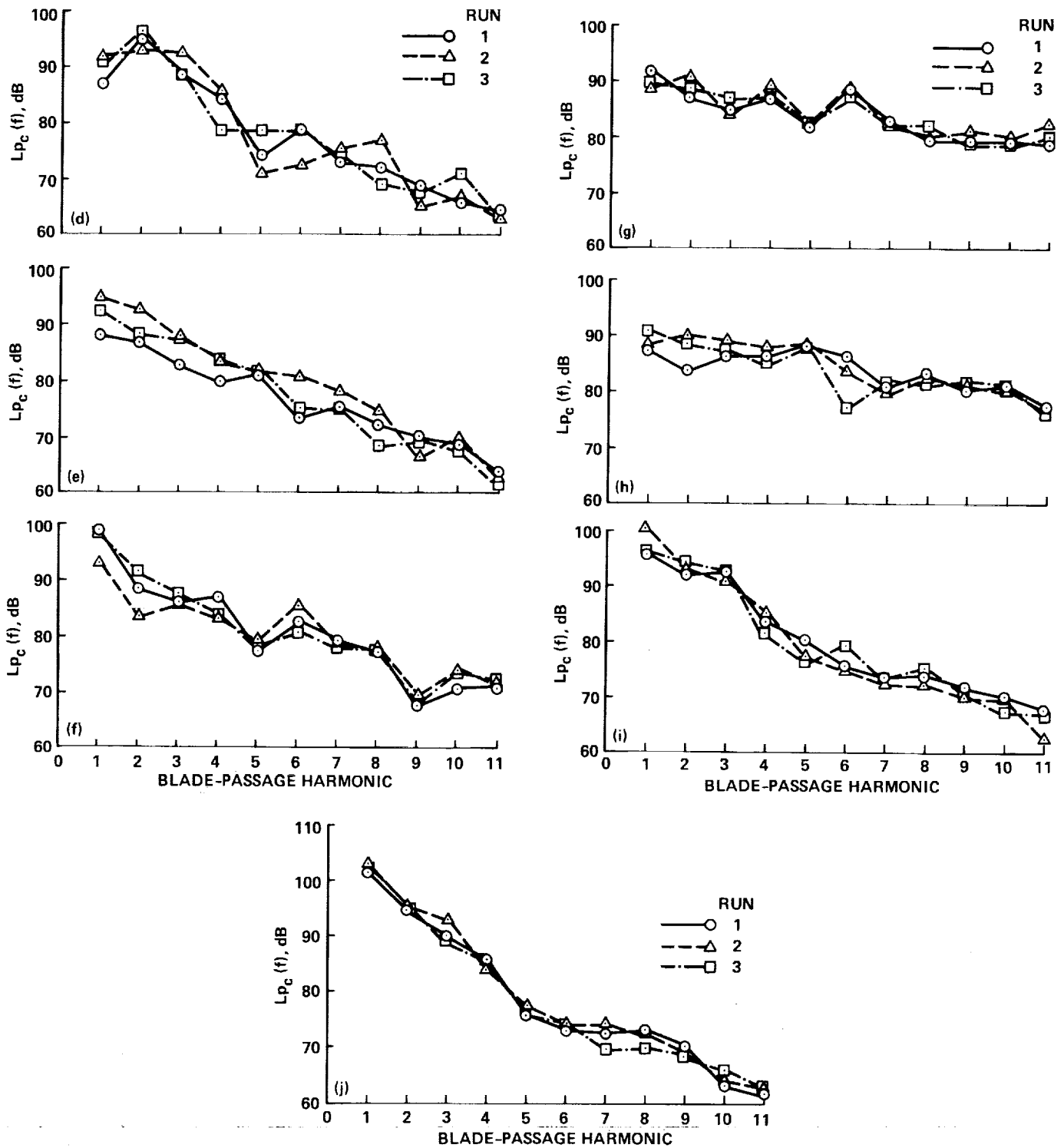


Figure 17. Concluded. (d) Microphone 4 ($\theta = 97^\circ$), (e) microphone 5 ($\theta = 111^\circ$), (f) microphone 6 ($\theta = 126^\circ$), (g) microphone 8 ($\theta = 140^\circ$), (h) microphone 9 ($\theta = 15^\circ$), (i) microphone 11 ($\theta = 98^\circ$), (j) microphone 12 ($\theta = 96^\circ$).

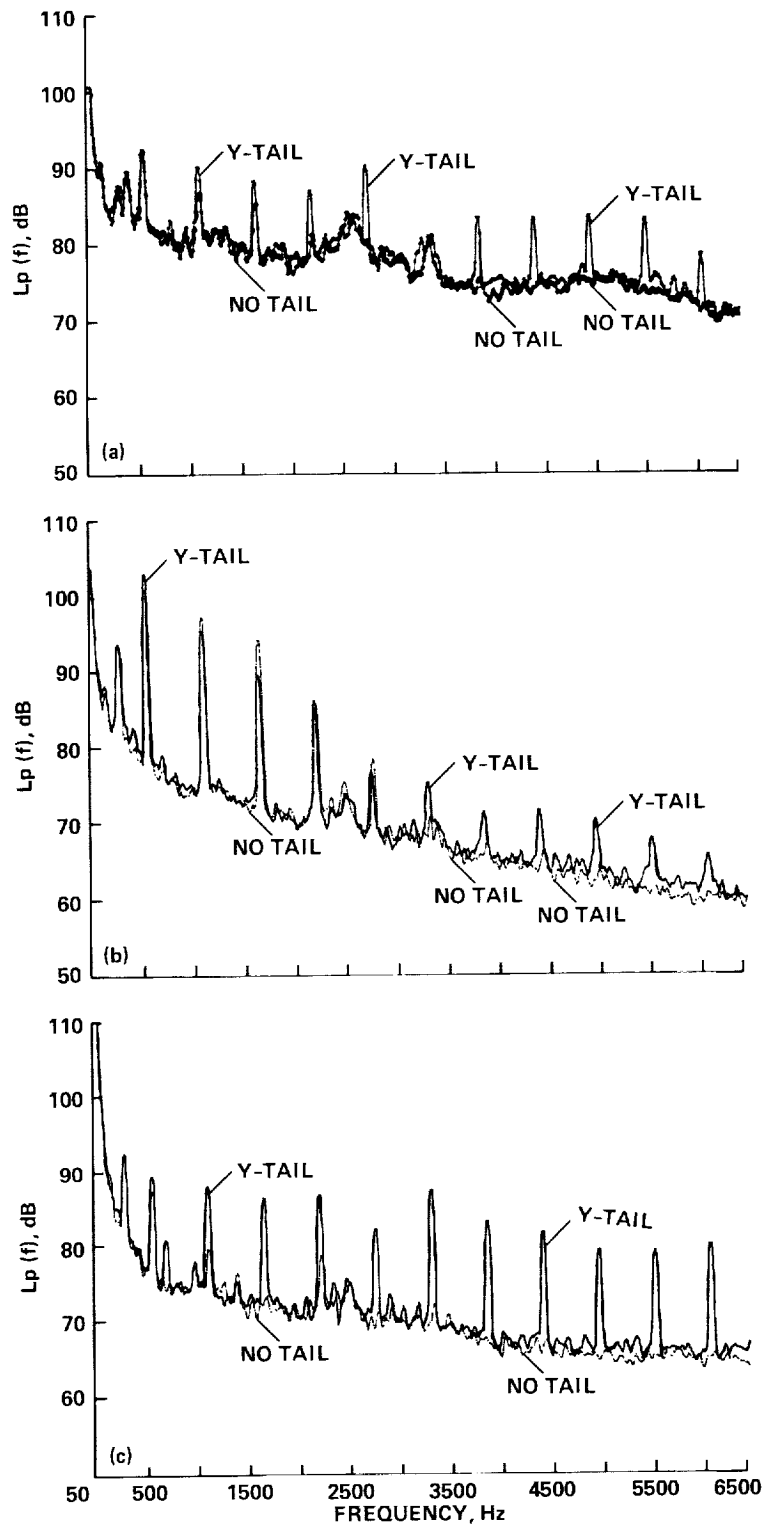


Figure 18. Effect of Y-tail on acoustic spectrum, $U_\infty = 62$ m/sec, $N = 8200$ rpm, $x'/c' = 0.80$.
 (a) $\theta = 15^\circ$ (microphone 9), (b) $\theta = 96^\circ$ (microphone 12), (c) $\theta = 140^\circ$ (microphone 8).

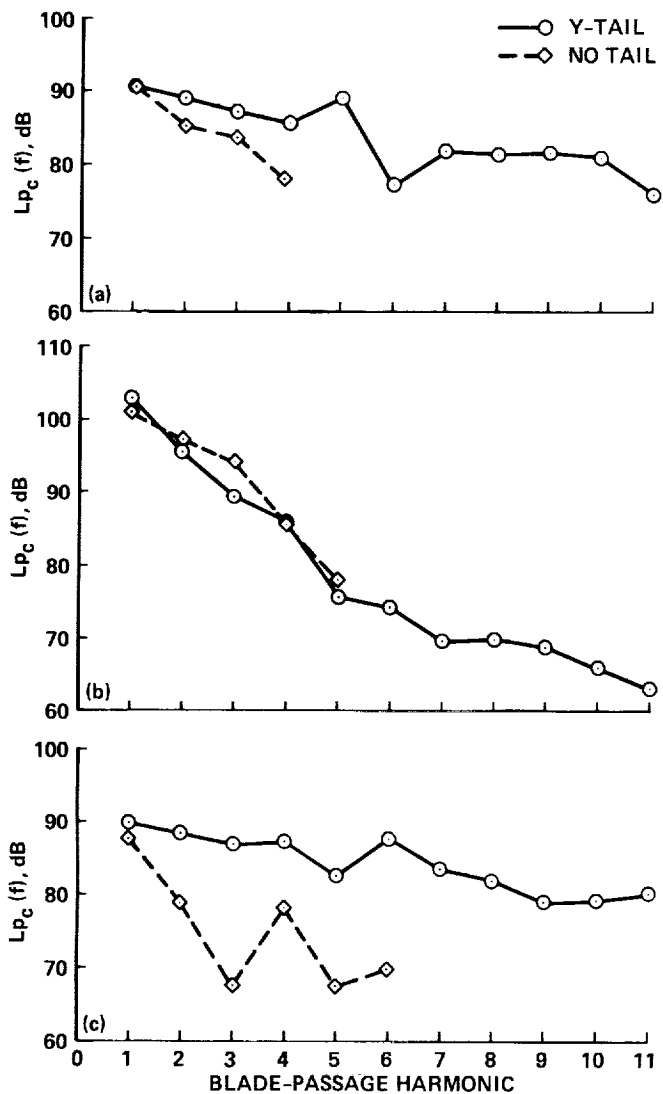


Figure 19. Effect of Y-tail on harmonics of blade-passage noise, $U_\infty = 62$ m/sec, $N = 8200$ rpm, $x'/c' = 0.80$.
 (a) $\theta = 15^\circ$ (microphone 9), (b) $\theta = 96^\circ$ (microphone 12),
 (c) $\theta = 140^\circ$ (microphone 8).

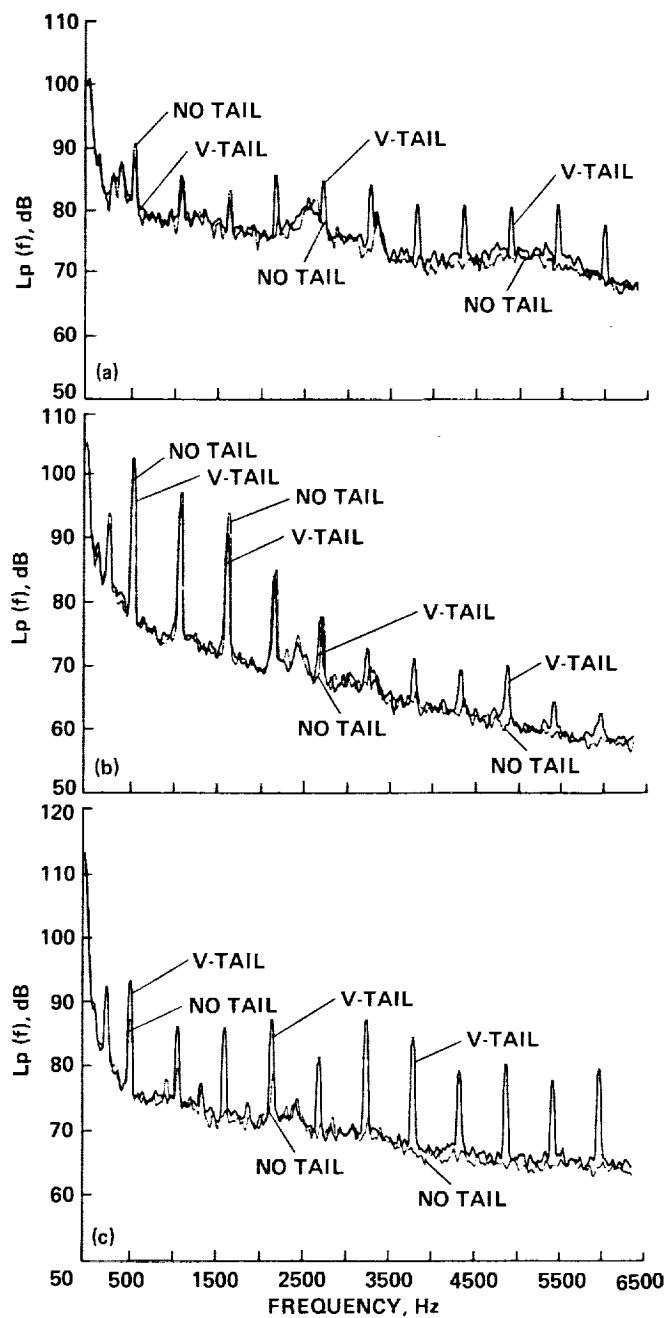


Figure 20. Effect of V-tail on acoustic spectrum.
 $U_\infty = 62$ m/sec, $N = 8200$ rpm, $x'/c' = 0.83$. (a) $\theta = 15^\circ$
 (microphone 9), (b) $\theta = 96^\circ$ (microphone 12), (c) $\theta = 140^\circ$
 (microphone 8).

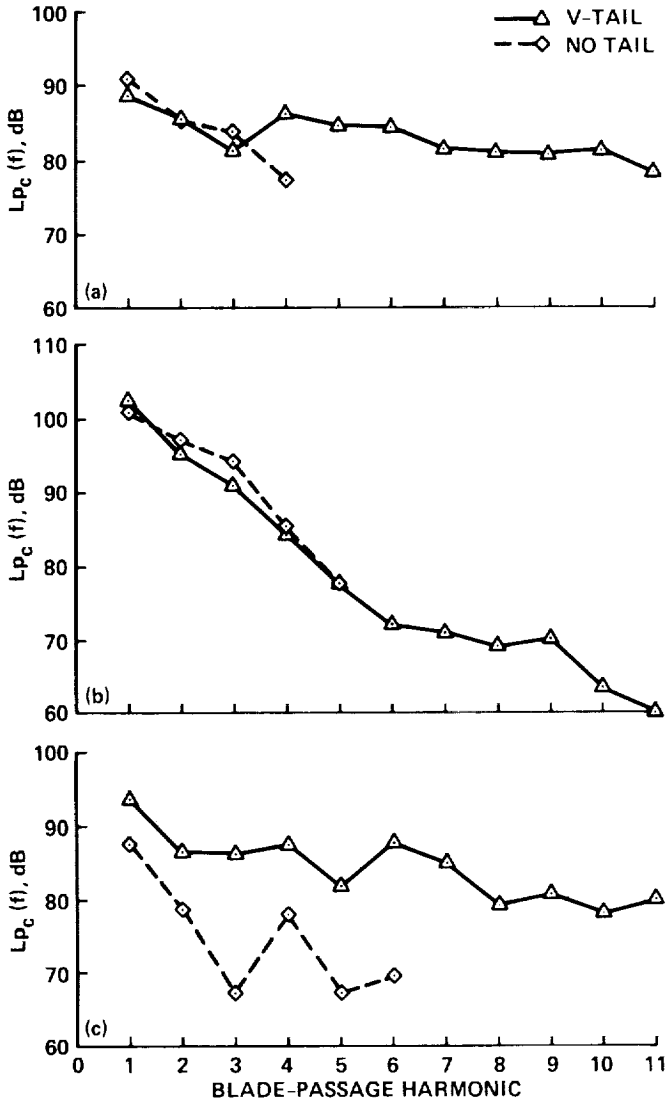


Figure 21. Effect of V-tail on harmonics of blade-passage noise. $U_\infty = 62$ m/sec, $N = 8200$ rpm, $x'/c' = 0.83$.
 (a) $\theta = 15^\circ$ (microphone 9), (b) $\theta = 96^\circ$ (microphone 12),
 (c) $\theta = 140^\circ$ (microphone 8).

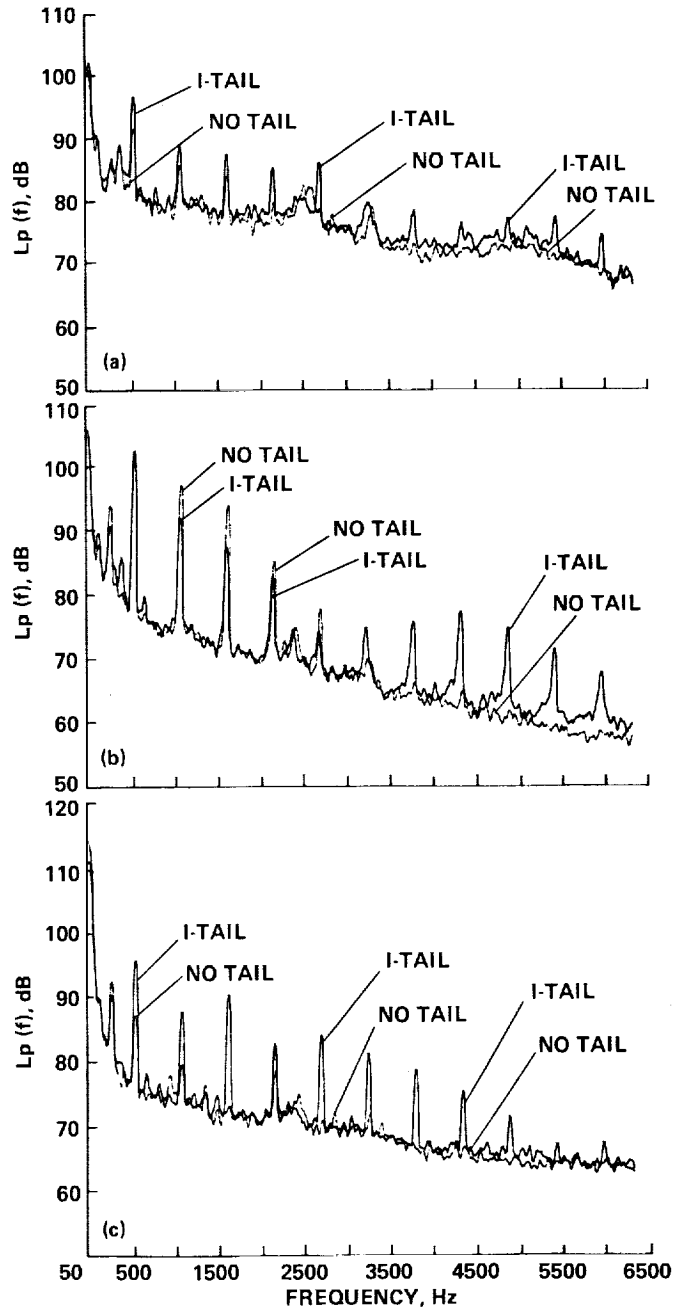


Figure 22. Effect of I-tail on acoustic spectrum. $U_\infty = 62$ m/sec, $N = 8200$ rpm, $x'/c' = 0.31$. (a) $\theta = 15^\circ$ (microphone 9), (b) $\theta = 96^\circ$ (microphone 12), (c) $\theta = 140^\circ$ (microphone 8).

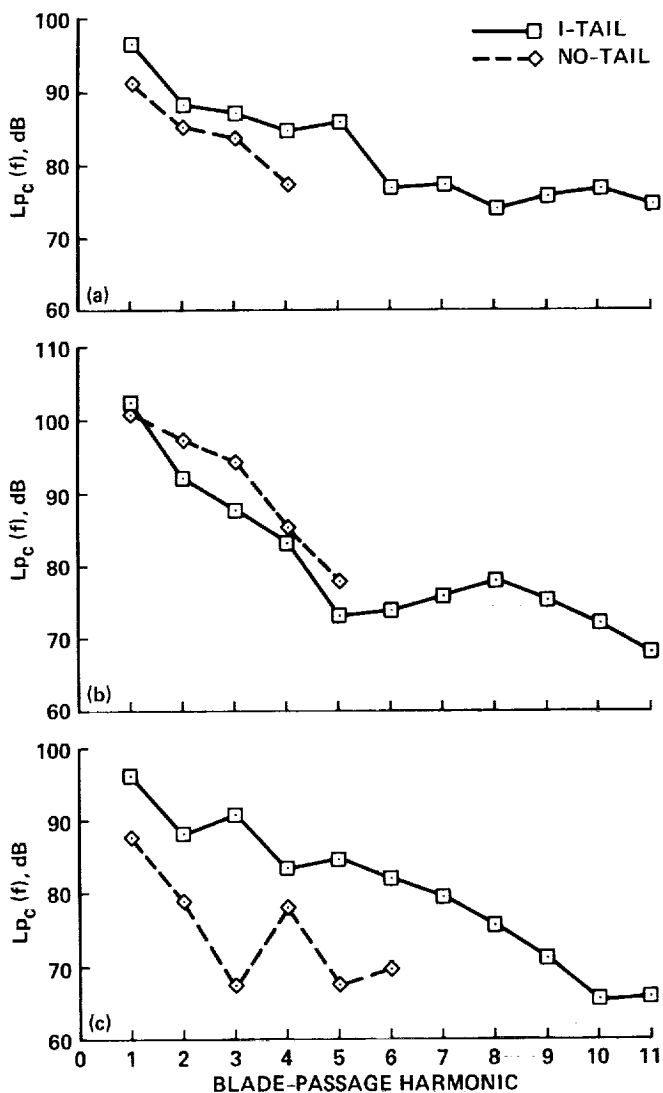


Figure 23. Effect of I-tail on harmonics of blade-passage noise. $U_\infty = 62$ m/sec, $N = 8200$ rpm, $x'/c' = 0.31$. (a) $\theta = 15^\circ$ (microphone 9), (b) $\theta = 96^\circ$ (microphone 12), (c) $\theta = 140^\circ$ (microphone 8).

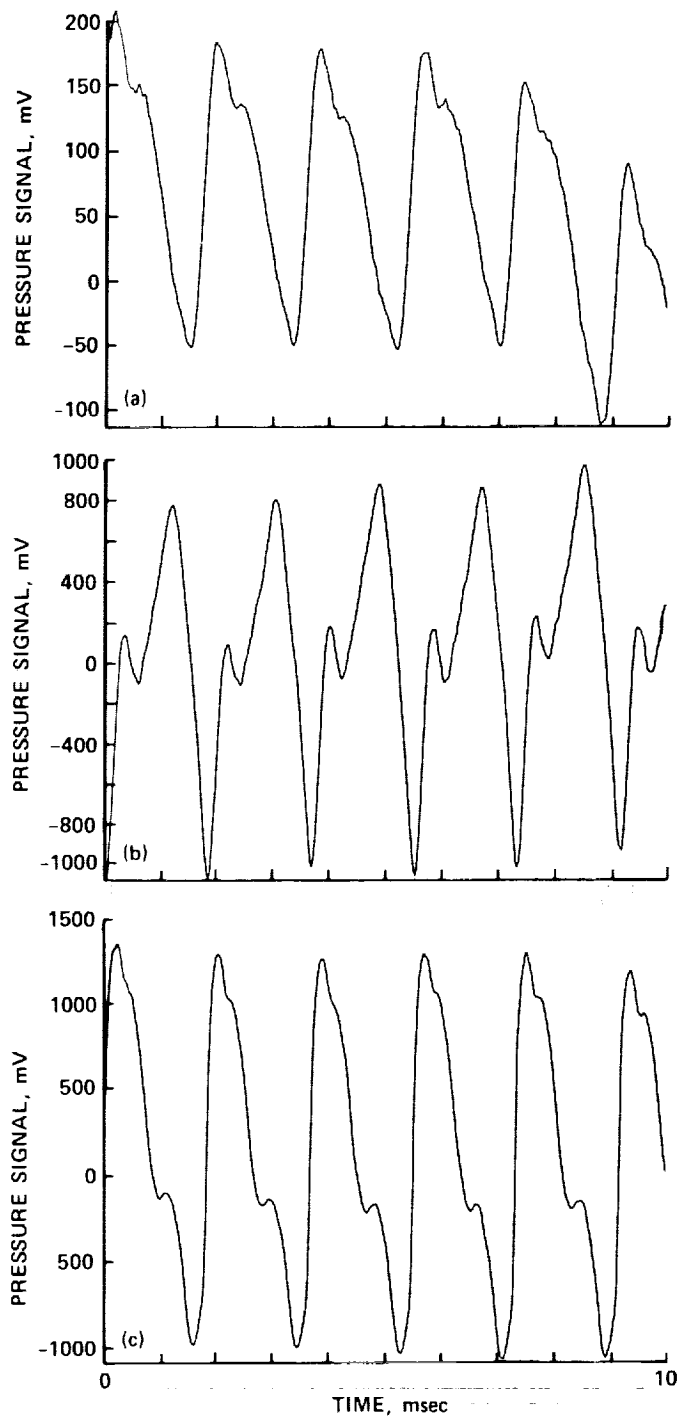


Figure 24. A comparison of time traces measured inside (microphone 7) and outside the shear layer (microphones 5 and 12). Sixty samples were captured at the blade-passage rate and then averaged. $U_\infty = 62$ m/sec, $N = 8200$ rpm (I-tail installed, $x' = 89$ mm). (a) $\theta = 105^\circ$ (microphone 7—in flow), (b) $\theta = 111^\circ$ (microphone 5—out of flow), (c) $\theta = 96^\circ$ (microphone 12—out of flow).

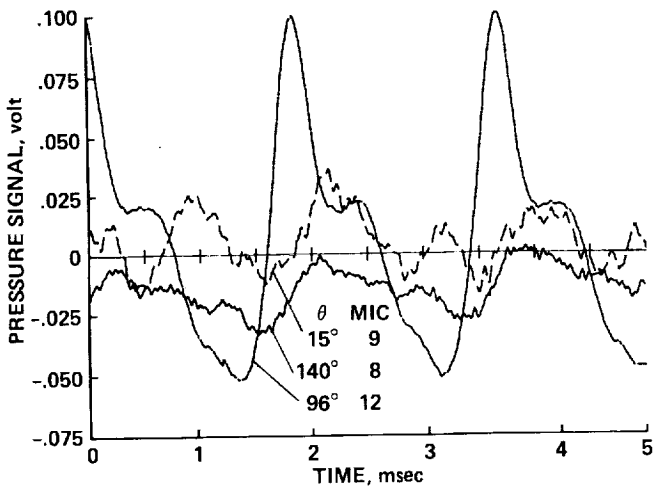


Figure 25. Acoustic pressure in the time domain; propeller operating without empennage installed. $\theta = 15, 96,$ and 140° , $U_\infty = 62$ m/sec, $N = 8200$ rpm.

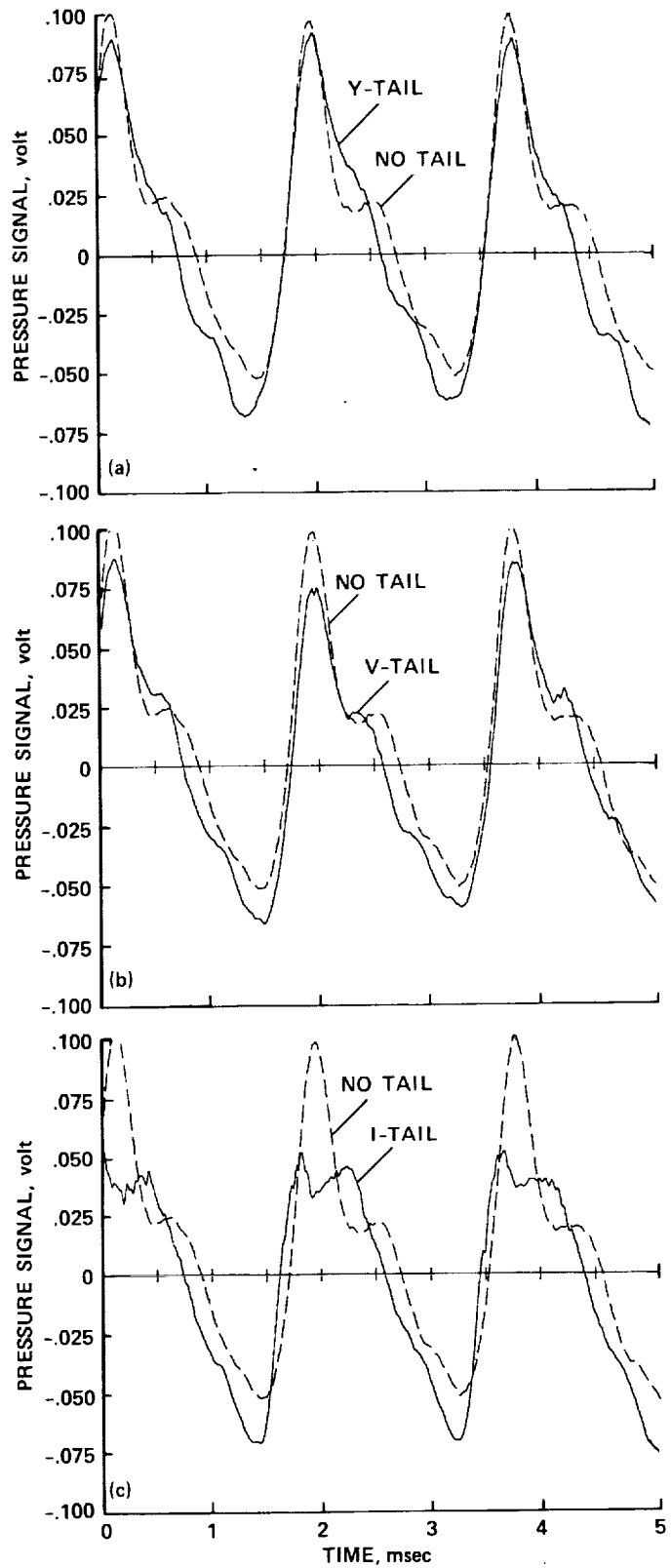


Figure 26. Effect of empennage on acoustic pressure in propeller plane in time domain. $\theta = 96^\circ$ (microphone 12), $U_\infty = 62$ m/sec, $N = 8200$ rpm. (a) With and without Y-tail ($x'/c' = 0.80$), (b) with and without V-tail ($x'/c' = 0.83$), (c) with and without I-tail ($x'/c' = 0.44$).

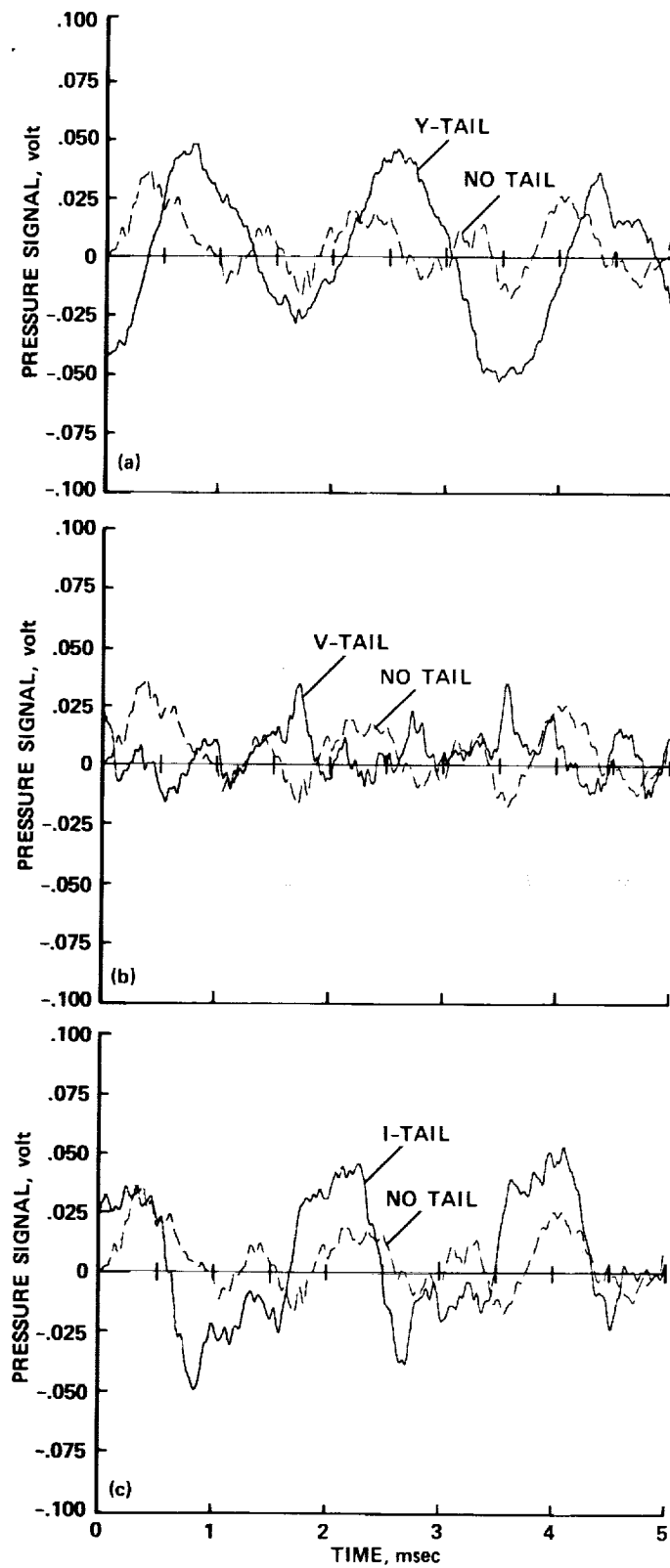


Figure 27. Effect of empennage on upstream acoustic pressure in time domain. $\theta = 15^\circ$ (microphone 9), $U_\infty = 62$ m/sec, $N = 8200$ rpm. (a) With and without Y-tail ($x'/c' = 0.80$), (b) with and without V-tail ($x'/c' = 0.83$), (c) with and without I-tail ($x'/c' = 0.44$).

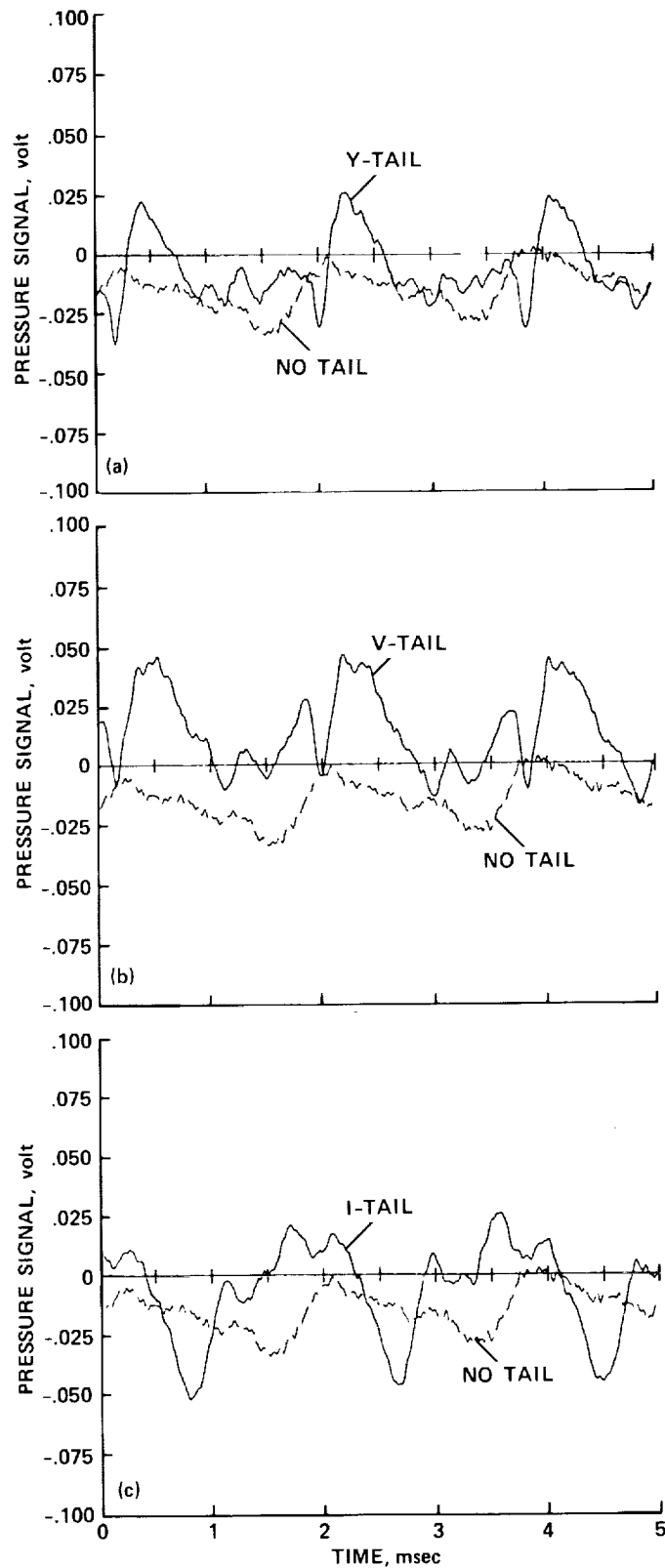


Figure 28. Effect of empennages on downstream acoustic pressure in time domain $\theta = 140^\circ$ (microphone 8), $U_\infty = 62$ m/sec, $N = 8200$ rpm. (a) With and without Y-tail ($x'/c' = 0.80$), (b) with and without V-tail ($x'/c' = 0.83$), (c) with and without I-tail ($x'/c' = 0.44$).

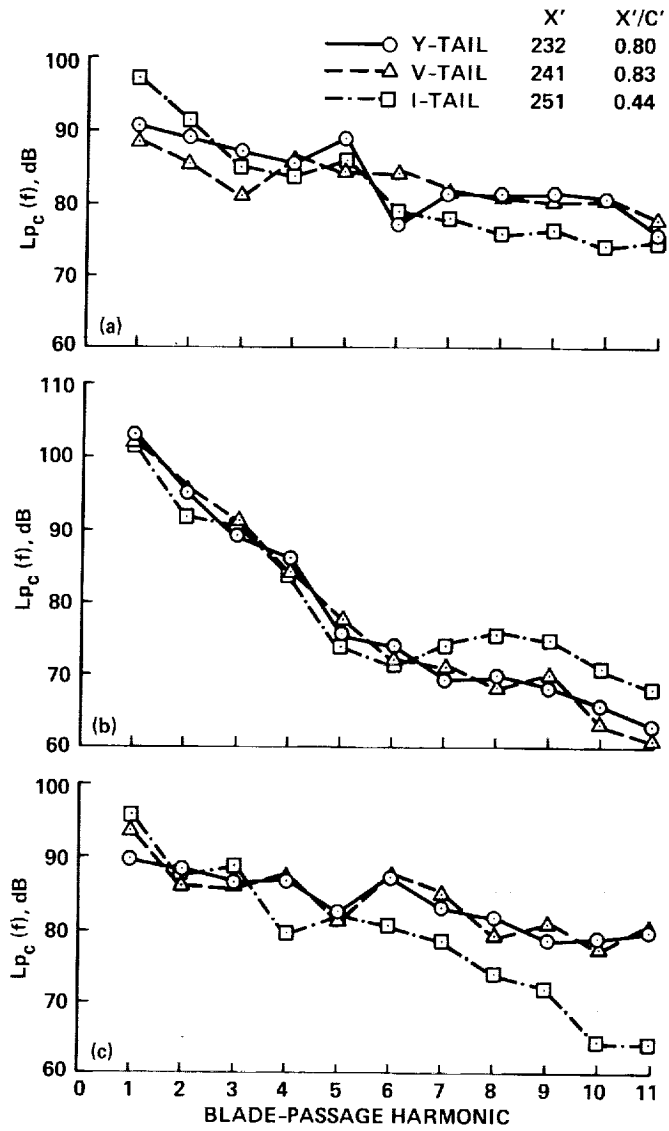


Figure 29. Comparison of harmonic noise levels generated by three empennages interacting with the propeller. $U_{\infty} = 62$ m/sec, $N = 8200$ rpm. (a) $\theta = 15^{\circ}$, approximately 0.24 m spacing between empennage and propeller, (b) $\theta = 96^{\circ}$, approximately 0.24 m spacing between empennage and propeller, (c) $\theta = 140^{\circ}$, approximately 0.24 m spacing between empennage and propeller.

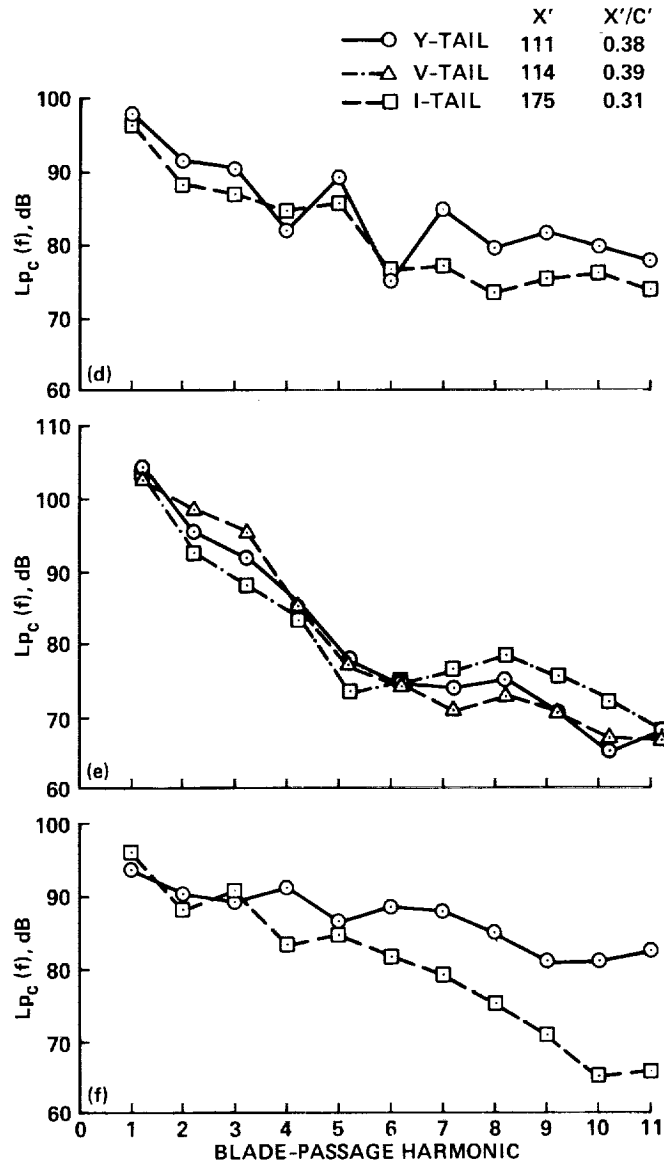


Figure 29. Concluded. (d) $\theta = 15^\circ$, 0.11-0.18 m spacing between empennage and propeller, (e) $\theta = 96^\circ$, 0.11-0.18 m spacing between empennage and propeller, (f) $\theta = 140^\circ$, 0.1-0.18 m spacing between empennage and propeller.

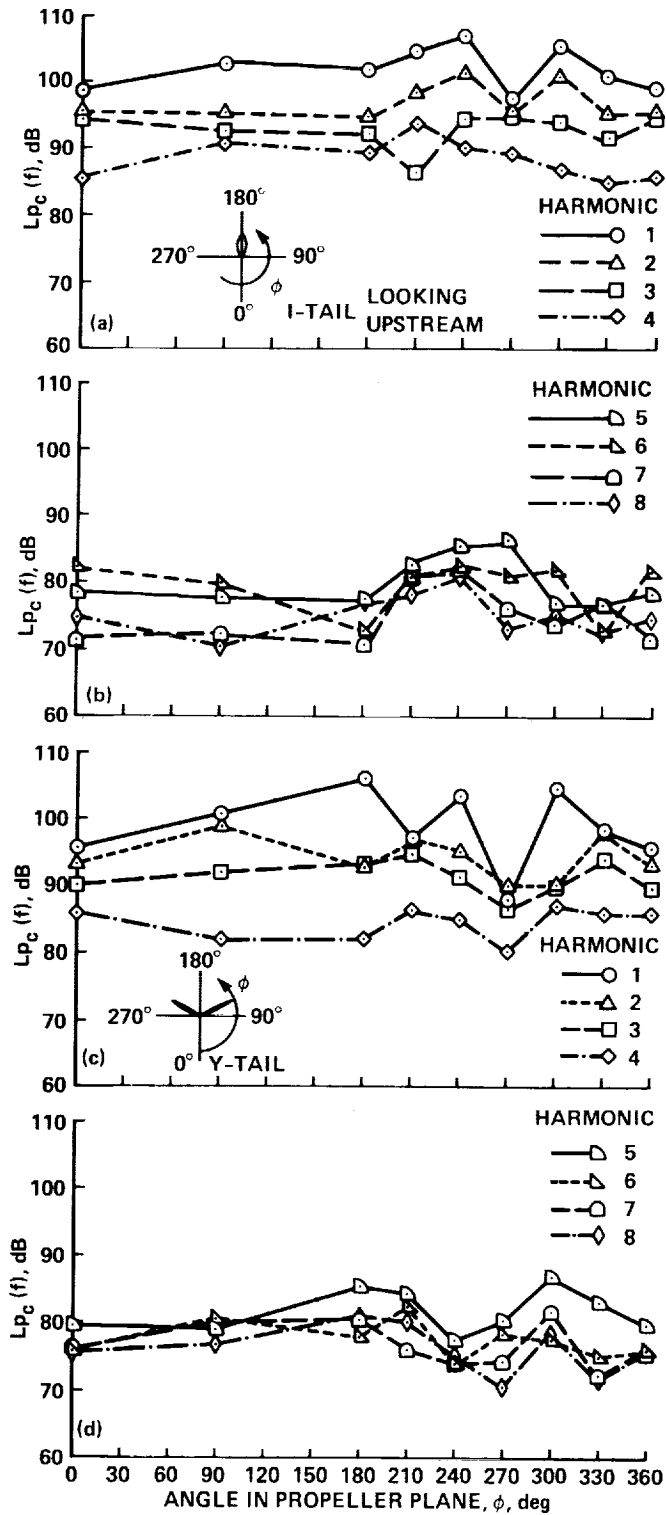


Figure 30. Acoustic directivity in vertical plane containing the propeller $U_\infty = 62$ m/sec, $N = 8200$ rpm. (a) I-tail, harmonics 1-4 ($x'/c' = 0.16$), (b) I-tail, harmonics 5-8 ($x'/c' = 0.16$), (c) Y-tail, harmonics 1-4 ($x'/c' = 0.38$), (d) Y-tail, harmonics 5-8 ($x'/c' = 0.38$).

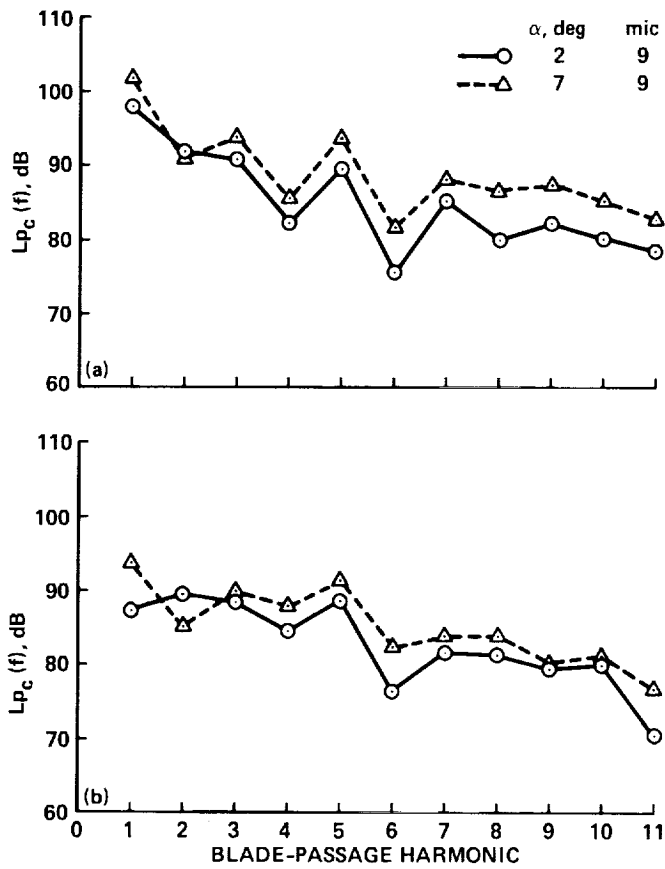


Figure 31. Effect of Y-tail incidence on harmonic noise levels for two propeller/empennage spacings. $\theta = 15^\circ$, $U_\infty = 62$ m/sec, $N = 8200$ rpm. (a) $x' = 111$ mm ($x'/c' = 0.38$), (b) $x' = 308$ mm ($x'/c' = 1.06$).

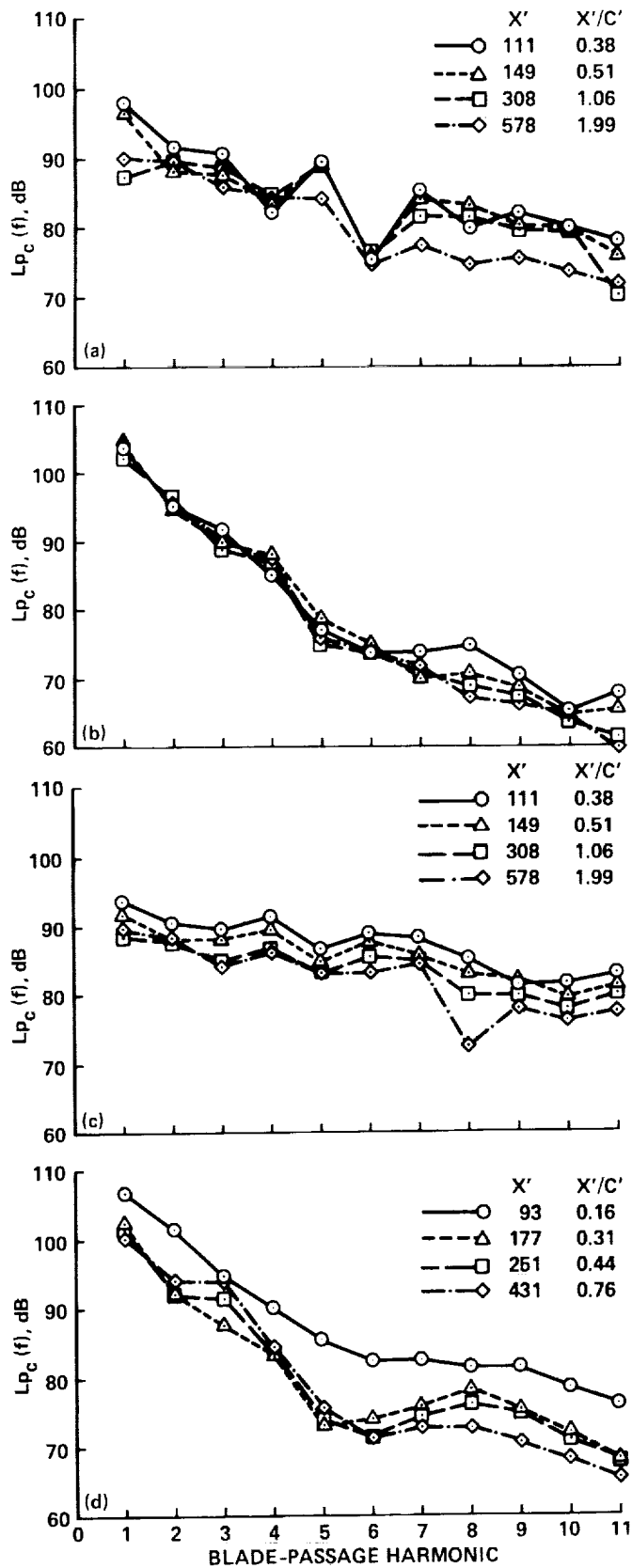


Figure 32. Variation of harmonic noise levels with propeller/empennage spacing. $U_\infty = 62$ m/sec, $N = 8200$ rpm. (a) $\theta = 15^\circ$ (microphone 9) Y-tail, (b) $\theta = 96^\circ$ (microphone 12) Y-tail, (c) $\theta = 140^\circ$ (microphone 8) Y-tail, (d) $\theta = 96^\circ$ (microphone 12) I-tail.

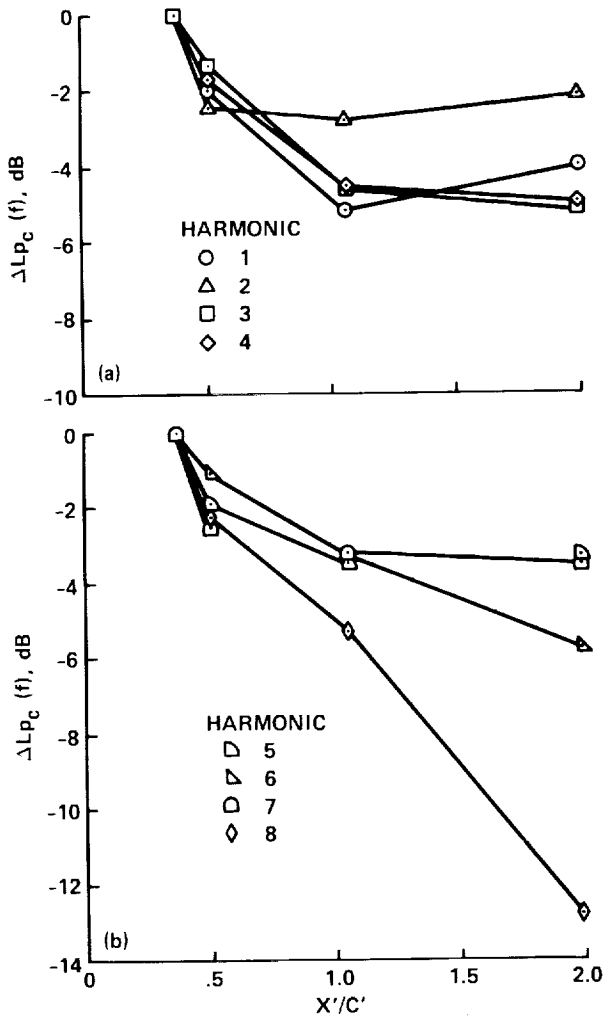


Figure 33. Decay of blade-passage harmonic levels with propeller/empennage normalized spacing (relative to noise at closest spacing). $\theta = 140^\circ$, Y-tail installed, $U_\infty = 62 \text{ m/sec}$, $N = 8200 \text{ rpm}$. (a) Harmonics 1-4, (b) harmonics 5-8.

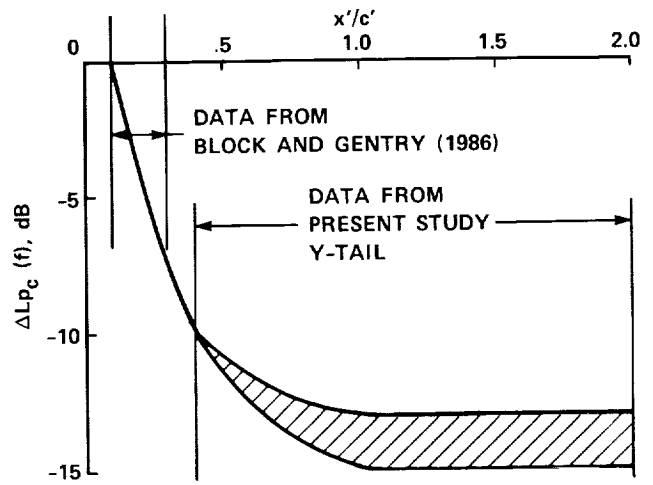


Figure 34. Summary plot of noise decay versus propeller/empennage normalized spacing (relative to closest spacing used by Block and Gentry of $x'/c' = 0.1$). Noise decay is for blade-passage harmonics 1-8. Data from present study are for Y-tail installed. $\theta = 140^\circ$, $U_\infty = 62 \text{ m/sec}$, $N = 8200 \text{ rpm}$.

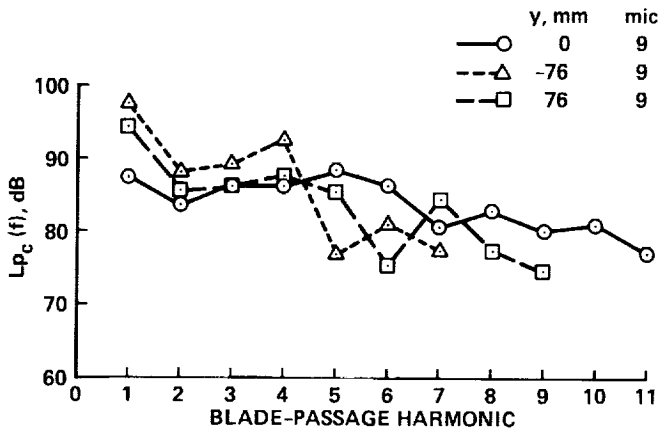


Figure 35. Effect of vertical displacement of propeller relative to fuselage centerline on harmonic noise levels. $\theta = 15^\circ$, Y-tail installed, $U_\infty = 62$ m/sec, $N = 8200$ rpm, $x'/c = 0.83$.

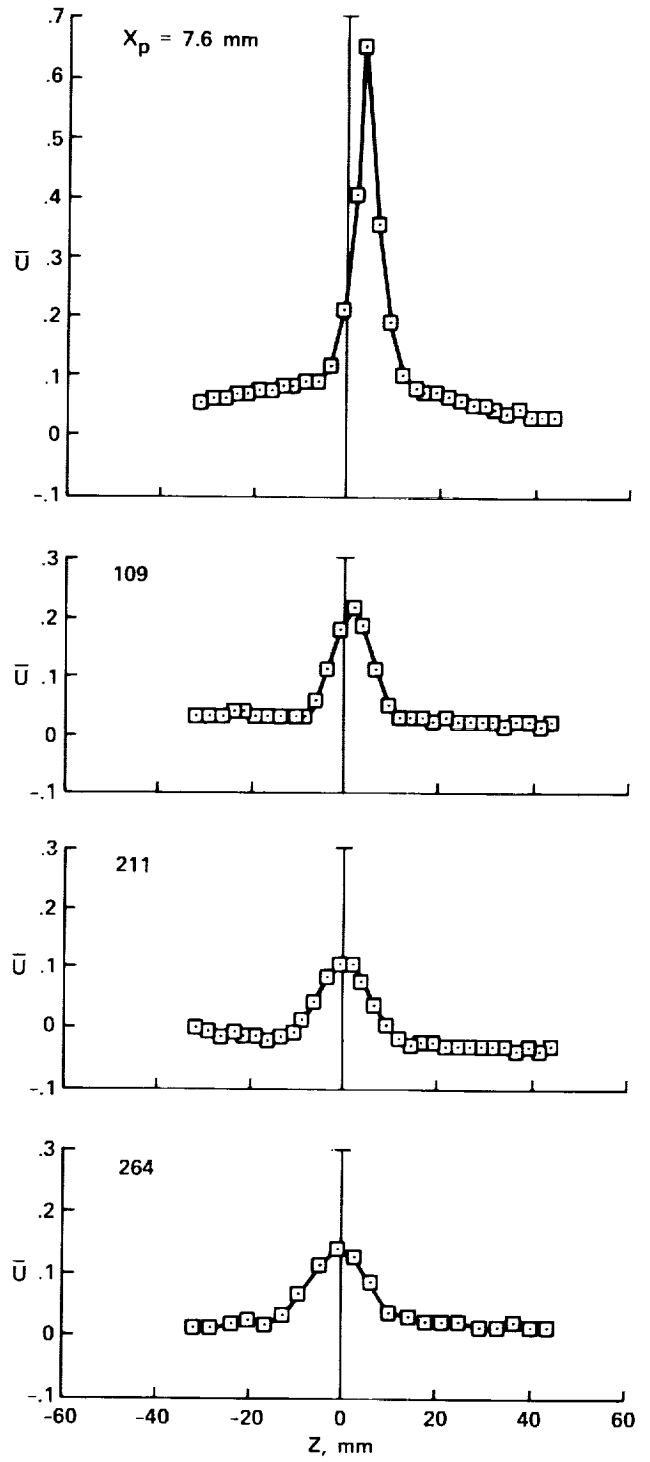


Figure 36. Wake flow field of the I-tail in terms of the mean axial velocity deficit profile at several downstream stations (x_p). $y = 305$ mm, propeller off, $U_\infty = 46$ m/sec.

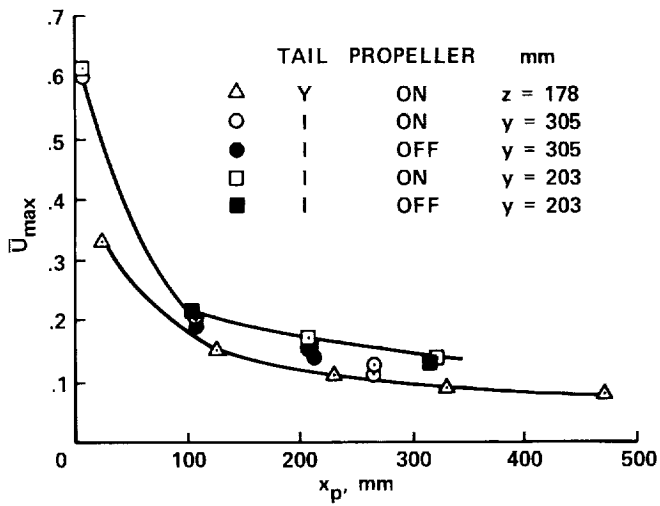


Figure 37. Peak wake deficit versus distance from the empennage as measured upstream from the probe. The wake deficit is in terms of the mean axial velocity profile.

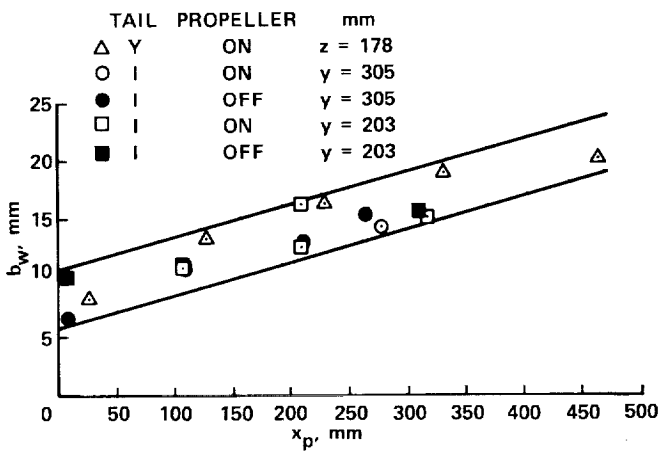


Figure 38. Wake width at mid-height of wake-deficit profile plotted versus distance from the empennage.

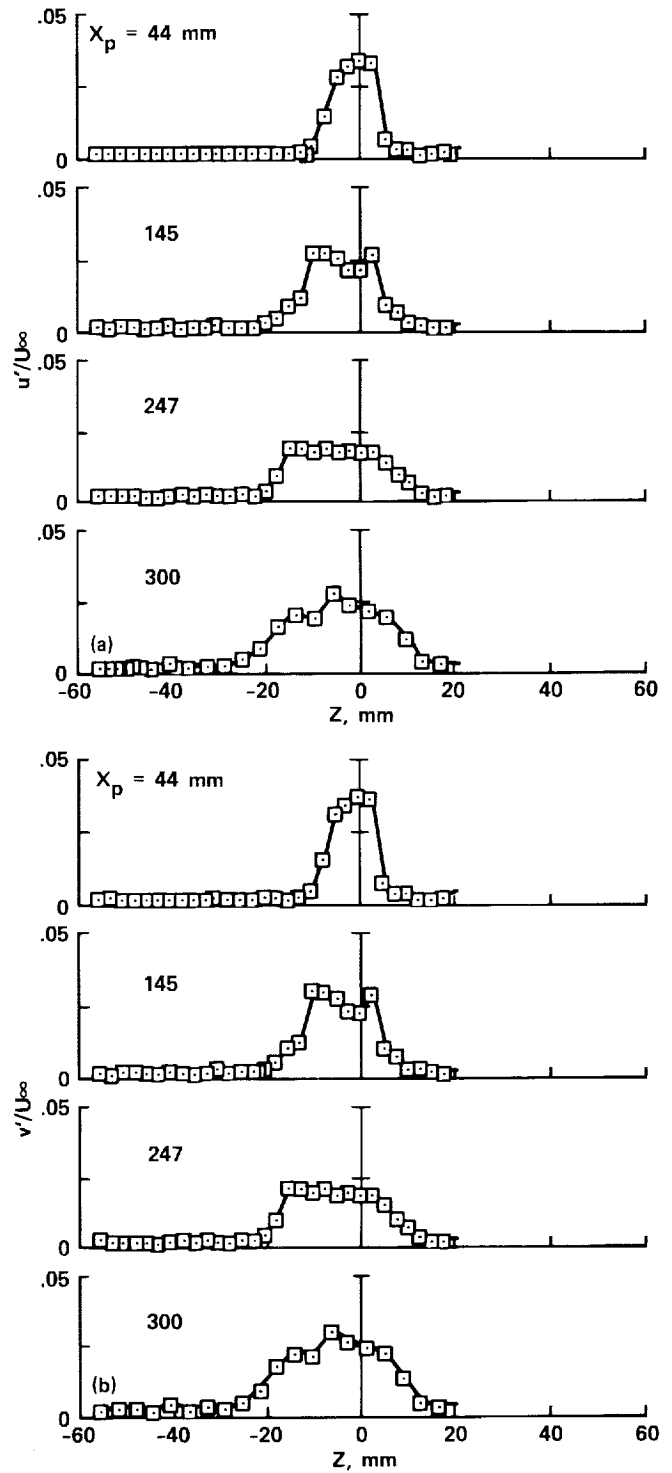


Figure 39. Turbulence distribution measured during cross-stream surveys through the I-tail wake at $y = 305$ mm; propeller off. (a) Axial turbulence, u'/U_∞ , (b) cross-stream turbulence in y -direction, v'/U_∞ .

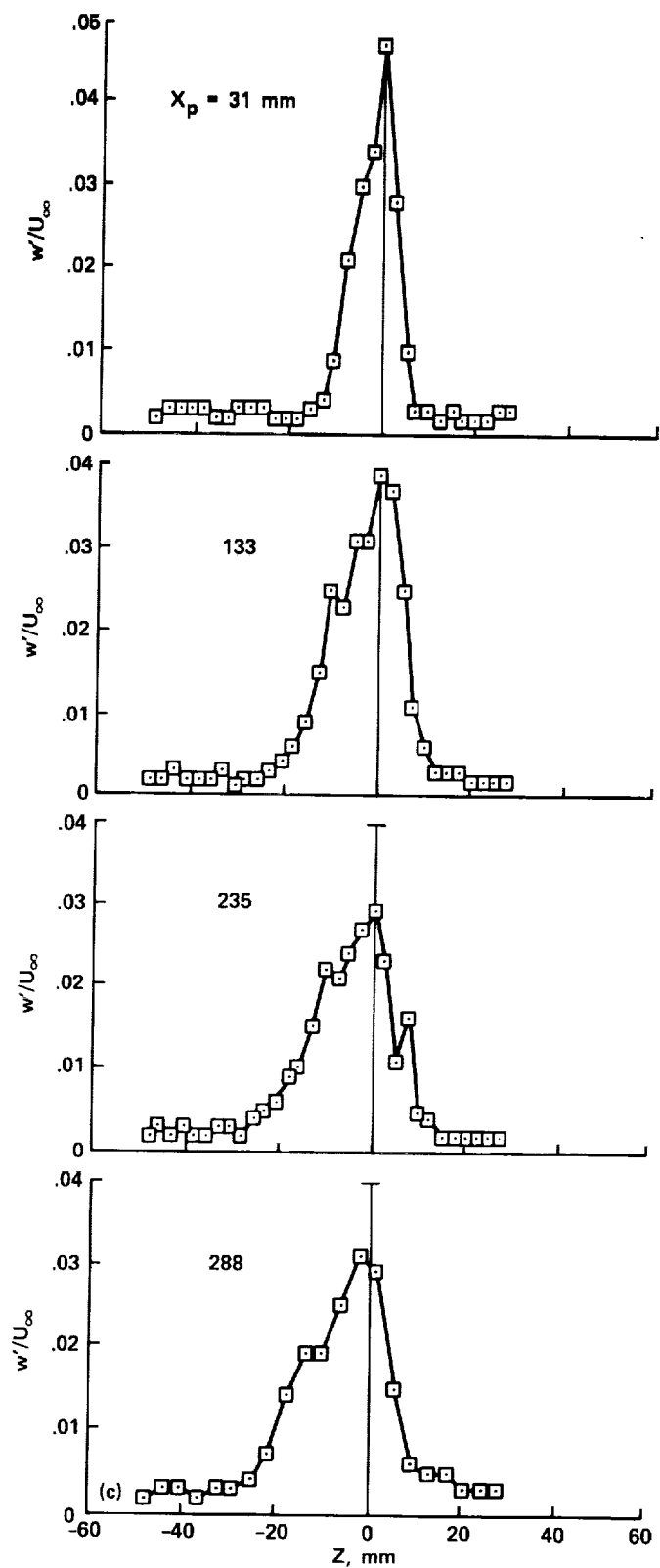


Figure 39. Concluded. (c) Cross-stream turbulence in z-direction, w'/U_∞ .

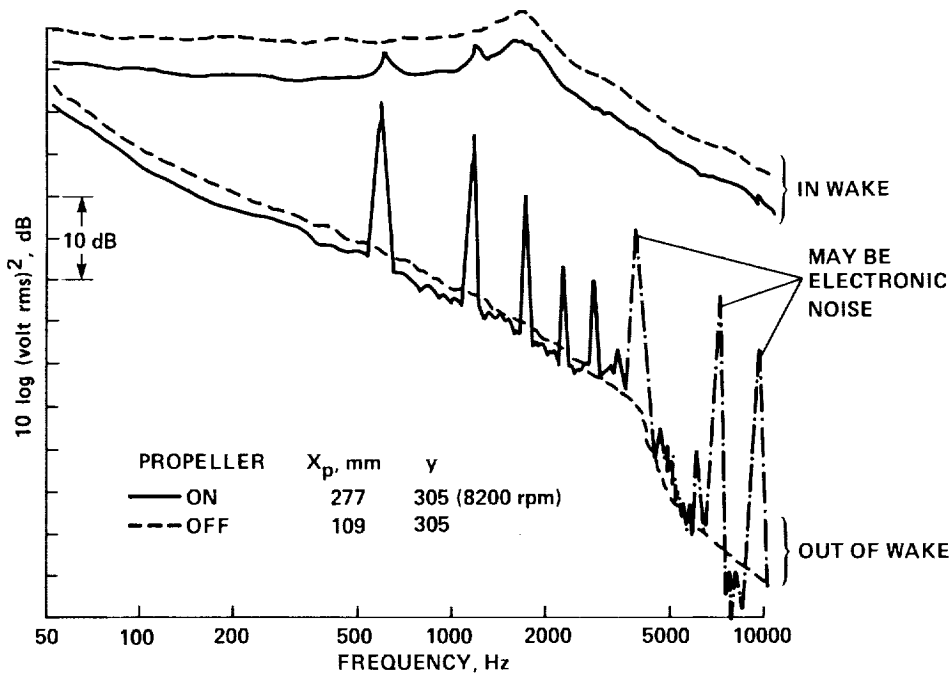


Figure 40. Typical hot-wire spectra measured in and out of the I-tail wake; propeller on and off. $U_\infty = 62$ m/sec. Constant 25-Hz bandwidth filter.

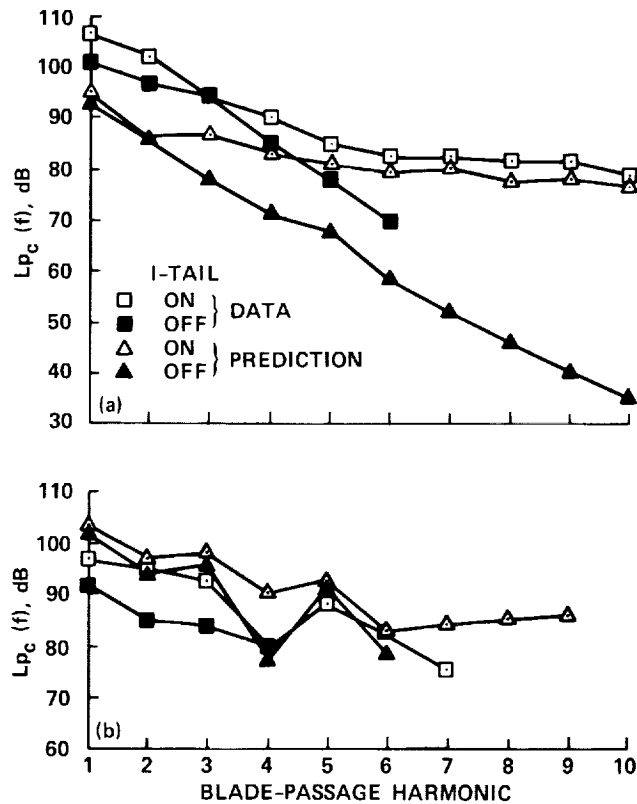


Figure 41. Predicted and measured propeller harmonic noise levels with and without empennage/propeller interaction. (a) In-plane noise, (b) upstream noise.



Report Documentation Page

1. Report No. NASA TP-3040		2. Government Accession No.		3. Recipient's Catalog No.	
4. Title and Subtitle Acoustic and Aerodynamic Study of a Pusher-Propeller Aircraft Model			5. Report Date September 1990		
			6. Performing Organization Code		
7. Author(s) Paul T. Soderman and W. Clifton Horne			8. Performing Organization Report No. A-89038		
			10. Work Unit No. 505-61-11		
9. Performing Organization Name and Address Ames Research Center Moffett Field, CA 94035			11. Contract or Grant No.		
			13. Type of Report and Period Covered Technical Paper		
12. Sponsoring Agency Name and Address National Aeronautics and Space Administration Washington, DC 20546-0001			14. Sponsoring Agency Code		
			15. Supplementary Notes Point of Contact: Paul T. Soderman, Ames Research Center, MS 247-2, Moffett Field, CA 94035-1000 (415) 604-6675 or FTS 464-6675		
16. Abstract An aerodynamic and acoustic study was made of a pusher-propeller aircraft model in the NASA Ames Research Center 7- by 10-Foot Wind Tunnel. The test section was modified to operate as an open jet. The 591-mm diameter unswept propeller was operated alone and in the wake of three empennages—an I-tail, a Y-tail, and a V-tail. The radiated noise and detailed wake properties were measured. Results indicate that the unsteady blade loading caused by the blade interactions with the wake mean velocity distribution had a strong effect on the harmonics of blade-passage noise. In particular, the blade-passage harmonics above the first were substantially increased in all horizontal directions by the empennage/ propeller interaction. Directivity in the plane of the propeller was maximum perpendicular to the blade surface. Increasing the tail loading caused the propeller harmonics to increase 3-5 dB for an empennage/propeller spacing of 0.38 mean empennage chords. The interaction noise became weak as empennage/propeller spacing was increased beyond 1.0 mean empennage chord lengths. Unlike the mean wake deficit, the wake turbulence had only a small effect on the propeller noise, that effect being a small increase in the broadband noise. A propeller noise theory, which incorporated an unsteady blade-loading model, indicates that the interaction noise trends can be predicted if the unsteady blade-loading aerodynamic and acoustics are modeled properly.					
17. Key Words (Suggested by Author(s)) Propeller noise Pusher propeller Empennage wake Propeller-empennage interaction			18. Distribution Statement Unclassified-Unlimited Subject Category 71		
19. Security Classif. (of this report) Unclassified		20. Security Classif. (of this page) Unclassified		21. No. of Pages 68	22. Price A04